

Self-assembly and foam stability of a cationic and anionic surfactant mixture

José Luís Sousa Ferreira

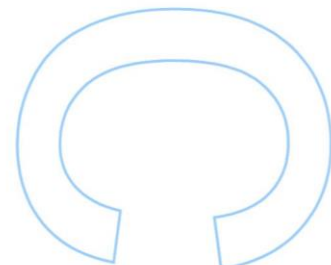
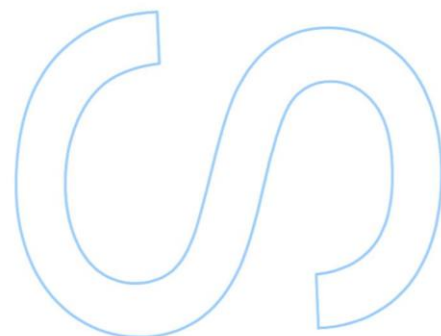
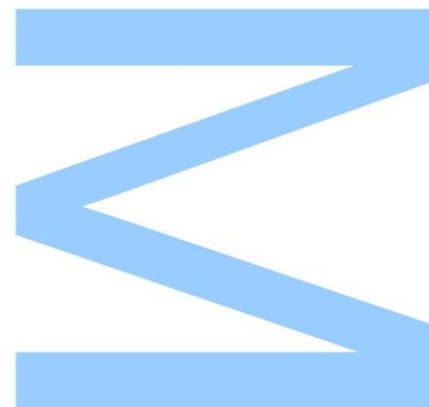
Mestrado em Química
Departamento de Química
2016

Orientador

Prof. Doutor Eduardo F. Marques, Faculdade de Ciências da Universidade do Porto

Coorientador

Prof^a. Doutora Anniina Salonen, Université Paris-Sud

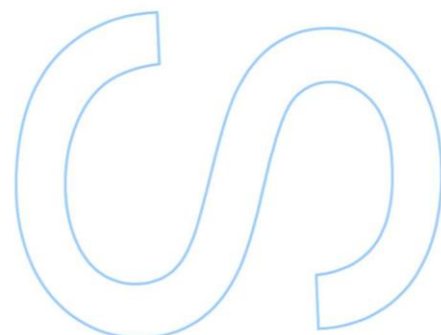
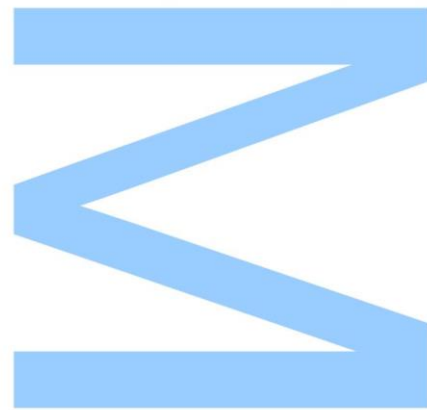




Todas as correções determinadas pelo júri, e só essas, foram efetuadas.

O Presidente do Júri,

Porto, ____ / ____ / ____



Acknowledgments

This project was only possible due to the contribution of many people that in one way or the other helped in the construction of this piece of knowledge. Therefore I want to address my gratitude to:

My supervisor Professor Eduardo Marques for giving me the opportunity to work in his group, for the concern and availability to guide me through this project. Thank you for your time and patience along this year.

My co supervisor Professor Anniina Salonen for the patience support and knowledge showed through the time we spent together.

All my colleagues in the physical chemistry group in Portugal, Isabel Oliveira, Barbara Abreu, Ricardo Bessa, Carlos Lima, Filipe Ribeiro, Ana Rodrigues e Inês Vaz for the great company and environment.

All my colleagues in the soft interfaces group in France, Alesya Mikhailovskaia, Manish Kushal, Maxime Shneider and Emillie Forel for all the help and partnership during this project.

Laury Lopes for supporting me every time and expand my horizons.

All my friends and family for all positive influence they had on me through this experience, with a special regard for my parents. Without them nothing of this would be possible from the beginning.

Abstract

Surfactants are amphiphilic molecules that find applications in the most diverse environments, from housekeeping products to industrial processes. The study of surfactant mixtures has drawn the attention of academy and industry due to the general enhanced adsorption properties the mixtures present, as compared to the individual surfactants. These effects are especially enhanced in mixtures of cationic and anionic surfactants due to the electrostatic interaction between opposite charges that leads to significant synergism between the surfactants (negative deviation from ideal behavior).

This project aims develop the understanding of the phase behavior of the catanionic mixture cetyl trimethylammonium bromide/ sodium octyl sulfonate, as a function of the CTAB molar fraction, and to investigate how different compositions affect the ageing process of foams generated from the different solutions. The effect of the ratio between the two oppositely charged surfactants was studied resorting to several experimental methods. The interfacial properties of the mixtures were studied by tensiometry, while the bulk aggregation behavior was characterized by light microscopy, dynamic light scattering, cryogenic transmission electron microscopy and small angle neutron scattering. The viscosity of the different samples was probed by solution rheometry. Foam ageing was characterized by photography and small angle neutron scattering.

Results showed significant differences in aggregation behavior and foam ageing for the different CTAB molar fractions studied. The presence of ellipsoid and rod-like micelles was found in this system, along with the formation of spontaneous vesicles for both equimolar composition and excess of SOSo. The data obtained also suggest that foam aging is related to the aggregates present in bulk solutions, and with the nature of the dispersed gas.

The results were further rationalized on the basis of the model of the critical packing parameter of surfactants, the molecular interactions at play and the interactions between self-assembled structures and foam structure.

Key words: surfactants, foam, self-assembly, ageing, vesicles, rods

Resumo

Os surfactantes ou tensoactivos consistem em moléculas anfifílicas cuja aplicação é encontrada nos mais diversos meios, desde produtos domésticos a processos industriais. O estudo de misturas de surfactantes reveste-se de grande interesse, quer a nível científico, que a nível industrial devido ao melhoramento das propriedades interfaciais de mistura, em comparação com os surfactantes individuais. Estes efeitos são especialmente significativos em misturas entre surfactantes catiónicos e aniónicos devido à interação eletrostática entre cargas opostas, que conduz a um elevado grau de sinergismo (desvio negativo ao comportamento ideal).

Este projeto teve como objectivo o estudo do comportamento de fase da mistura catiónica brometo de cetil trimetilamónio (CTAB) / octil sulfonato de sódio (SOSo), em função da fração molar de CTAB, e da influencia da diferente composição da mistura no processo de envelhecimento de espuma gerada pelas diferentes soluções. O efeito provocado pelas diferentes razões de mistura entre os surfactantes de carga oposta no comportamento de auto-agregação foi estudado recorrendo a várias técnicas experimentais. As propriedades interfaciais das misturas foram estudadas por tensiometria, enquanto a agregação no seio da solução foi investigada por microscopia de luz, dispersão dinâmica de luz, microscopia de transmissão electrónica criogénica, e difração de neutrões de baixo ângulo. A viscosidade das diferentes amostras foi determinada por reometria de soluções. Os processos de envelhecimento das espumas foram caracterizados por fotografia e difração de neutrões de baixo ângulo.

Os resultados revelam diferenças significativas na agregação e no processo de envelhecimento da espuma para diferentes frações molares de CTAB estudadas. A presença de estruturas micelares elipsoidais e em forma de cilindro rígido foram encontradas para este sistema, assim como a formação espontânea de vesículas estáveis tanto para composição equimolar como para excesso em SOSo. Os dados obtidos sugerem também que o envelhecimento destas espumas está diretamente relacionado com o tipo de agregados em solução e com a natureza do gás disperso.

Os resultados foram racionalizados pelo modelo do parametro crítico de empacotamento de surfactantes, pelas interações moleculares em jogo e pela interação entre a estrutura dos agregados e estrutura da espuma.

Palavras chave: surfactantes, espuma, auto-agregação, vesículas, micelas.

Table of Contents

Acknowledgments.....	1
Abstract	2
Resumo	3
List of figures	6
List of tables	10
Acronims and symbols.....	11
1 Introduction.....	13
1.1 Introduction to self-assembled systems and foams as colloidal systems	13
1.2 Surfactant solutions.....	13
1.2.1 Surfactants.....	13
1.2.2 Surface tension.....	17
1.2.2 Surfactant self-assembly.....	19
1.2.3 Catanionic mixtures	24
1.3 Foams	27
1.3.1 Daily life examples and industrial applications of foams	27
1.3.3 Formation.....	29
1.3.4 Structure	30
1.3.5 Foam ageing.....	32
1.4 Aim of this project.....	35
2 Experimental section.....	36
2.1 Materials.....	36
2.2 Sample preparation	36
2.3 Foam generation	37
2.4 Experimental methods.....	38
2.4.1 Tensiometry	38
2.4.2 Light microscopy	40
2.4.3 Dynamic Light Scattering (DLS)	42
2.4.4 Zeta potential	43
2.4.5 Solution rheometry.....	45
2.4.6 Cryogenic Transmission Electron Microscopy (cryo-TEM)	46
2.4.7 Small Angle Neutron Scattering SANS.....	47
2.4.8 Foam Characterization by Photography	49
3 Results.....	52
3.1 Bulk behavior	53

3.1.1 CTAB/SO ₂ mixture – macroscopic characterization	53
3.1.2 Aggregate shape and size	54
3.1.3 Aggregate distribution and zeta potential	55
3.1.4 <i>C_{mc}</i> determination by surface tension	59
3.1.5 Viscosity profile by solution rheometry	62
3.1.6 Cryo-TEM observations	63
3.1.7 Small Angle Neutron Scattering (SANS) study	64
3.1.8 Discussion – Bulk behavior	69
3.2 Foams	75
3.2.1 Foam ageing	75
3.2.4 SANS in foams	80
3.2.5 Discussion – Foam behavior	83
4 Conclusions and perspectives	86
5 Bibliography:	88

List of figures

Figure 1 - A) Surfactant representation, B) Surfactant behavior in a solution	14
Figure 2 - Example of an anionic surfactant: sodium dodecyl sulfate (SDS).....	15
Figure 3 - Example of cationic surfactant: cetyl trimethylammonium bromide (CTAB). 15	
Figure 4 - Example of a nonionic surfactant: Octaethylene glycol monododecyl ether (C ₁₂ E ₈)	16
Figure 5 - Example of a zwitterionic surfactant: Palmitoyl-oleyl-sn-phosphatidylcholine	16
Figure 6 - Example of a catanionic surfactant: tetradecyltrimethylammonium dodecylsulphate.....	17
Figure 7 - Representation of conventional (left) and gemini surfactants (right).....	17
Figure 8 - Illustration of the notorious variation for different physicochemical properties of surfactants solutions before and after cmc. Adapted from ^[9]	19
Figure 9 – Schematic representation of the Krafft point for a certain surfactant [8].....	20
Figure 10 - Fontell scheme for the dependence of surfactant liquid crystalline structure on composition, illustrating the symmetry of curvature location of cubic phases. Adapted from [1]	24
Figure 11 - Structure of a typical dry foam	27
Figure 12 - Examples of foams. A) Mineral flotation; B) Beer foam; C) Sea foam; D) Firefighting foam. Adapted from ^[22]	28
Figure 13 – Profile of a draining foam	31
Figure 14 - Representation of: A) CTAB molecule; B) SOSo molecule	36
Figure 15 - Schematic representation of the double syringe method.....	37
Figure 16 - Representation of the Wilhelmy plate method for surface tension measurements.....	38
Figure 17 - Graphic representation of the surface tension variation with the natural logarithm of the concentration.....	39
Figure 18 - Schematic representation of a microscope equipped with differential interference contrast system. Adapted from ^[41]	41
Figure 19 - Schematic illustration of a basic light scattering apparatus	42
Figure 20 - Schematic representation of surface charge distribution around a positive charged particle	44
Figure 21 – Schematic representation of three main geometries of rotational viscometers: A) Cup and bob; B) Cone; C) Disc. Adapted from ^[50]	45
Figure 22 - Schematic representation of sample preparation for Cryo-TEM observation. Adapted from ^[54]	46

Figure 23 - Form factors for different particle shapes with the same radius of gyration. Adapted from ^[56]	48
Figure 24 - Schematic representation of the setup used to measure drainage velocity	50
Figure 25 - Procedure to evaluate drainage velocity through photographic documentation	51
Figure 26 - Scheme of the approach used to characterize bulk and foam behavior of the cationic mixture CTAB/SOSo.	52
Figure 27 – Visual appearance of CTAB/SOSo mixtures as a function of x_{CTAB}	53
Figure 28 - Schematic representation of CTAB/SOSo phase behavior for the different x_{CTAB}	53
Figure 29 - Microscopic characterization of: A) $0.500 x_{CTAB}$ - 400x magnification, B) $0.500 x_{CTAB}$ - 1000x magnification; C) $0.200 x_{CTAB}$ - 400x magnification, D) $0.200 x_{CTAB}$ - 1000x magnification, E) $0.100 x_{CTAB}$ - 400x magnification, and F) $0.100 x_{CTAB}$ - 1000x magnification.	54
Figure 30 - Size distribution by intensity for $0.900 x_{CTAB}$ at $20 \text{ mmol}\cdot\text{kg}^{-1}$	55
Figure 31 - Size distribution by intensity for 0.800 and $0.750 x_{CTAB}$ at $20 \text{ mmol}\cdot\text{kg}^{-1}$	56
Figure 32 - Size distribution by intensity for $0.667 x_{CTAB}$ at $20 \text{ mmol}\cdot\text{kg}^{-1}$	56
Figure 33 - Size distribution by intensity for 0.500 , 0.200 and $0.100 x_{CTAB}$ at $20 \text{ mmol}\cdot\text{kg}^{-1}$	57
Figure 34 - Zeta potential distribution by intensity for 0.100 , 0.200 , 0.250 , $0.333 x_{CTAB}$ at $20 \text{ mmol}\cdot\text{kg}^{-1}$	58
Figure 35 – Zeta potential distribution by intensity for $0.500 x_{CTAB}$ at $20 \text{ mmol}\cdot\text{kg}^{-1}$	59
Figure 36 - Summary graph of surface tension as a function of the natural logarithm of concentration for different x_{CTAB}	59
Figure 37 – Summary graph of cmc and γ_{cmc} as a function of x_{CTAB}	60
Figure 38 - Measured and calculated cmc for different x_{CTAB}	61
Figure 39 – Viscosity as a function of shear rate for different x_{CTAB}	62
Figure 40 - Cryo-TEM images of sample $0.530 x_{CTAB}$ at $20 \text{ mmol}\cdot\text{kg}^{-1}$ showing vesicles and elongated micelles.	63
Figure 41 – Model example (sample 0.100) of the scattering intensity as a function of the wave vector for vesicles in solution on the left and schematic representation of a vesicle and respective characteristic sizes on the right.	65
Figure 42 - Model example (sample 0.590) of the scattering intensity as a function of the wave vector for rods in solution on the left and schematic representation of a rod and respective characteristic sizes on the right.	65

Figure 43 - Model example (sample 0.800) of the scattering intensity as a function of the wave vector for ellipsoids in solution on the left and schematic representation of a ellipsoid and respective characteristic sizes on the right.	65
Figure 44 - Intensity as a function of q for the different samples analyzed	66
Figure 45 - Comparison of the fitting of 0.800 x_{CTAB} data for A) ellipsoid form factor, and B) sphere form factor	68
Figure 46 - Scaling factor as a function of the x_{CTAB}	69
Figure 47 - Schematic representation of the types of aggregates formed as a function of x_{CTAB}	71
Figure 48 - Drainage velocity of foams, at 20% liquid fraction generated with simple air, as a function of the x_{CTAB}	75
Figure 49 - Drainage velocity of different x_{CTAB} at 20% liquid fraction generated with air containing traces of C_6F_{14}	76
Figure 50 - Product between drainage velocity and viscosity as a function of x_{CTAB} for 20% liquid fraction foams generated with simple air.....	77
Figure 51 - Product between drainage velocity and viscosity as a function of x_{CTAB} for 20% liquid fraction foams generated with air containing trace amounts of C_6F_{14}	77
Figure 52 - Photography of foam at 20% liquid fraction (simple air) from sample 0.600 x_{CTAB} in 20 minutes intervals, representing foam ageing.....	78
Figure 53 - Photography of foam at 20% liquid fraction (air with trace amounts of C_6F_{14}) from sample 0.600 x_{CTAB} , one hour and 1 week after foam generation, representing foam ageing.....	78
Figure 54 - Bubble radius as a function of the x_{CTAB} at 20 % liquid fraction with air containing trace amounts of C_6F_{14} at the time of formation (black) and one week later (red). The y axis is represented in logarithmic scale for convenience.....	79
Figure 55 - Scattering intensity as a function of the wave vector for 0.500 x_{CTAB} solutions at 20 mmol·kg ⁻¹ in D ₂ O, at 10, 15, 20 and 25% liquid fractions with air containing traces of C_6F_{14} as dispersed phase. The blue line represents the q^{-4} decay for low q in sample 0.500 25%.	80
Figure 56 - Scattering intensity as a function of the wave vector for 0.600 x_{CTAB} solutions at 20 mmol·kg ⁻¹ in D ₂ O, at 10, 15, 20 and 25% liquid fractions with air containing traces of C_6F_{14} as dispersed phase.....	81
Figure 57 - Scattering intensity as a function of the wave vector for 0.500 x_{CTAB} solutions at 20 mmol·kg ⁻¹ in D ₂ O, at 15 and 20% liquid fractions with air containing traces of C_6F_{14} as dispersed phase.....	81

Figure 58 - Scattering intensity as a function of the wave vector for 0.500, 0.600 and 0.800 x_{CTAB} solutions at 20 mmol·kg⁻¹ in D₂O, at 15% liquid fraction with air containing traces of C₆F₁₄ as dispersed phase..... 82

Figure 59 - Scattering intensity as a function of the wave vector for 0.500, 0.600 and 0.800 x_{CTAB} solutions at 20 mmol·kg⁻¹ in D₂O, at 20% liquid fraction with air containing traces of C₆F₁₄ as dispersed phase..... 82

List of tables

Table 1 - Relation between CPP and c , and probable surfactants self-assembly. Adapted from ^[12]	22
Table 2 - Ways to express the amount of surfactant in solution during this work.....	37
Table 3 - Summary table of of aggregate size distribution and respective frequency for samples 0.667, 0.750, 0.800 and 0.900 x_{CTAB}	57
Table 4 - Zeta potential as a function of the x_{CTAB}	58
Table 5 - cmc and surface tension on cmc for different x_{CTAB}	60
Table 6 - Interaction parameter β as a function of x_{CTAB}	61
Table 7 - Summary table of fitting parameters for samples 0.100, 0.450, 0.500 and 0.510 x_{CTAB} using form factor for vesicle shape.	67
Table 8 - Summary table of fitting parameters for samples 0.590, 0.600, 0.700 and 0.750 x_{CTAB} using form factor for rod shape.....	67
Table 9 - Summary table of fitting parameters for samples 0.100, 0.450, 0.500 and 0.510 x_{CTAB} using form factor for spherical shape.....	68
Table 10 – Aggregation behavior for different catanionic mixtures. M = micelles, sM = spherical micelles, eM = ellipsoidal micelles, R = rod-like micelles, V = vesicles, L = lamellar phase, L.C. = liquid crystalline phase, P = precipitate, C.L. = clear liquid, MPh = multi-phase region, I = isotropic phase, 2Ph = two phase region. ^{+/-} indicates cationic- rich or anionic-rich respectively. x_+ indicates molar fraction of cationic surfactant.	73

Acronims and symbols

cmc – critical micellar concentration
CPP – critical packing parameter
CTAB – cetyl trimethylammnium bromide
DIC – differential interference contrast
DLS – dynamic light scattering
DTAB – dodecyl trimethylammonium
N.A. – numerical aperture
QELS – quasi elastic light scattering
SDS – sodium dodecyl sulfate
SOSo – sodium octylsulfonate

x_{CTAB} – CTAB molar fraction
 γ – surface tension
 A – area
 P – pressure
 V_l – liquid volume
 V_f – foam volume
 H – foam height
 η – viscosity
 k – dimensionless permeability constant
 R – bubble radius
 g – gravity acceleration
 θ – angle
 F – force
 L – length
 G – Gibbs energy
 S – entropy
 T – absolute temperature
 V_c – volume of the hydrophobic chain
 a – head group surface area
 L_c – length of the hydrocarbon chain
 R_1 – radius of curvature 1
 R_2 – radius of curvature 2

f – activity coefficient
 β – interaction parameter
 x_1^m – molar fraction of surfactant 1 in the aggregate
 ϕ - liquid fraction
 λ – wave length
 n – refractive index
 q – wave vector
 D – diffusion coefficient
 τ – relaxation time
 R_h – hydrodynamic radius
 K_b – Boltzmann constant
 ζ – zeta potential
 ξ_0 – permittivity of free space
 ξ_r – dielectric constant
 k_s – scattered wave vector
 k_i . incident wave vector
 ρ_p – scattering length density of the particle
 ρ_m – scattering length density of the matrix
 μ_e – electrophoretic mobility
 N_p – number of particles
 V_p – volume of a particles
 $P(q)$ – form factor
 $S(q)$ – structure factor.

1 Introduction

1.1 Introduction to self-assembled systems and foams as colloidal systems

Surfactant self-assembled structures and foams are the key topics throughout this work. Both of them are colloidal systems, and therefore interfacial properties emerge with great importance to understand the goal of this project. Colloidal systems are solutions or dispersions containing particles which possess at least one dimension within the range of a few nm to a few μm . Due to the small size of these particles, the surface area to volume ratio of the material is extremely high, so interfacial phenomena are dominant in this kind of systems. Because of this, it is of main importance to understand both the colloidal and interfacial properties of the systems under study in this work.

1.2 Surfactant solutions

1.2.1 Surfactants

Surfactants, also known as surface-active agents, are characterized by their natural tendency to occupy an interface, changing significantly the physical properties of that boundary ^[1]. The molecular structure of surfactants is the main contribution for their properties. These molecules are composed by at least two distinct parts (Figure 1). One part, called lyophilic, is soluble in a specific solvent whereas the other part, called lyophobic, is not. When the solvent is water, which is the case in this work, the lyophilic part is called hydrophilic and is commonly referred to as head group, whereas the lyophobic part is called hydrophobic and referred as tail.

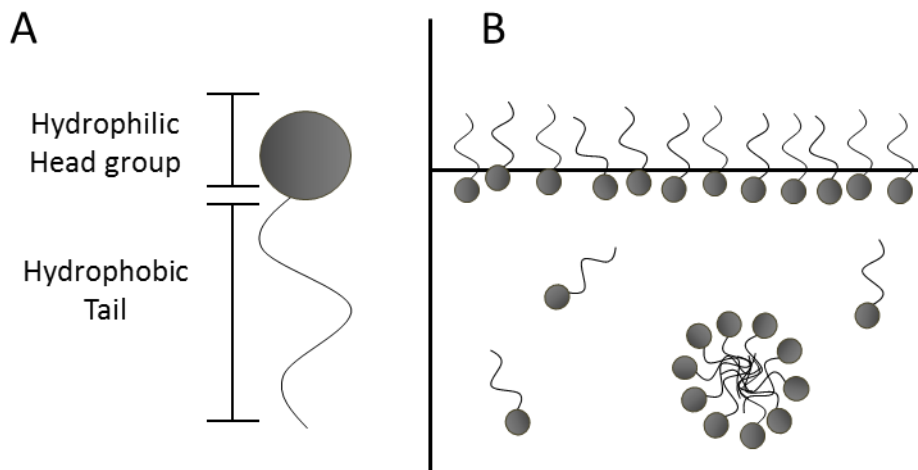


Figure 1 - A) Surfactant representation, B) Surfactant behavior in a solution

Processes of adsorption and self-assembly derive from the structural duality of surfactants and are driven by the reduction of the Gibbs energy of the system.

In order to avoid the unfavorable interactions between water and the hydrophobic part, the surfactant adsorbs at the gas-liquid interface lowering the Gibbs energy of the phase boundary (i.e. surface tension of the liquid). The surface tension of an aqueous solution (or the interfacial Gibbs energy per unit area of the boundary between water and air), decreases as the surface is covered by surfactant molecules. The driving force for this phenomenon is known as the hydrophobic effect. ^[1]

Surfactants form oriented monolayers at interfaces (liquid-gas, liquid-liquid and liquid-solid) and, also importantly, self-assembled structures in the bulk, such as micelles, vesicles, bilayers and liquid crystals. Surfactants have emulsification, dispersion, wetting, foaming and detergency properties.

At very low concentrations, most surfactants are soluble in water in the form of unimers (free surfactants) forming simple solutions ^[1]. Above a certain temperature (Krafft temperature), with increasing concentration, the adsorption at surfaces and/or interfaces becomes stronger until saturation is reached and, the formation of small aggregates takes place – typically these aggregates are micelles.

At sufficiently high concentrations, surfactants are also capable of self-assembling in the form of lyotropic liquid crystals. Different molecular arrangements will give rise to different mesophases that will behave more liquid-like or solid-like phase depending on the concentration of the surfactant and the surfactant structure itself ^[2].

Surfactants can be classified by several properties. Usually they are classified by polar head group charge, polar head group chemical nature, or by the number of head groups and tail structures. In this work, the most relevant approach is to classify the surfactants by the head group charge, as described below:

- **Anionic surfactants** are composed by an amphiphilic anion and a cation (generally an alkaline metal or a quaternary ammonium) (Figure 2). The head group is commonly a sulfonate, sulfate, phosphate or carboxylate. Anionics are used in greater amount than any other surfactant class mostly on detergent formulations and emulsifiers.

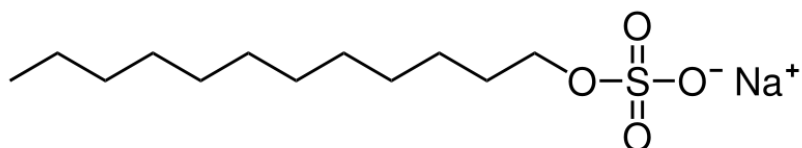


Figure 2 - Example of an anionic surfactant: sodium dodecyl sulfate (SDS)

- **Cationic surfactants** comprise an amphiphilic cation and an anion, most often a halide ion (Figure 3). Usually, in this type of surfactant, the source of the positive charge is nitrogen from an amine or quaternary ammonium groups. Since the production of this type of surfactants is more costly than that of the anionic ones, they are less used overall. Nonetheless, they are of extreme importance in the coverage of negatively charged surfaces like steel, mineral ores, plastics, and fibers, which makes them good anticorrosive agents, dispersants and bactericides.

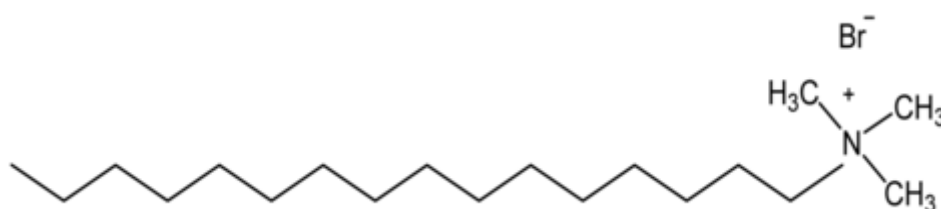


Figure 3 - Example of cationic surfactant: cetyl trimethylammonium bromide (CTAB)

- **Nonionic surfactants** do not dissociate in water. Their hydrophilic group is uncharged and in most cases it is a polyether consisting of oxyethylene units, made by polymerization of ethylene oxide (Figure 4). The most important nonionic surfactants are fatty alcohol ethoxylates. They are used in liquid and powder detergents as well as in a variety of industrial applications, being the second most used type of surfactants overall.

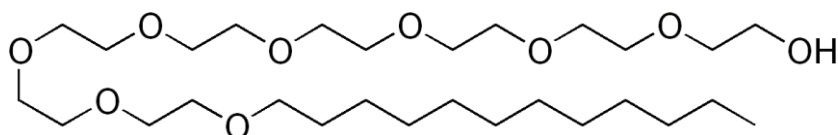


Figure 4 - Example of a nonionic surfactant: Octaethylene glycol monododecyl ether ($C_{12}E_8$)

- **Zwitterionic surfactants** possess a head group with both positive and negative centers (Figure 5). It is the case of synthetic products like betaines or sulfobetaines and natural substances like amino acids and phospholipids. Zwitterionics, as a group, are characterized by having excellent dermatological properties. They also exhibit low eye irritation and are frequently used in shampoos and other cosmetic products.

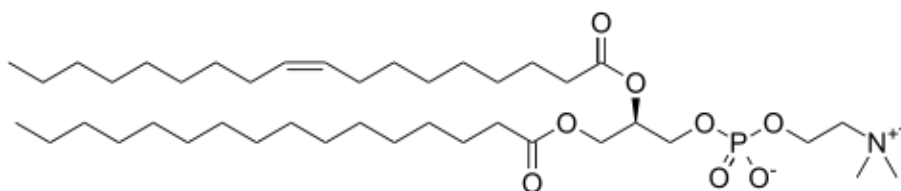


Figure 5 - Example of a zwitterionic surfactant: Palmitoyl-oleyl-*sn*-phosphatidylcholine

- **Catanionic surfactants** are obtained by the pairing of two oppositely charged surfactants and removing the respective counter-ions (Figure 6). In the pair there is electrostatic association between the head groups with no covalent bond between the surfactants. This pairing often results in synergistic effects such as reduction of *cmc* and surface tension at *cmc* compared to the cationic and anionic surfactants alone. Catanionics display unique aggregation behavior that is also different from the original oppositely charged surfactants [3, 4].

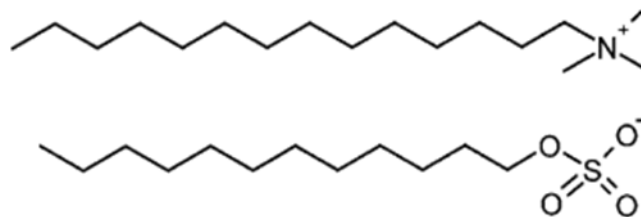


Figure 6 - Example of a cationic surfactant: tetradecyltrimethylammonium dodecylsulphate

Another interesting class of surfactants are gemini surfactants. They are a group that display interesting physicochemical properties when compared to conventional surfactants. All geminis possess at least two hydrophobic chains and two ionic or polar groups, and many possibilities for the spacers (Figure 7) ^[5]. Compared to conventional surfactants of equivalent chain, they present properties like lower *cmc* and surface activity. Due to these characteristics, geminis are applied in diverse applications such as cosmetics, food processing, membranes and gene and drug delivery ^[6].

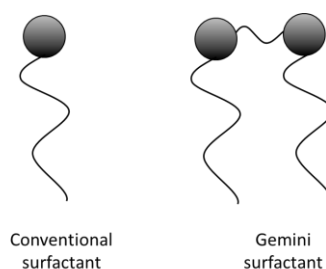


Figure 7 - Representation of conventional (left) and gemini surfactants (right)

Surfactants are present in many systems and environments such as, living organisms, cosmetic products, detergents or mining. Owing to such unique properties and rich phase behavior, these versatile molecules find application in many industrial processes, especially when surfaces are of main concern. The variety of surfactants and the possibilities that arise from mixed surfactant systems are of key importance, both for fundamental and application purposes.

1.2.2 Surface tension

Interfaces constitute the boundary that both connect and separate two different phases. They can be addressed in five different types: solid-solid, solid-liquid, liquid-liquid, solid-gas, and liquid-gas (the last two ones can be also designated surfaces).

Surface or interfacial tension (γ) arises from this contact between the two different media. It is a consequence of the unfavorable interactions between the two phases. Molecules of one phase interact mainly with their neighbors of the same kind creating a cohesive force that delimits one phase from the other. In the case of water in contact with air, surface tension is explained by the cohesive forces inside the liquid originated by the hydrogen bonds between water molecules. The molecules at the surface have less neighbors to interact with and so, overall molecular interactions are stronger inside the bulk than at the surface. To minimize the total interaction energy, the system places as little molecules in the interface as possible, minimizing surface area. Therefore, increasing the surface area implies an increase in Gibbs energy, as it is necessary to expend work to carry out that process.

The reversible work δW_{rev}^σ needed to expand the surface area, A , by dA at constant temperature and pressure is given by:

$$\delta W_{rev}^\sigma = \gamma dA \quad [1]$$

The proportionality constant between the reversible work required for surface expansion and the increase in surface area, at constant pressure and temperature, is called surface tension.

Variation of total Gibbs energy of a system with only one component can be written as:

$$dG = -SdT + VdP + \gamma dA \quad [2]$$

For constant temperature and pressure surface tension can be defined in terms of Gibbs energy by equation 3.

$$\gamma = \left(\frac{\partial G}{\partial A} \right)_{T,p} \quad [3]$$

The variation of the surface tension with the presence of surfactant molecules at the interface may be rationalized by the Gibbs adsorption model (equation 4) ^[1, 7].

$$d\gamma = -\Gamma RT d \ln(a) \quad [4]$$

Where Γ is the surface excess of the solute, R is the ideal gas constant, T is the absolute temperature and a the optimal area occupied by the polar head-group in the polar/apolar interface.

1.2.2 Surfactant self-assembly

Surfactant molecules self-assemble in organized structures that can be of various forms and sizes depending on surfactant and solvent characteristics. Self-assembly starts when the adsorption on the interfaces is no longer thermodynamically favorable. The concentration at which aggregates, termed micelles, start to form is called critical micellar concentration (*cmc*).

1.2.2.1 Critical Micellar Concentration (*cmc*)

The *cmc* is an important quantity for many applications of surfactants because not only it gives information on the concentration required to form aggregates, but also on the free surfactant concentration in solution.

cmc is characteristic of each surfactant and depends on several factors such as the chemical nature of the head group, hydrophobic tail length, temperature, ionic strength, surfactant concentration, and addition of cosolutes [8].

It is well known that most physicochemical properties of surfactant solutions vary markedly below and above a certain concentration, the *cmc*. Below this concentration, ionic surfactants behave essentially as strong electrolytes. Above *cmc*, the properties change markedly, indicating that a highly cooperative association processes takes place. This is well illustrated in figure 8 [9].

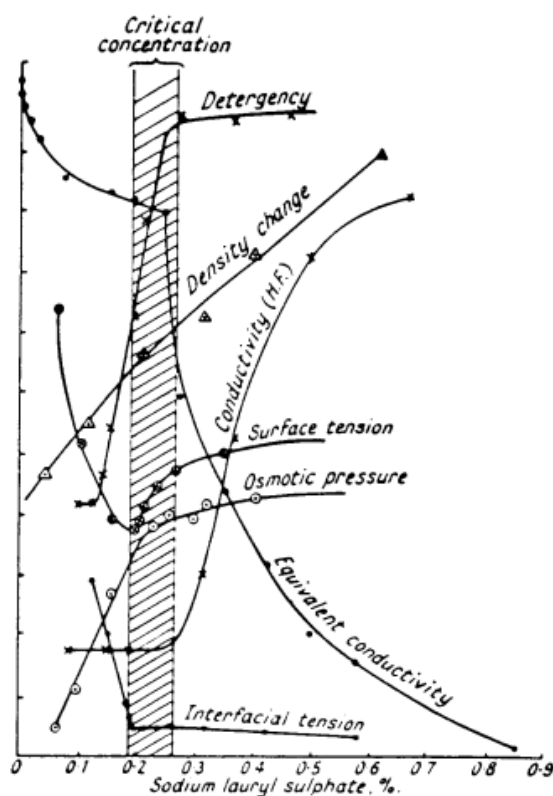


Figure 8 - Illustration of the notorious variation for different physicochemical properties of surfactants solutions before and after *cmc*. Adapted from [9]

The main reason for surfactants to self-assemble is the hydrophobic effect. Due to the poor interaction between alkyl chains and water molecules, it is highly unfavorable

to maintain contact surface between these two components. Water molecules reoriented themselves around this surfaces creating an organized structure termed clathrate cages that restrict the rotational and translational motion of the water molecules exerting a huge entropic penalty. To overcome this penalty, surfactants aggregate themselves in such a manner that the hydrophobic part of the surfactant has the minimum possible contact with water molecules. It is a fine balance between a strong entropic term and an enthalpic term whose sign is temperature dependent [1, 8, 10].

1.2.2.2 Krafft Temperature

Krafft temperature is the temperature at which the surfactant solubility matches the *cmc* (Figure 9). In other words, if the temperature is not high enough, the surfactants will start to precipitate before they can start aggregation. Aggregate formation in solution is linked with the sharp increase in solubility at the Krafft temperature [11].

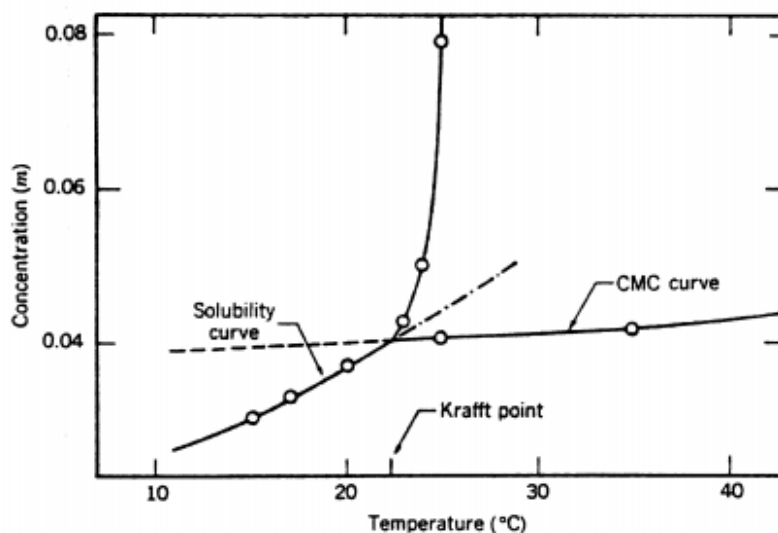


Figure 9 – Schematic representation of the Krafft point for a certain surfactant [8].

1.2.2.3 Packing parameter and spontaneous curvature

Surfactants self-assemble to form aggregates that can be of various types. The type of aggregate that a surfactant will form depends on the geometry that the molecule acquires in a certain environment and how the molecule is able to be packed with other molecules.

In order to predict and rationalize the type of aggregate structure that a certain surfactant will likely adopt in solution, one must consider molecular parameters (hydrophobic chain length and volume and polar head group surface area) and intensive variables (e.g. temperature and ionic strength).

A simple and common concept to rationalize surfactant self-assembly behavior with surfactant geometrical shape is the critical packing parameter (*CPP*). It relates the surfactant molecular shape in certain conditions with a certain type of aggregate likely to be formed. It is given by equation 5 and it allows the prediction, to a certain extent, on how the aggregation will change with intensive parameters.

$$CPP = \frac{V_c}{a \times L_c} \quad [5]$$

V_c and L_c are the volume and the length of the hydrocarbon chain, respectively, and a is the optimal area occupied by the polar head group in the polar/apolar interface. The values of V_c and L_c can be calculated using equations 6 and 7 respectively, where n_{CH_2} is the number of CH_2 groups and n_{CH_3} the number of methyl groups.

$$V_c = 0.027n_{CH_2} + 0.055n_{CH_3} \quad [6]$$

$$l_c = 0.13n_{CH_2} + 0.15 \quad [7]$$

Parameter a is the most difficult to quantify since, for the same molecule, it depends on the solution conditions like temperature, pH, salt concentration or additives. The values that *CPP* assumes will dictate the kind of aggregate likely to be formed as shown in Table 1.

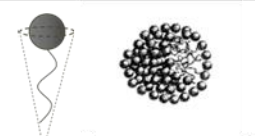
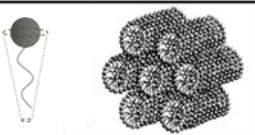
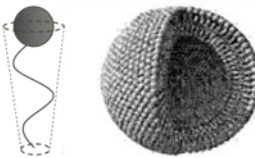
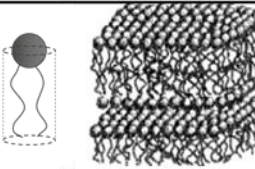
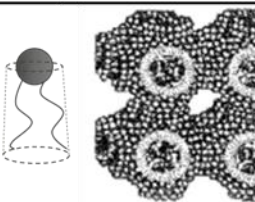
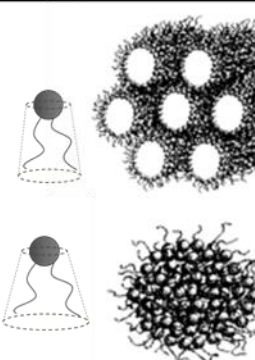
Another model to rationalize self-assembly is the *flexible surface model*. It considers the surfactant film to be a surface with intrinsic interfacial tension and elastic properties^[10]. The bending properties are characterized by the curvature bending constants. c is the mean curvature of the film, R_1 and R_2 are the principal radii of curvature in perpendicular directions, c_1 and c_2 are the principal curvatures.

$$c = \frac{1}{2} \left(\frac{1}{R_1} + \frac{1}{R_2} \right) = \frac{1}{2(c_1 + c_2)} \quad [8]$$

It is established by convention that the curvature towards water is positive whereas curvature away from water is negative. Hence positive curvature will give rise to direct phases and negative curvature to inverted phases.

The spontaneous curvature that the film acquires is the configuration that minimizes the Gibbs energy of the system. This quantity can be related qualitatively to the *CPP* as shown in Table 1.

Table 1 - Relation between *CPP* and *c*, and probable surfactants self-assembly. Adapted from [12].

CPP	<i>c</i>	Aggregate structure	Characteristics
$< 1/3$ Micellar Solution	$1/R$		- Generally spherical but also they can adopt other geometries like discs, prolates, oblates and rods. - Optical and structural isotropy
$1/3 < CPP < 1/2$ Hexagonal Liquid crystal	$1/2R$		- Cylindrical micelles in hexagonal arrangement - Optical and structural anisotropy
$1/2 < CPP < 1$ Vesicular structures			- Hollow spherical aggregates with a bilayer membrane. - Optical and structural isotropy except for multilamellar vesicles, which can present optical anisotropy
≈ 1 Lamellar liquid crystal	0		- Anisotropic phase formed by bilayer layers separated by solvent
≥ 1 Cubic liquid crystal	$-1/R$		- Micellar aggregates organized in cubic geometry (cubic discrete phase, I) or bicontinuous film containing hydrophilic and hydrophobic domains (bicontinuous cubic phase, V) - Optical and structural isotropy
> 1 Inverted hexagonal liquid crystal Inverted micellar solution	$-1/R$		- They have the same geometry as the direct phases but with the surfactants "upside-down". The tail are towards the solvent.

With this simple model of analyzing surfactant packing, it is possible to predict qualitatively the type of change in structural behavior that can be expected when changing the environment conditions.

1.2.2.4 Salt addition

The presence of salts have great influence on both *cmc* and *CPP*, especially for ionic surfactant solutions. The surface area of the head group in an aggregate is dependent on the electrostatic repulsion between adjacent molecules. The ions from the salt do not favor the dissociation of the ionic surfactant and lead to a “contraction” of the counterion cloud in the aggregates leading to screening effect on the head group charges, thus increasing the *CPP* and reducing the *cmc* ^[1, 10].

1.2.2.5 Temperature

Nonionic surfactants are considerably more affected by temperature than ionic surfactants, for which temperature has low effect on *CPP* or *cmc*. For nonionics, of C_nE_m type, temperature has great influence. Increasing temperature will lead to dehydration of the hydrophilic head group, reducing its interaction with water, and leading to a reduction in the *CPP* and *cmc* of the surfactant.

1.2.2.6 Cosolutes

Cosolutes with lower molecular weight than the surfactant, produce changes in the *cmc* to different extent depending on cosolute polarity ^[1]. Both an increase and a decrease in *cmc* are possible. Small or moderate increases are observable with the addition of highly water-soluble compounds. A decrease in *cmc* upon addition of uncharged molecules is very common and is well illustrated by the addition of simple alcohols. The hydrophobic character of the alcohols lead these molecules into the micelles, stabilizing them.

1.2.2.7 Concentration of surfactant

With increasing surfactant concentration, the available volume for the molecules in water is lower, hence the interaction between aggregates will be stronger. This leads the surfactants to pack in a more favorable way to occupy the available volume. In the

case of ionics, for each surfactant added to the solution, there is an increase of the counter ions concentration that bring about similar phenomena as described for salt addition. These effects increase the *CPP* and as a consequence, surfactants organize in different ways. This can be described by Fontell's scheme that explains the natural evolution of self-assembled structures with increasing amount of surfactant (Figure 10).

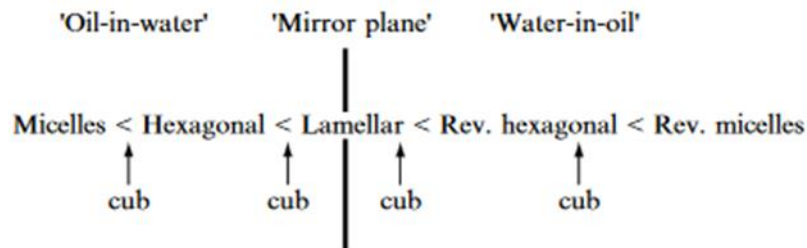


Figure 10 - Fontell scheme for the dependence of surfactant liquid crystalline structure on composition, illustrating the symmetry of curvature location of cubic phases. Adapted from [1]

1.2.3 Catanionic mixtures

A mixture of surfactants can bring about significant changes in surfactant aggregation behavior even if one of them is present only in small quantities. Two surfactants with different packing parameters will interfere with each other causing a change in the overall curvature of the system that is different from the one of each surfactant separately. Mixed surfactant solutions have been the focus of considerable research interest due to their frequent use in industry and pharmaceutical formulations. Compared with the individual surfactants, mixtures exhibit different surface activity and aggregation behavior [13].

Mixtures of surfactants can be understood assuming ideal mixing where the *cmc* of the mixture is then given by [1]:

$$\frac{1}{cmc} = \sum_{i=1}^m \frac{x_i}{cmc_i} \quad [9]$$

Although this relation is important to understand ideal mixing behavior, it is not enough to evaluate the *cmc* of most mixture of surfactants with different head groups which deviate from ideal behavior. In such cases, the *cmc* of the mixture can be

estimated from the individual *cmc* and activity coefficients, f_1 and f_2 , of the surfactants through equation 10.

$$\frac{1}{cmc} = \frac{x_1}{f_1 cmc_1} + \frac{1-x_1}{f_2 cmc_2} \quad [10]$$

The activity coefficients can be obtained by the regular solution theory from:

$$\ln(f_1) = (1-x_1^m)^2 \beta \quad [11]$$

and

$$\ln(f_2) = (x_1^m)^2 \beta \quad [12]$$

Where x_1^m is the molar fraction of component one in the micelle, and β is an interaction parameter, quantifying the net interaction between the surfactants in the micelle. Positive values of β indicate net repulsion between both species and negative values of β indicate net attraction. If β is zero the activity coefficients are one and there is ideal mixing. The β parameter can be interpreted as an energetic parameter that represents the excess Gibbs free energy of mixing given by equation 13, where w_{ij} is the interaction parameter between the i and j surfactants, k the Boltzmann constant and T the absolute temperature [14].

$$\beta_{12} = \frac{w_{12} - (w_{11} + w_{22})/2}{kT} \quad [13]$$

Surfactant synergistic behavior happens when the lowering in the *cmc* of the mixture is higher than the predicted by ideal mixture ($\beta < 0$). Synergism in oppositely charged surfactants is stronger than in other types of surfactant mixtures since the mixtures of oppositely charged surfactants enable the neutralization of charges in the aggregates. It also permits the release of the counter ions leading to a large increase in entropy of the system [15].

Catanionic mixtures are aqueous mixtures of surfactants where the head groups are oppositely charged. The electrostatic interaction between head groups has a screening effect on the charges and change dramatically the surface area of the surfactant, thus changing the *CPP* of the mixed surfactant layer. The screening effect is necessarily correlated with the proportion between the two surfactants and tends to a maximum as it approaches equimolarity. Therefore, adsorption, *cmc*, phase behavior, and other properties of the mixture are tremendously affected by the surfactant mixture

ratio. In cationic mixtures, as well as in surfactants in general, these properties are also affected by the total surfactant concentration and molecular structure [15, 16, 17].

As mentioned above, by varying the molar ratio between the single surfactants of a specific cationic system, the *CPP* also changes permitting the occurrence of many different forms of aggregation even if they are not present for the individual systems [15, 18]. Regarding the example of DTAB/SDS system [18], just by varying the mixture ratio, at high dilutions, it is possible to observe small spherical micelles, for low DTAB molar fractions that increase in size to large thread-like micelle as the DTAB molar fraction increases. One can also find multiphase regions, and two-phase regions where vesicles and precipitate coexist. This rich phase behavior is found in many other cationic systems [15, 19, 20].

One of the most researched topics in cationic mixtures is the appearance of thermodynamically stable vesicles. Traditionally, this kind of structures are prepared by sonication, thin-film hydration or high-pressure extrusion, whereas for other situations it may be sufficient to vortex-mix or just vigorously shake a mixture to accomplish vesicle formation [21]. As these types of aggregates are of great importance to many applications such as pharmaceuticals or nanotechnology, the appearance of thermodynamically stable vesicles in cationic mixtures has led to intense research on this topic.

1.3 Foams

Foams are colloidal systems made up by large amount of bubbles interacting with each other. When bubbles are packed, as it happens in foam, two bubbles meet in a film, films meet in plateau borders and plateau borders meet in nodes. Such complex network gives this state of matter remarkable properties.

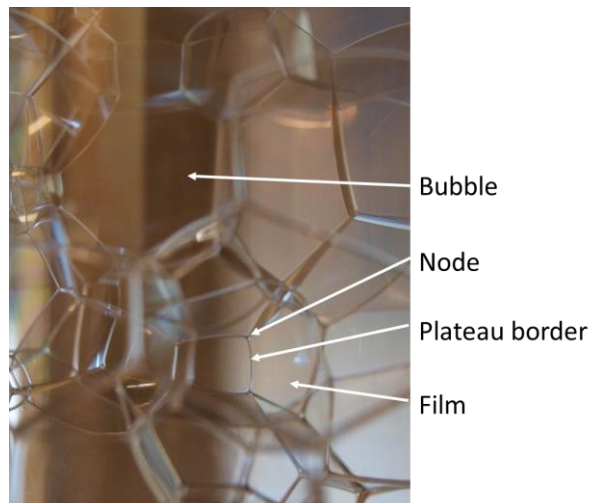


Figure 11 - Structure of a typical dry foam

For foams to exist it is needed a liquid, a gas and a foaming agent. This work deals with liquid aqueous foams which consist in a dispersion of air in water. Their properties can be very varied (elastic or viscous, translucent or very opaque etc.) and depend on the size of the bubbles, the wetness of the foam and the chemicals used to make it. The differences are easily illustrated by our daily life, such as sea foam, chocolate *mousse* or washing products.

1.3.1 Daily life examples and industrial applications of foams

Foams are associated with many hygiene products that can be found in almost every house in the modern society such as dishwasher, shampoo or shaving cream. Despite this association, it is not clear if foams are a measure of cleaning efficiency or just a sub product of the cleaning process. In fact, manufacturers try to suppress foams in mechanical cleaning (washing machines and dishwashing) with anti-foaming agents in order to avoid foam overflowing. Although it is not import for cleaning itself, foam is extremely useful when dealing with vertical surfaces, such as cleaning walls or shaving because it is elastic at small shear, therefore stays on the surfaces allowing better and longer coverage.

Certain beverages are also strongly associated with the presence of foam. In beer for example the foam is so important for the consumer that a great deal of beer advertising focus on how the foam forms and stays in the top of a bottle or a glass. In champagne although the foam is more delicate, it is so important that an expert can tell about the quality of the wine by looking at the foam alone. In champagne and certain beers, the foam formation relies on the release of gas from the supersaturated liquid that degases when the container is opened. In a cappuccino, the long lasting foam seen at the top is stabilized by proteins present in the milk.

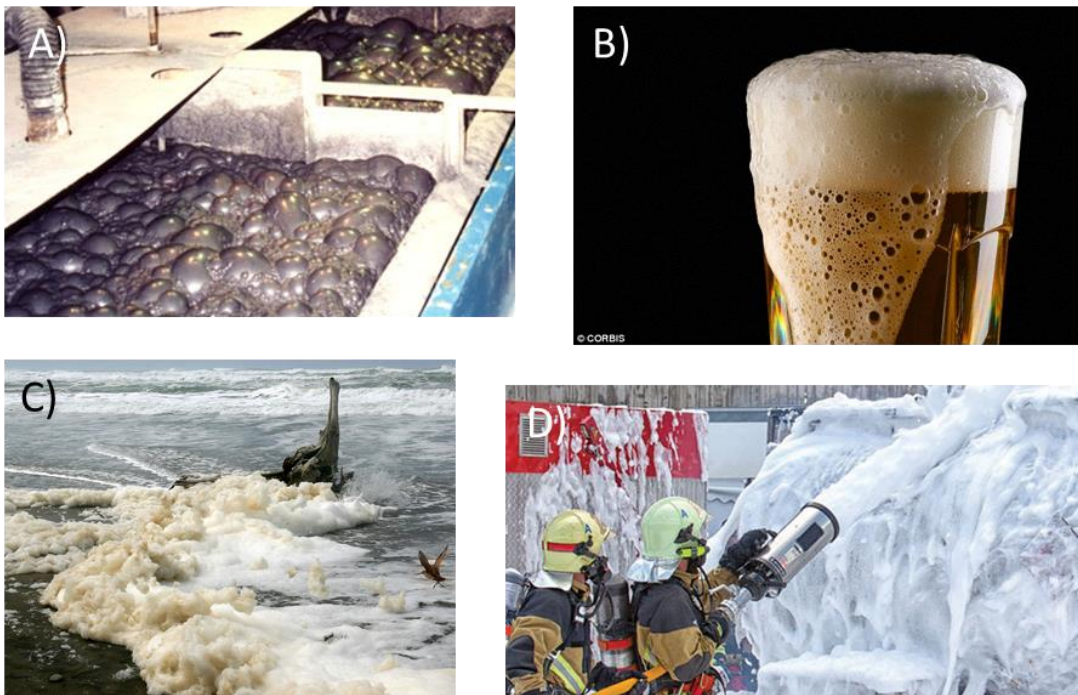


Figure 12 - Examples of foams. A) Mineral flotation; B) Beer foam; C) Sea foam; D) Firefighting foam. Adapted from ^[22].

This smooth and light material is also present in food industry mainly under the form of solid foams. Bread, one of the most common food products in the world, is a solid foam. The yeasts produce carbon dioxide which is trapped in small air pockets and through thermal treatment the bread solidifies. Chocolate or fruit *mousse* are well known desserts that are foams themselves.

In certain conditions it is possible to find foam forming “spontaneously”. When a liquid containing a foaming agent is mixed in such a way that the air is incorporated in it, a foam is created. This is the case in the bottom of a waterfall or the sea. Naturally these foams are ephemeral but in the presence of surfactants from pollutants or plankton they can last long as is the example of the “white-horses”. Hence the presence of foam in the sea is a good indicator of contamination (natural or industrial) by surfactants.

Mineral flotation is a major application of foam properties. The principle of flotation is based on the wetting properties at the liquid/air interfaces. It is possible to optimize the physicochemical conditions so that the mineral grains are trapped by the interfaces while the gangue remains in the liquid. Foam is used in this process because of its high interfacial area. The ground-up rock and mineral are placed in large tanks (height and diameter of several meters). Two types of surfactants (at least) are added: those that control the affinity of the mineral for the interface and those that cause the mixture to foam. Air is injected at the base while the mixture is vigorously mixed in a way that favors encounters between bubbles and particles. A foam is thus continually formed and rises to the surface of the tank before spilling out. It brings with it the mineral, attached to the bubbles.

In fire-fighting it is necessary both to extinguish the fire and to isolate the combustible. Foams are able to extinguish burning hydrocarbons more effectively than water due to their low density and because they float and thus isolate the fuel from oxygen in the air.

Sometimes, foam formation is undesirable for certain industrial processes. Such foam appears for example in the settling tanks or during the manufacturing of glass, steel, pulp or water color paints. In these cases there are methods, usually involving anti-foaming agents to avoid the foaming process ^[23].

1.3.3 Formation

Foam formation requires energy input for the creation of surfaces is energy costly and so, it does not occur without an energy source.

There is not a universal method to generate foam. The type of foam produced will depend strongly on the used method. Different methods allow making foam in different ways that allow more or less polydispersity, bigger or smaller bubble size, higher or lower liquid fraction. Since foam properties depend so much on these parameters there is a large number of methods to produce foams.

Foams can be generated by either dispersion or expansion methods. In dispersion methods, the discrete phase of the future foam is initially available as a large volume of gas. Such methods rely on the mixing of liquid and gas with an input of energy, as in shaking, whipping or pouring. Here a common technique is bubbling air through

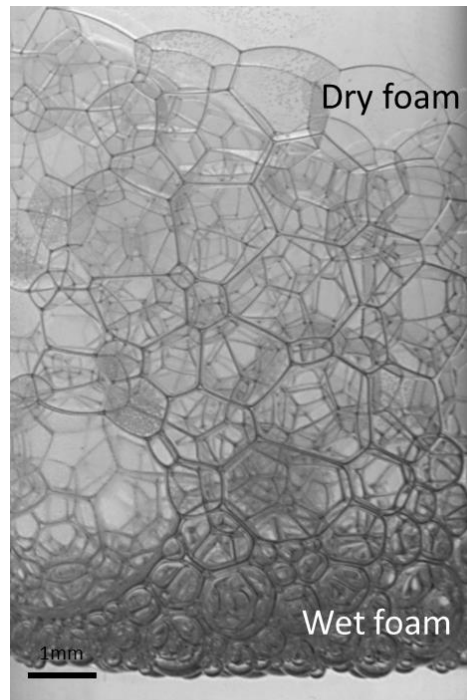
small orifices such as capillaries or drilled plates resulting in size controlled bubbles whose size depends mainly on solution properties, orifice dimensions and gas flow rate. With methods like bubbling with a needle or microfluidics, essentially monodisperse foams can be created.

In expansion methods the air that will be encapsulated in the bubbles is initially present as a solute. Foam results from generation of local gas pockets within the solution. Properties of the whole system have to be changed in such a manner that the solution becomes supersaturated with the gas. Gas can be generated chemically (chemical generate fire-fighting foams) or by microbiological processes (fermentation) or by lowering the entire pressure of the system (soft drinks) ^[24].

1.3.4 Structure

The structure of foams is characteristic and easily recognized (Figure 13). The gas is trapped in small discrete containers referred as bubbles which are surrounded by the continuous phase, in our case the liquid. Foaming agents are the key to avoid the instantaneous collapse of the structure, because they stabilize the interfaces between air and water. Foams of everyday experience are disordered assemblages of bubbles of widely ranging sizes (polydisperse foams).

The polydispersity of a foam is a measure of its bubble size distribution. It affects foam ageing processes like coarsening and is very important in industrial applications since the mechanical properties of the foam will depend on the bubble packing which in turn affects the three dimensional arrangement of the channels and films compromising or enhancing the properties for which the foam was designed for.



Foaming solution

Figure 13 – Profile of a draining foam

Another important quantity to characterize foam is the liquid volume fraction, or just liquid fraction, ϕ (3.1). Where V_l and V_f are the liquid and foam volumes respectively.

$$\phi = \frac{V_l}{V_f} \quad [14]$$

The ratio between the volume of liquid and the total volume of foam will dictate the behavior of the foam and more specifically, the bubble shape. In a typical liquid foam in equilibrium under gravity it is possible to observe that the shape of the bubbles is dependent on the local liquid fraction of the foam. When ϕ is higher than ≈ 0.36 , it is no longer considered a foam but rather a bubbly liquid (the bubbles do not touch and there are no films). This is called the critical liquid fraction (random close packing). Foams with liquid fraction between 0.36 and 0.15 are referred to as wet foams - the bubbles start to lose their sphere shape but there is still a considerable amount of liquid in the plateau borders. From 0.15 to 0.05 the foam is an intermediate between wet and dry and for liquid fractions below ≈ 0.05 the foams are considered dry^[25]. The setting of these values is quite arbitrary^[26] however it helps distinguish between the two opposite behaviors.

Especially for dry foams, there are a set of rules observed by the Belgian physicist Joseph Plateau that characterize the structural organization of foam. He observed that:

- (1) The soap films are smooth and have a constant mean curvature which is determined by the Young-Laplace law;
- (2) The films always meet in threes along edges, forming angles of 120° ;
- (3) The edges meet four-fold at vertices forming angles of $\approx 109.5^\circ$.

Although these rules best describe dry foams and it was shown that some of them can be violated ^[27, 28], they are an important step and basis to understand foam structure, which impacts strongly on its behavior and stability.

1.3.5 Foam ageing

As previously said, foams are thermodynamically unstable which means that their destruction is the natural way to evolve over time. There are three main mechanisms that act on the destabilization of foams: drainage, coarsening and coalescence.

1.3.5.1 Drainage

If a single bubble is considered, the difference in density between the air and the liquid is enough to describe the ascension of the bubble, explaining why liquid appears at the bottom of a foam. But in foams, the bubbles are interacting with each other leading to complex behavior. As mentioned before, bubbles are arranged in a network of films and channels that turn the description of liquid-gas separation too complex to be described by buoyancy.

Due the gravitational influence, the liquid flows through the foam and the foam is said to drain. When a foam is not in equilibrium under gravity, the liquid drains through the foam until the capillary forces are in the same order of magnitude than the gravitational forces ^[29]. As drainage proceeds, the bubbles are progressively distorted from the spherical form, minimizing its surface energy. The drainage of the liquid and the distortion of bubbles leads to motion in the foam, changing the position between the air

compartments. The viscosity of the liquid within the foam will influence greatly this step for it will make the motion more difficult thus preventing the ageing process.

The water flows through the foam along the Plateau borders from the top to the bottom creating a gradient in the local liquid fraction. In the top of the foam, the liquid fraction is lower so the foam is dryer and as a consequence, the shape of the bubbles will resemble more polyhedral whereas in the bottom the liquid fraction is higher so the bubbles will have a spherical shape. In a closed container the liquid flows downwards filling the bottom and pushing the foam upwards.

Foam drainage has characteristic profile that is more intense at the beginning and gets scarce as the liquid leaves the foam. The characteristic time of drainage is given by:

$$T_{drain} = \frac{H\eta}{K\rho gR^2\phi^\alpha} \quad [15]$$

Where H is the foam height, R the average bubble radius, ρ the liquid density, η viscosity, g the acceleration of gravity, K a dimensionless permeability constant and α an exponent between 0.5 and 1. K and α depend on the mobility of the surface layers protecting the bubbles, which depends itself not only on the compression modulus but also on the surface shear viscosity^[30].

From equation 14 it is obvious that the characteristic time of drainage depends on many properties of the foam. Specifically, it is directly proportional to the viscosity of the liquid, which means that the drainage velocity will be inversely proportional to this value.

When foams are formed from surfactant solutions the liquid inside usually bears self-assembled structures. The aggregates in the liquid are often responsible for an increase in viscosity that affects directly foam stability but it can also be the case that big aggregates such as vesicles or micron-sized tubes can accumulate in the nodes where plateau borders meet obstructing the water flow^[31, 32].

Drainage is one of the most important mechanisms of ageing in foams. Once the liquid goes out the amount of film increases and the thickness diminishes, which makes for more efficient gas exchange between bubbles (coarsening) or even the rupture of the films (coalescence)^[25].

1.3.5.2 Coarsening

In a simple way, coarsening consists in the exchange of air between bubbles. Due to the differences in Laplace pressure, gas is transferred from small to big bubbles leading to disappearance of the smaller bubbles and the enlargement of the bigger ones. This difference in pressure, ΔP is a consequence of the surface curvature in bubbles and it is described by the Young-Laplace equation ^[33]:

$$\Delta P = \gamma \left(\frac{1}{R_x} + \frac{1}{R_y} \right) \quad [16]$$

Where γ is the surface tension between the gas and the liquid and R_x and R_y the radii of the two bubbles under consideration. The exchange of gas between bubbles implies the passage of gas through the liquid and depends on the amount of contact surface between bubbles so it is easy to understand that for higher liquid fractions the air exchange rate will be slower than for low liquid fractions. Since the internal pressure of the bubble is inversely proportional to its radius, the differences in pressure between bubbles are higher for polydisperse foams. In a perfectly monodisperse foam coarsening is not expected, but of course this is a hypothetical scenario since in reality there are always small fluctuations in the structure ^[33]. Very important for coarsening phenomena is the physical chemistry of the gas and the surfactant. The solubility of the gas in the liquid phase is a limiting factor for the gas exchange. For example, when the gas in a foam is carbon dioxide, it will coarsen a lot quicker than a foam under the same condition where the gas is air. Since the solubility of CO_2 is higher, the exchange rate of gas will be faster and so will be the ageing of the foam. To increase foam stability often a small amount of hydrocarbon or fluorocarbon gases are mixed with air ^[34]. The low solubility of hydrocarbons and especially fluorocarbons in water reduces drastically the exchange rate gas between bubbles. Also the surfactant has a great influence in this destabilizing mechanism. The denser or looser packing of surfactants on the bubble surface can hinder more or less the gas exchange rate.

1.3.5.3 Coalescence

The event where the film between two bubbles bursts giving rise to a single bubble is called coalescence. When the disjoining pressure is sufficiently low, the surfaces of the film do not repel each other so they collapse, reducing the total number of bubbles. This is the least understood mechanism of foam ageing. It is more important as the bubbles are bigger and the liquid fraction smaller.

1.4 Aim of this project

The areas where cationic mixtures and respective foams can be applied are varied and for this it is important to improve the knowledge regarding these systems. In this work our goal is to investigate and rationalize the phase behavior of the cationic mixture CTAB/SOSo and how this is related with foam formation and ageing. This project intends to expand the understanding of the interfacial properties and self-assembly behavior of cationic mixtures, to improve knowledge about foam stability and how the bulk properties can play a role in the ageing processes of a foam. The use of cationic mixtures in foams have been studied ^[35, 36, 37] with interesting and promising results.

2 Experimental section

2.1 Materials

The surfactants cetyltrimethylammonium bromide (CTAB) and sodium octylsulfonate (SOSO) were used to prepare surfactant mixtures with different molar mixing ratios (Figure 14). Both surfactants were purchased from *Sigma-Aldrich* with $\approx 99\%$ and $\approx 98\%$ purity, respectively. CTAB was washed several times with diethyl ether to eliminate possible contaminants before any usage and SOSO was used without any further purification.

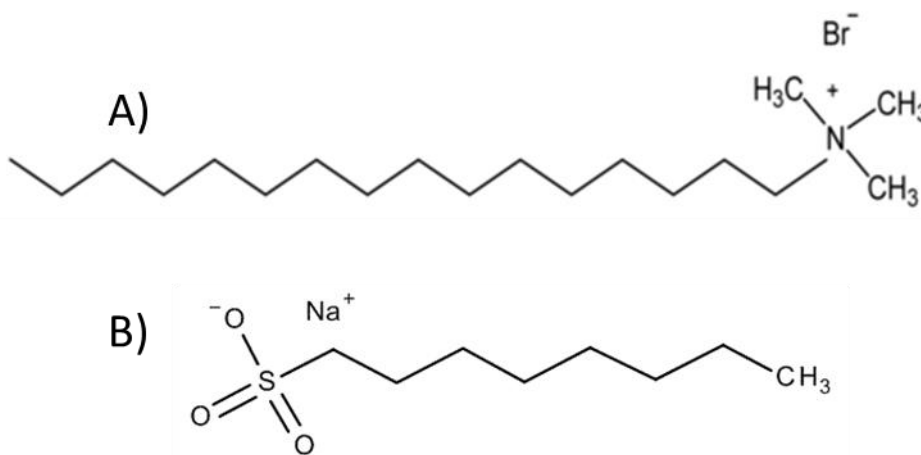


Figure 14 - Representation of: A) CTAB molecule; B) SOSO molecule

2.2 Sample preparation

The solutions used in this work were prepared in glass material washed with acetone, alcohol and ultrapure water several times. Stock solutions of both surfactants were prepared by weighing the solid surfactant in an analytical balance with $\pm 1 \times 10^{-4}$ g precision and adding the necessary volume of ultrapure water (Millipore[™] system). Surfactant mixtures were prepared by addition of mass from the stock solutions of the individual surfactants. The solutions were prepared at least one day before any measurements and subject to homogenization through continuous agitation.

The surfactant composition of the samples will be expressed in different quantities as described in Table 2.

Table 2 - Ways to express the amount of surfactant in solution during this work

Composition	Definition	Units
Molarity	$c = \frac{n_{solute}}{V_{solution}}$	mol·dm ⁻³
Molality	$m = \frac{n_{solute}}{m_{solution}}$	mol·kg ⁻¹
CTAB molar fraction	$x_{CTAB} = \frac{n_{CTAB}}{n_{CTAB} + n_{SOS_0}}$	No units

2.3 Foam generation

In this work, the double syringe method was used to produce foams. The double syringe method is an easy and controlled way to produce foam [38]. It requires two syringes that encapsulate water and air in controlled amounts and force both components to pass by a small constrain (Figure 15). The passage through this constrain incorporates the air in the liquid producing a foam with characteristic bubble size distributions.

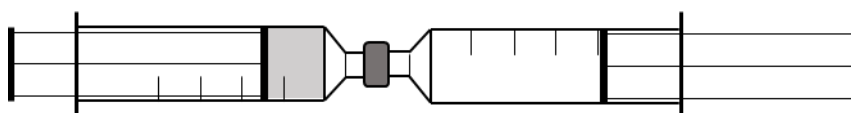


Figure 15 - Schematic representation of the double syringe method

The syringes were washed with ultrapure water several times before the foaming process. The surfactant mixture needed for the foaming was extracted and measured from the glass vials directly with a micropipette, whereas the amount of gas was controlled by the syringe indicators.

To control the ageing processes in the foam, C₆F₁₄ gas was used in SANS and drainage experiments. Air is passed through liquid C₆F₁₄, dragging some of its molecules, and is incorporated in the syringe where the surfactant solution is already set.

2.4 Experimental methods

2.4.1 Tensiometry

There are different experimental methods to measure the surface tension of a liquid and they can be divided in three categories depending on the property being measured [39]: (i) weight methods, in which there are capillary ascension, Wilhelmy plate and du Noüy ring, (ii) shape methods, which include volume of drop, pendant drop and sessile drop, and (iii) pressure methods represented by the method of maximum bubble pressure.

In this work, we used the Wilhelmy's plate method, a simple and precise method from which it is possible to obtain reliable results without theoretical corrections.

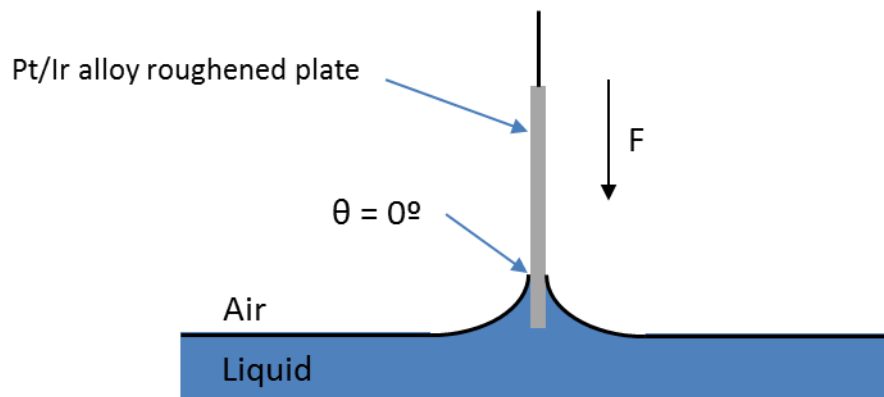


Figure 16 - Representation of the Wilhelmy plate method for surface tension measurements

In Figure 16, one can see a thin vertical plate attached to a balance and immersed on a liquid. The surface tension manifests through the meniscus forming around the perimeter of the plate. The plate is made of platinum or a platinum-iridium alloy as these are inert materials, easy to clean; besides, the plate can be optimally wetted on account of its very high surface free energy, thus forming a contact angle θ of 0° ($\cos \theta = 1$) with liquids.

$$\gamma = \frac{F}{L \cos(\theta)} \quad [17]$$

When the balance is set to zero before dipping the plate, the increase in mass after the immersion is caused by the contact with the surface and by the dragging of the meniscus. This will give rise to a vertical force, F , provoked by the surface. If length of

the plate is known and constant over its height, since the contact angle between the plate and the liquid is 0° , surface tension is easy to calculate by equation 18 ^[40].

Experimental procedure

The surface tension of the individual compounds and catanionic mixtures was measured with a commercial tensiometer Dataphysics, DCAT 11 model, with SCAT 11 software, in order to obtain the *cmc* values for the different mixture ratios. The temperature at which the experiment was carried out was controlled by a thermostatic bath from Julabo. The procedure for the measurement started with careful washing and drying of the measuring glass vessel and the plate, with this last being flamed to remove any remaining impurities. After this process, 25 mL of water were added to the vessel; the measurement is preceded by measuring the surface tension of ultrapure water (to ascertain that the balance remains properly calibrated) at the temperature that the experiment is carried out. After this, small aliquots of the surfactant solution were added to the vase with the help of micropipettes and the value of the surface tension was registered each time after equilibrium was reached. All the solutions were prepared and equilibrated at least one day before the measurements to ensure a good level of mixture between the surfactants.

Data treatment

To obtain the *cmc* value for the analyzed substance, two linear regressions are applied to the data before and after the inflexion point in the curve (as explained in Figure 17) resorting to the function LINEST from Microsoft office excel. The intersection of the two regressions is resolved and the output x value is considered the natural logarithm of the *cmc*.

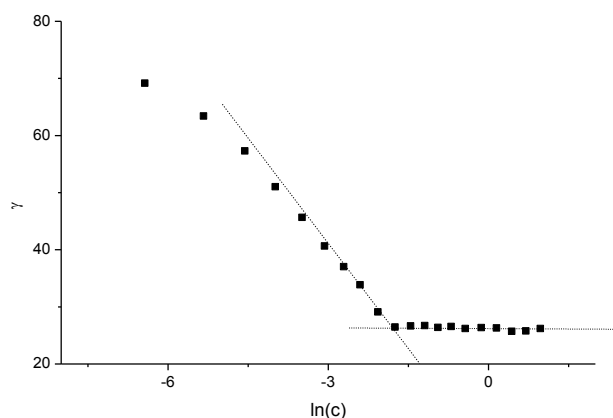


Figure 17 - Graphic representation of the surface tension variation with the natural logarithm of the concentration

2.4.2 Light microscopy

2.4.2.1 Bright field microscopy

Light microscopy is a powerful, quick, and well-established technique to probe objects at the micron scale. This technique relies on a visible light ($400 \text{ nm} < \lambda < 750 \text{ nm}$) emitting source that illuminates the sample. The light transmitted is then conducted through a set of mirrors and lenses that amplify and invert the image to be displayed in the oculars of the microscope or in a digital camera attached to the device and plugged in a computer ^[41, 42, 43].

The wave length of the light used is a limiting factor since it is only possible to resolve objects bigger or of the same order of magnitude in size that the wavelength used. Resolution is the capacity to distinguish two close points as different individual objects. In the case of a light microscope, the resolution (R) is given by:

$$R = \frac{\lambda}{2N.A.} \quad [18]$$

where λ is the light wavelength and N.A. the numerical aperture of the objective that in turn can be calculated from:

$$N.A. = n \sin(\mu) \quad [19]$$

with n being the refractive index of the medium between the sample and the lens and μ represents half of the aperture angle from the objective. The aperture angle is related with the amount of light that the lens is able to collect after the radiation has passed through the sample and get diffracted. The resolution power is affected by the wavelength of the radiation used and light diffraction in the sample ^[41, 42, 43].

2.4.2.2 Differential Interference Contrast Microscopy (DIC)

Relying on a mode of dual-beam interference optics, the DIC mode transforms the fluctuations in optical path length in a sample, into areas of contrast in the sample image (Figure 18). In this technique, the specimen is sampled by pairs of closely spaced rays that vibrate perpendicularly to each other. This separation is generated by a beam splitter (Nomarski prism) between the polarizer and the condenser. When the ray pair

traverse a phase object in a region where there is a gradient in refractive index, thickness, or both, there will be an optical path mismatch between them as they emergence from the sample. The passage through different thicknesses and refractive indexes leads to differences in transmission inside the pair. A second Nomarski prism is placed right after the objectives with the purpose to recombine the ray pair again. Hence the two beams that propagates perpendicular to each other interfere resulting in a contrast enhancement. Beyond the contrast, this technique add some perspective to the aggregates that derives from the optical density of the sample. Because the optical path length is a result of both refractive index and thickness, it is not possible to tell if the phase gradient in the sample is due to differences in one, the other, or both. Amplitude differences in the image should be considered as representing just optical path differences, unless other information about the object is known [41].

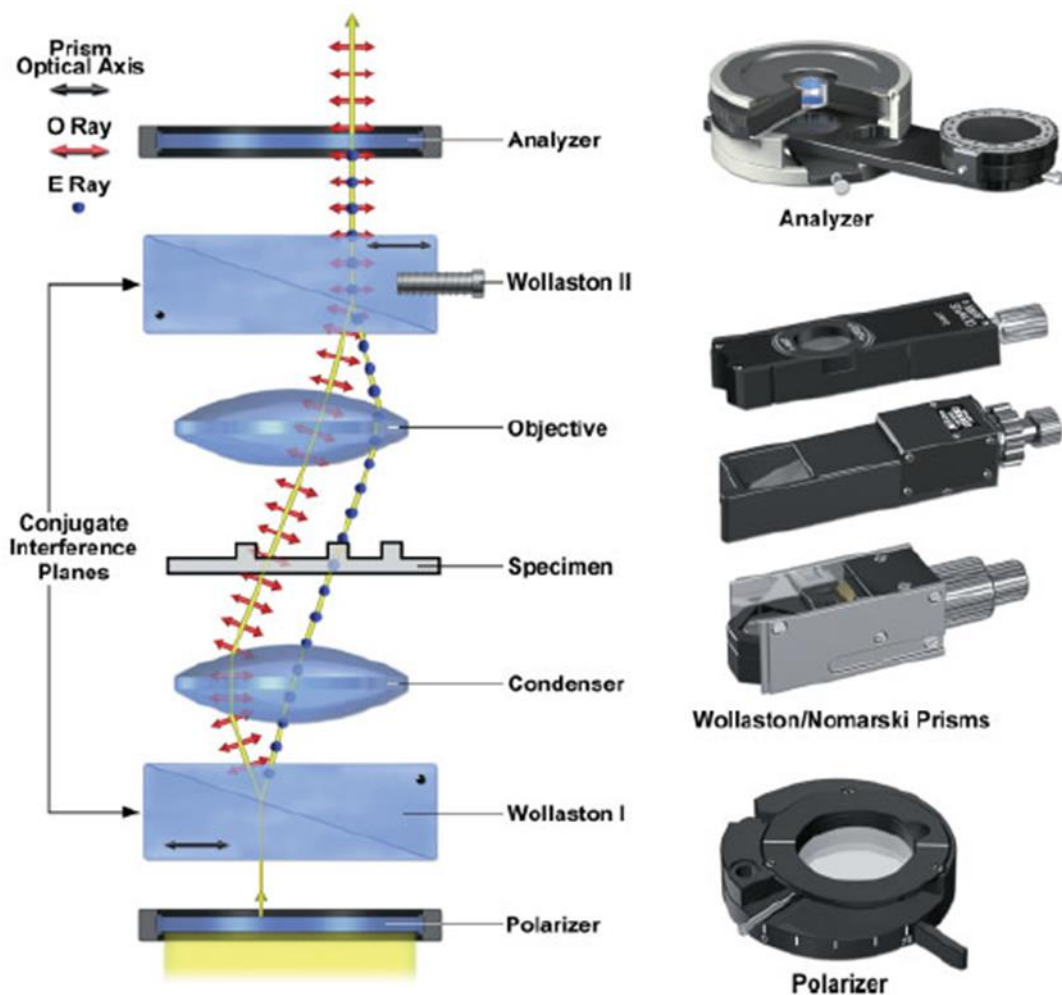


Figure 18 - Schematic representation of a microscope equipped with differential interference contrast system. Adapted from [41]

Experimental procedure

In this work, the samples were visualized in a polarized light microscope Olympus BX51, equipped with differential interference contrast (DIC). The images from the different samples were captured by a digital camera Olympus C5060, coupled to the microscope. Sample observation was carried out by pouring a single drop on a slide, that is covered with a lamella and then both are sealed in order to maintain sample quality.

2.4.3 Dynamic Light Scattering (DLS)

Dynamic light scattering (DLS) or quasi-elastic light scattering (QELS) is a well-established technique used to obtain information about the size and time scales in systems of various complexity. The principle behind this technique is the interpretation of light scattering fluctuations caused by the suspended/solubilized particles in the sample. A schematic representation of a DLS apparatus is presented in Figure 19.

Light scattered by mesoscopic particles in solution produces a random interference pattern. This pattern, in general presents the form of random distributed spots of different sizes called speckles. Particle motion leads to a temporal evolution of the scattered speckle frame since one interference pattern is continuously replaced by another. This evolution is observed as intensity fluctuations over time in a single speckle spot, with a well-defined temporal correlation. The intensity fluctuations are inherently linked with the scatterers' dynamics and, therefore, the temporal correlation functions depend on the particle movement. Thus, the measurable correlation properties of light can be linked to the dynamical properties of particles which in turn, can provide their flow velocity and direction, particle size, density of moving scatterers, among many other properties [44, 45, 46].

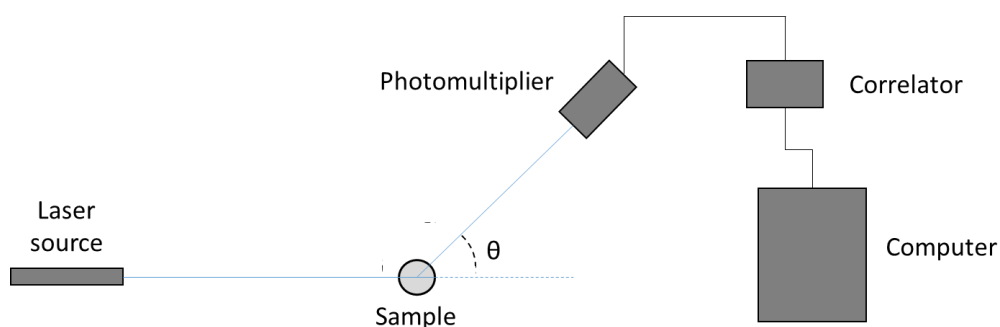


Figure 19 - Schematic illustration of a basic light scattering apparatus

DLS measurements probe how concentration fluctuations relax towards equilibrium at a length scale of q^{-1} , where q is the wave vector defined as.

$$q = \frac{4\pi n_{ref} \sin(\theta/2)}{\lambda} \quad [20]$$

In equation 19 n_{ref} is the refractive index of the medium, θ is the scattering angle, and λ is the wavelength of the incident light in vacuum.

Correlating the intensity fluctuations through the use of an autocorrelation function it is possible to calculate the relaxation time ^[44]. This time is related with the diffusion coefficient (D) of the particles in solution by the equation:

$$\tau^{-1} = Dq^2 \quad [21]$$

Knowing the diffusion coefficient, it is possible to calculate the hydrodynamic radius (R_h) from the Stokes-Einstein relationship ^[44]:

$$D \cong \frac{k_b T}{6\pi\eta_0 R_h} \quad [22]$$

Experimental procedure

The cationic solutions were analyzed for different concentrations with the particle analyzer Malvern ZetaSizer Nano ZS. For the determination of the particle size, population frequencies and respective errors, 1 mL aliquots of each solution were poured in disposable polystyrene cuvettes and analyzed at 27°C. Samples were equilibrated for 120 seconds before analyzed and the tests were repeated 5 times in order to get an average value for the parameter.

2.4.4 Zeta potential

Zeta potential is the potential difference between the dispersion medium and the stationary layer of fluid around the dispersed particle (Figure 20). Since it is extremely difficult to obtain information about the real surface charge of the particle due to solvation phenomena, the most outer layer of the particle in solution (slipping plane) is considered instead.

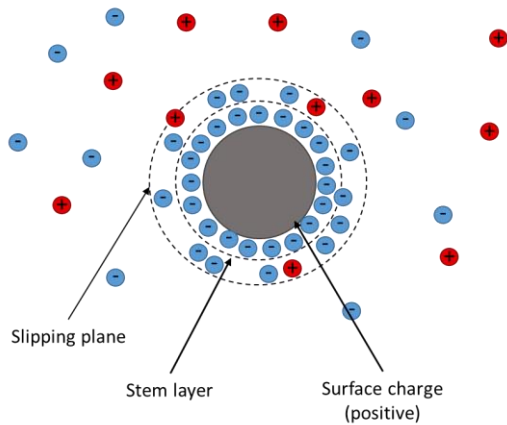


Figure 20 - Schematic representation of surface charge distribution around a positive charged particle

This potential difference rises from the net electrical charge that lies on the region bounded by the slipping plane and depends on the position of the plane. Henceforth this measurement is widely used to quantify the magnitude of the charge. Although zeta potential is neither a measure of the actual surface charge nor of the Stern potential, it is often the only available method to have information about the “apparent” surface charge of the particles [47].

Zeta potential cannot be measured directly but it can be calculated considering the electrophoretic mobility, μ_e , according to the expression [48]:

$$\mu_e = \frac{\xi_r \xi_0 \zeta}{\eta} \quad [23]$$

where ξ_r is the dielectric constant of the dispersion medium, ξ_0 is the permittivity of free space, η is the dynamic viscosity, and ζ is the zeta potential.

In colloidal chemistry, it is very important to have information about the particle stability against aggregation. The zeta potential is a good indicator of this stability since double-layer electrostatic repulsions act against aggregation, and the bigger the zeta potential is, the stronger the ionic repulsions between aggregates will be.

Experimental procedure

Zeta potential was estimated in a Malvern ZetaSizer Nano ZS, where the samples were placed in disposable capillary polycarbonate cells equipped with gold coated electrodes. Samples were equilibrated for 120 seconds at 27° C before analyzed at the same temperature. The tests were repeated 5 times in order to get an average value for the parameter.

2.4.5 Solution rheometry

The study of the mechanical properties of a system is called rheology. In rheology one of the most relevant properties is viscosity for it is a main factor for the characterization of fluid systems. Measuring the viscosity of liquids is not a trivial task because viscosity itself is a gathering of interplaying forces between the particles under motion. Nonetheless, it is possible to do so and in this work we resorted to a rotational rheometer of the “cup and bob” type to measure the viscosity of the solutions [49].

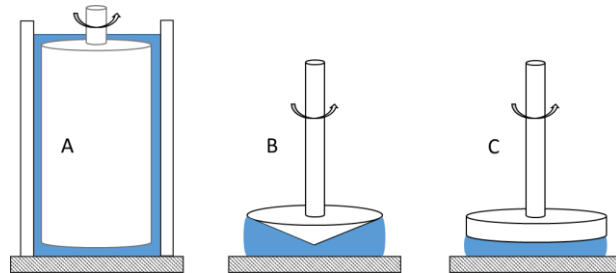


Figure 21 – Schematic representation of three main geometries of rotational viscometers: A) Cup and bob; B) Cone; C) Disc. Adapted from [50].

Rotational viscometers operate in the principle of measuring the force or torque required to move a solid shape in a viscous medium at a defined angular velocity (Figure 21) [50, 51]. To rotate a disk or bob in a fluid at known speed, a force is necessary. The rheometer will determine the force required to the process. 'Cup and bob' viscometers work with a specific volume of sample which is to be sheared within a test cell. The torque required to acquire a certain rotational speed is measured. "Cup and bob" viscometers have two main geometries, known as either the "*Couette*" or "*Searle*" systems. In the first, it is the bob that rotates, and in the second, the cup. This measuring systems require large sample volumes and the cleaning process is more difficult. They may produce problems when performing high frequency measurements because in general they have large mass and large inertia. The main advantage of using these systems is that they can work effectively with low-viscosity samples and mobile suspensions. Their large surface area gives them greater sensitivity and so they will produce good data at low shear rates and viscosities. Due to the large surface area, the double gap measuring system is ideal for low viscosity / low shear rate tests [52].

Experimental procedure

The samples were transferred into a rheometer (Rheoplus, Anton Paar) after at least one day equilibrating and viscosity was measured with a *Couette* geometry in a log ramp

shear rate from 1 to 100 rad/s acquiring 8 points. The cup and bob system used has internal gap thickness of 0.42 mm, external gap thickness of 0.47 mm and the sample volume of 3.619 mL.

2.4.6 Cryogenic Transmission Electron Microscopy (cryo-TEM)

Transmission electron microscopy (TEM) involves the transmission of an electron beam through a sample in a high vacuum environment ($p < 10^{-5} - 10^{-6}$ Pa). This technique is an extremely powerful tool to probe objects at the nanoscale. Using both the dual particle and wave nature of the electron, one is allowed to control the electron wavelength in order to probe such small substrates. TEM samples must be ultra-thin in order to be observable. The image is formed from the interaction between electrons and the sample from where they are transmitted ^[43].

Cryo-TEM is a technique where TEM is used on vitrified samples ^[53]. Since TEM imaging requires high-vacuum it is not possible to observe liquid samples unless they are dried or frozen. More specifically, in the case of aqueous solutions, the samples must be vitrified or else the water crystals formed would destroy the aggregates natural shape and interfere with the electron path making the observation impossible. Vitrification is fundamental to explore aggregates in liquid samples because not only it avoids the evaporation of the solvent but also it arrests the movement of the particles enabling a good focus for the visualization ^[54]. Figure 22 summarizes the procedure schematically.

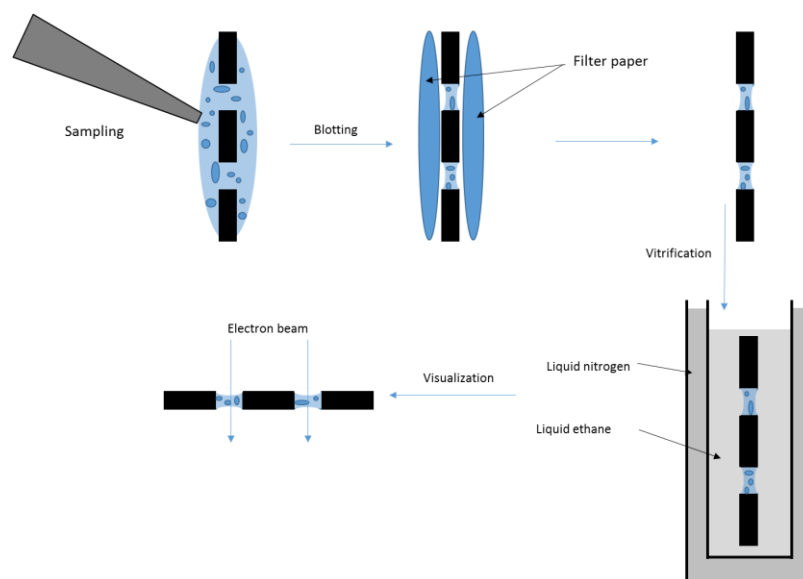


Figure 22 - Schematic representation of sample preparation for Cryo-TEM observation. Adapted from ^[54]

Experimental procedure

Cryo-TEM imaging allowed the visualization of the aggregates present in the solution samples at room temperature (around 25 °C). A small quantity of sample is placed on a copper grid that was previously treated with plasma to acquire small surface charge and facilitate wetting process. The copper grid is in a thermostated chamber at the desired temperature and humidity. The sample in the grid is then blotted to create a thin film. Afterward, the copper grid with the sample is quickly vitrified by immersion in liquid ethane and carefully transferred in liquid-nitrogen environment to the microscope. The samples in this work were imaged with a Philips CM 120 Bio-Twin transmission electron microscope.

2.4.7 Small Angle Neutron Scattering SANS

Neutron scattering offered to colloidal science an extremely powerful tool to probe the colloidal systems at short scale (1 nm – 1000 nm) in its natural state. As in any other scattering technique, the scattering vector, q , is a key parameter. It is the difference between the incident and the scattered wave vectors, $q = k_s - k_i$. The magnitude of q is given by $q = 4\pi \sin \theta / \lambda$, as seen above in the DLS section. The wave vector is a useful quantity because a diffraction peak happens at a certain q that depends both on θ and λ .

Neutrons are scattered by the atomic nuclei and their diffraction depends on the nuclear scattering length density. The scattering length indicates how strongly the nucleus scatters neutrons. An important point about this parameter is that it does not vary systematically with the atomic number. The scattering density varies almost randomly from successive elements and even between isotopes. For example, the scattering between hydrogen and deuterium is completely different, which is one of the main reasons for this technique to be so important in soft matter and polymer science. By switching from H₂O to D₂O the experimentalist is able to emphasize some aspect of the scattering without changing too much the chemistry of the sample ^[55].

Considering a simple case where a dispersion of identical spherical particles in a certain matrix is being analyzed, the observed scattering intensity, $I(q)$ is given by ^[56]:

$$I(q) = (\rho_p - \rho_M) N_p V_p^2 P(q) S(q) \quad [24]$$

Where $(\rho_p - \rho_M)$ is the contrast in scattering between a particle and the matrix, N_p is the number of particles in the sample, V_p is the volume of a particle, $P(q)$ is the particle form factor and $S(q)$ is the structure factor. This expression is only valid for a collection of spherical particles but it is also a good approximation for other shapes where anisotropy is not too high.

The particle form factor is the term that gives the information about particle size and shape. Using appropriate models, it is possible to fit the intensity curves in order to obtain shape and characteristic sizes of the particles. The structure factor, $S(q)$, is the parameter that considers the interaction between particles giving information about the local order of the sample. Scattering objects with different shapes will give rise to different scattering patterns. Some of these patterns are well known, as shown in Figure 23. There are several models concerning shape and form factors that permit an easy fitting for the acquired data given that one has an idea about the shape of the scattering bodies being probed.

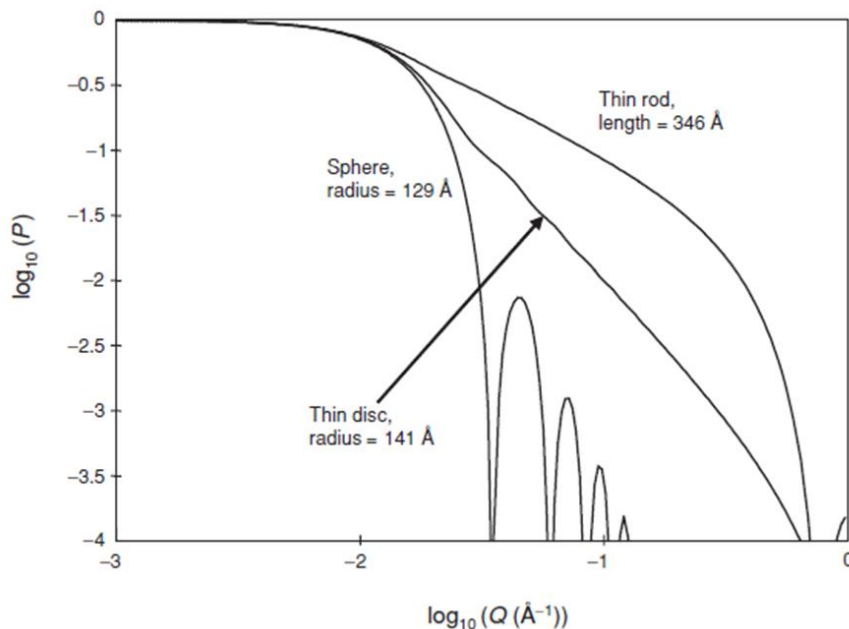


Figure 23 - Form factors for different particle shapes with the same radius of gyration. Adapted from [56]

Experimental procedure

SANS experiments were performed in Laboratoire Léon Brillouin implemented in CEA/Saclay facilities. The neutrons are produced in a nuclear reactor by fission of uranium 235, the same process as in a nuclear power plant. They are cooled in cold moderators to reach the desired energy (cold neutrons). Incoming polychromatic neutrons are monochromatized by a mechanical velocity selector. The neutrons are then collimated with two ^{68}Ni guide elements under vacuum. The BF3 multi-detector, with 128 x 128 cells of 5 x 5 mm², was positioned at 1 m with $\lambda_n = 6 \text{ \AA}$ for high q , 3 m with $\lambda_n = 6 \text{ \AA}$ for Medium q , 5 m with $\lambda_n = 8.5 \text{ \AA}$ for low q and 6.7 m with $\lambda_n = 15 \text{ \AA}$ for very low q distances from the sample in the horizontal direction in its vacuum tube. The instrument is operated by a PC through a menu-driven interface and an image of the data collected are displayed on a color monitor. Samples are analyzed in 1mm high quality quartz cells to be analyzed.

The two dimensional isotropic scattering spectra has been corrected for detector efficiency by dividing the scattering pattern by the incoherent scattering spectra of neat water and has been radially averaged and converted to absolute scale. This treatment was performed using the *Pasinet v2.0146* software. Background has been subtracted, by subtracting the constant value of the incoherent scattering measured at high q values.

2.4.8 Foam Characterization by Photography

Photographic documentation of sample evolution can be of great value to understand the mechanisms that drive the ageing of the samples. By capturing photos in a systematic way it is possible to relate the different characteristics of the sample evolving with the time required to achieve this evolution.

Drainage velocity

To calculate the drainage velocity of a foam one can consider the amount of liquid drained over time. Knowing the dimensions of the container in which the foam is, it is easy to have information about the volume drained in a certain time. With photographic time controlled documentation the volume of liquid drained can be calculated for each time, and drainage velocity can be obtained.

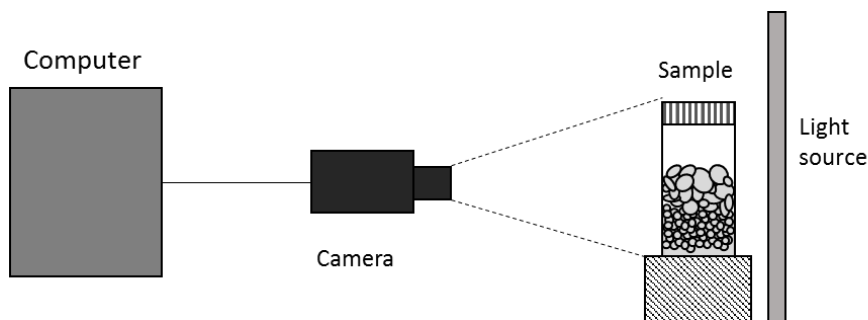


Figure 24 - Schematic representation of the setup used to measure drainage velocity

Aqueous cationic mixture solutions were submitted to foaming processes by the two syringe method. In order to evaluate physical-chemical properties of the said foam and bulk solutions, the samples were foamed at different liquid fractions. The prepared foams are stored, and immediately analyzed, inside 25 mL glass tubes in a homemade assemblage like the one in Figure 24, where foam photos were set to record every 5 seconds in the *uEye* trigger software using a *uEye* camera, regarding foam dynamics and ageing processes. Images were treated using free software *Image J*.

Data treatment

The photographs were sequenced with the software *Image J*. A line of 1 pixel width is drawn in the center of the foam container (that is placed in the same position each photo). In every photo, this line is considered to assemble a new image which is the sequence of the lines picked at each photo. The height of the liquid over time is considered in the transition in color from the liquid to the foam. Converting a vertical sequence of pixels in height and a horizontal sequence in time the drainage velocity is calculated by linear regression of the initial linear region with the help of function *LINEST* from *Microsoft Office Excel*.

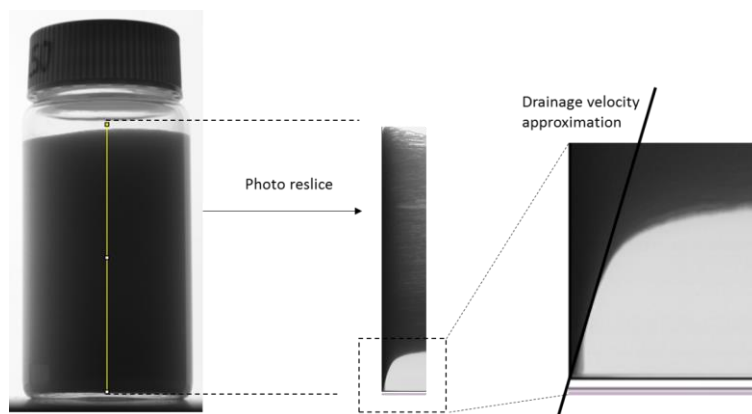


Figure 25 - Procedure to evaluate drainage velocity through photographic documentation

Bubble size

In order to have good statistical information on the bubble size and bubble size distribution, measurements were performed in a homemade photographic device incorporating a uEye camera and moving support that can create a photo assemblage.

The cationic mixture solutions were submitted to foaming processes by the two syringe method at different liquid fractions. The samples were applied over a slide immediately after foaming, diluted with the solution used to produce foam and covered with a lamella. They were transferred to the photographic device and photos acquired. Images are treated and the size of the bubbles analyzed using the free software *Image J*.

3 Results

The presentation of this work will be divided in two main parts. First, the bulk behavior of the CTAB/SOSo cationic mixtures is explored as a function of the CTAB molar fraction (x_{CTAB}) Figure 26. In a second part, aqueous foams of this cationic solutions are studied considering ageing processes and their relation with bulk properties.

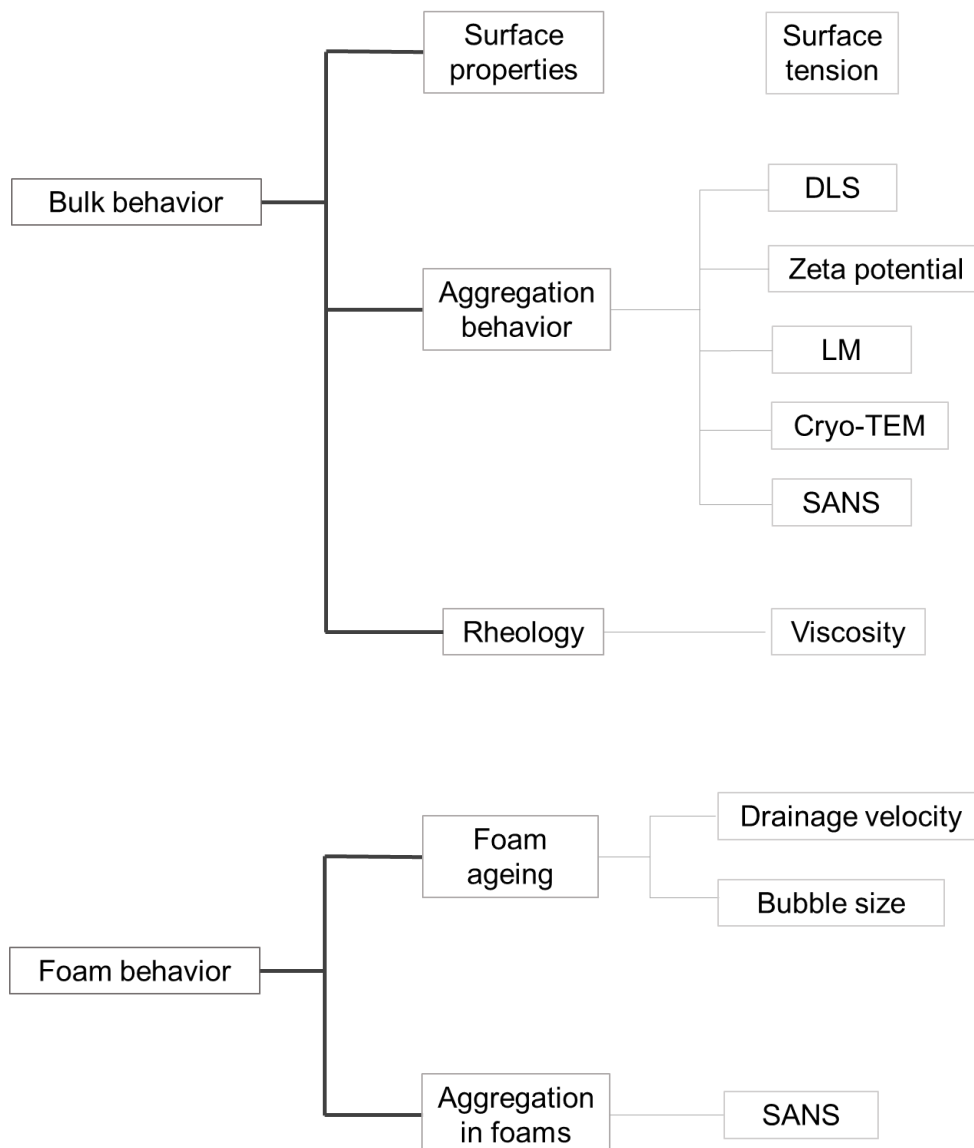


Figure 26 - Scheme of the approach used to characterize bulk and foam behavior of the cationic mixture CTAB/SOSo.

3.1 Bulk behavior

3.1.1 CTAB/SO₂So mixture – macroscopic characterization

Different molar mixing ratios of CTAB/SO₂So were prepared at a total surfactant concentration of 20 mmol·kg⁻¹ using the method described in section 2.1. To designate the relative amount of CTAB and SO₂So in each solution, CTAB molar fractions (x_{CTAB}) will be considered.

From the analyzed samples it is possible to distinguish some features by careful ocular observation (Figure 27). While the cationic-rich samples present a consistent transparency, the anionic-rich ones appear bluish or hazy depending on composition.

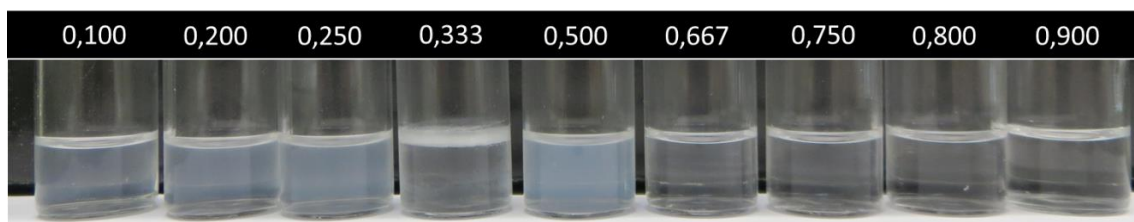


Figure 27 – Visual appearance of CTAB/SO₂So mixtures as a function of x_{CTAB} .

It is possible to have an intuitive notion of the relative viscosity from one sample to another by shaking the solution inside the container and observe how fast bubbles rise in the liquid. From these observations, it can be inferred that: (i) the anionic-rich side has low viscosity with no significant difference between samples, (ii) the cationic rich side has a decreasing viscosity from $x_{CTAB} = 0.667$ to 0.900, and (iii) $x_{CTAB} = 0.500$ sample has some intermediate viscosity between the two extremes. Samples at 0.330 and 0.250 have phase separation (“creaming”). In Figure 28 we present a schematic guide to rationalize the macroscopic behavior of the system.

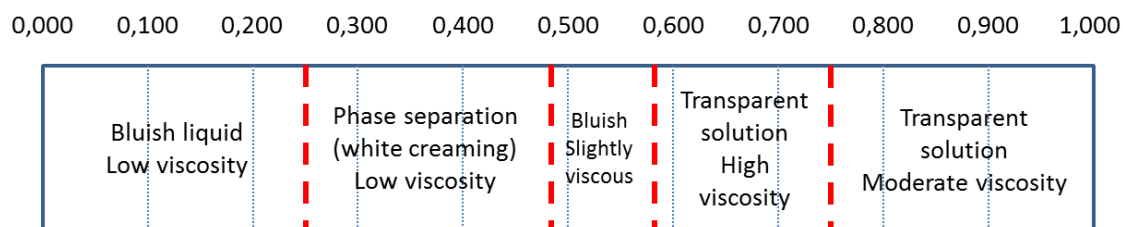


Figure 28 - Schematic representation of CTAB/SO₂So phase behavior for the different x_{CTAB}

3.1.2 Aggregate shape and size

The appearance of a bluish tinge in some samples suggests the presence of big scattering objects. To evaluate the structure of those aggregates, different cationic mixture ratios prepared were observed under a light microscope equipped with the DIC system (Figure 29). Aggregates were found only in the bluish samples in the form of either spherical vesicles or clusters of a large bilayer fragments. The samples appearing transparent to the naked eye, showed no evidence for aggregates under the resolution of the light microscope.

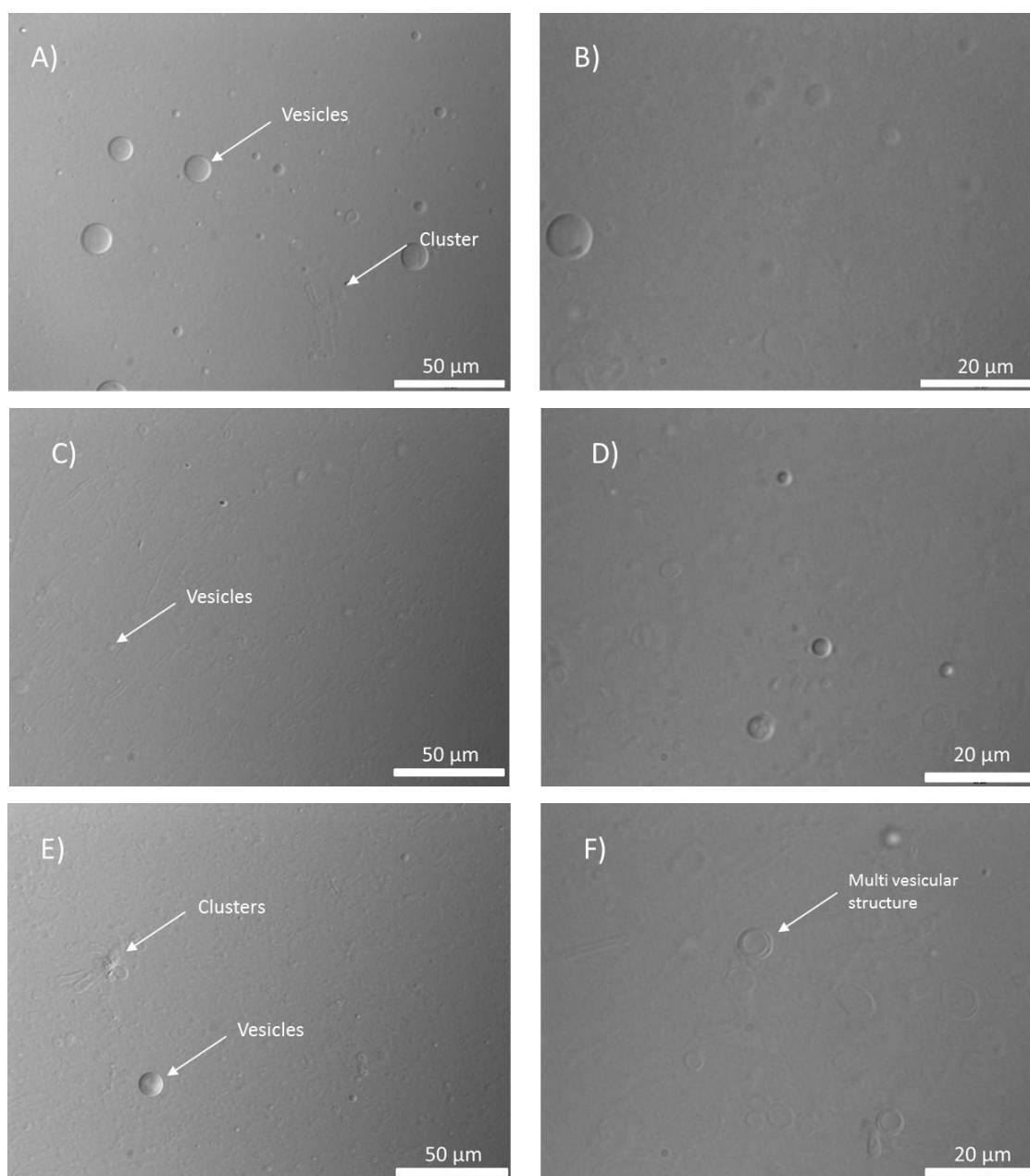


Figure 29 - Microscopic characterization of: A) 0.500 x_{CTAB} - 400x magnification, B) 0.500 x_{CTAB} - 1000x magnification; C) 0.200 x_{CTAB} - 400x magnification, D) 0.200 x_{CTAB} - 1000x magnification, E) 0.100 x_{CTAB} - 400x magnification, and F) 0.100 x_{CTAB} - 1000x magnification.

Vesicular micron-sized aggregates are observable for samples with $x_{CTAB} = 0.500$, 0.200 and 0.100 (Figure 29). The diameter of vesicles found in this analysis lies between 0.6 μm and 12 μm (giant unilamellar vesicles) indicating that the vesicles are highly polydisperse. It is worth mentioning that aggregates are present in two regions separated by a region of phase separation between 0.250 and 0.333. Birefringence of aggregate structures was probed with a cross-polarized system coupled with the microscope to evaluate the possible existence of multilamellar vesicles, but no evidence of this phenomena was found.

3.1.3 Aggregate distribution and zeta potential

In order to acquire further information about the phase behavior of the cationic mixture, aggregate size and apparent surface charge were probed for the different samples using dynamic light scattering and zeta potential. The collected data is presented for different cationic mixtures consisting in 5 independent measurements per sample.

From the obtained data some tendencies arise: aggregates from the cationic-rich side are smaller than the ones found in equimolar and anionic region. Mixtures with $x_{CTAB} = 0.900$, 0.800 and 0.750 display what is presumably small micelles that increase in size when more SOSo is present (with increasing diameter from 2 to 5 nm) (from Figure 30 to Figure 31).

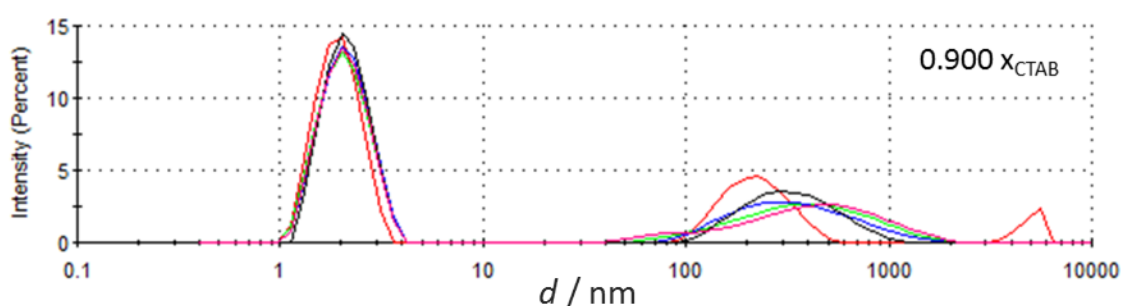


Figure 30 - Size distribution by intensity for 0.900 x_{CTAB} at $20 \text{ mmol} \cdot \text{kg}^{-1}$

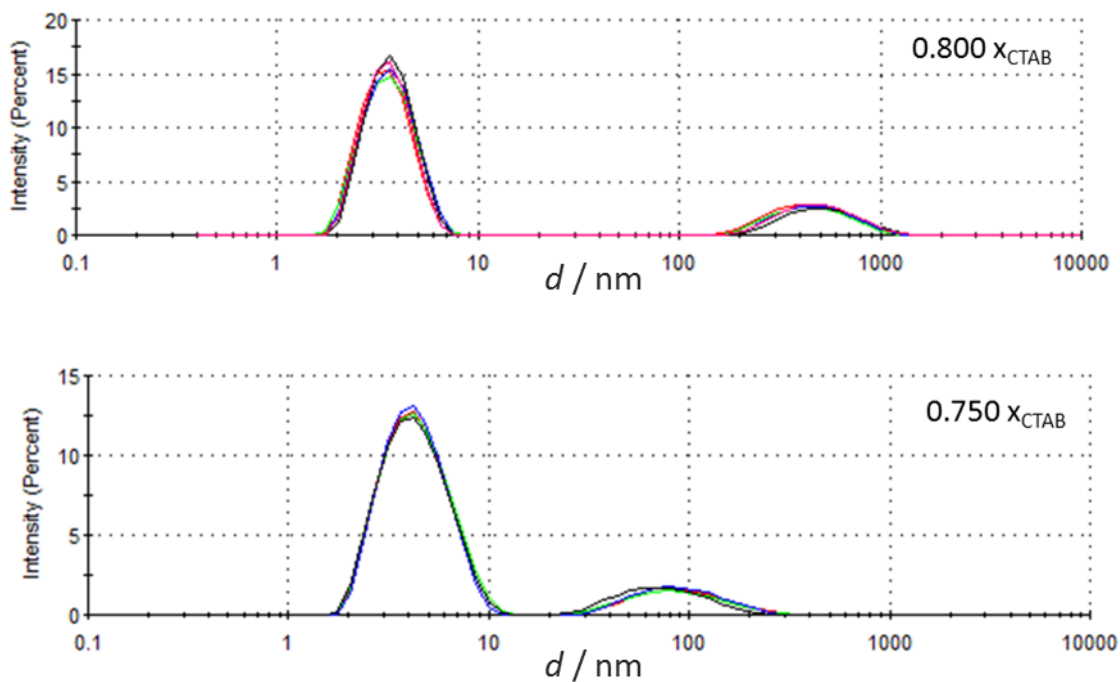


Figure 31 - Size distribution by intensity for 0.800 and 0.750 x_{CTAB} at 20 mmol·kg⁻¹

There is a bimodal distribution for these three different x_{CTAB} , with a very good agreement between the five measurements. The peak that appears on the left in the representations, deriving from smaller aggregates, is higher than the one on the right indicating that the amount of these bigger aggregates are negligible.

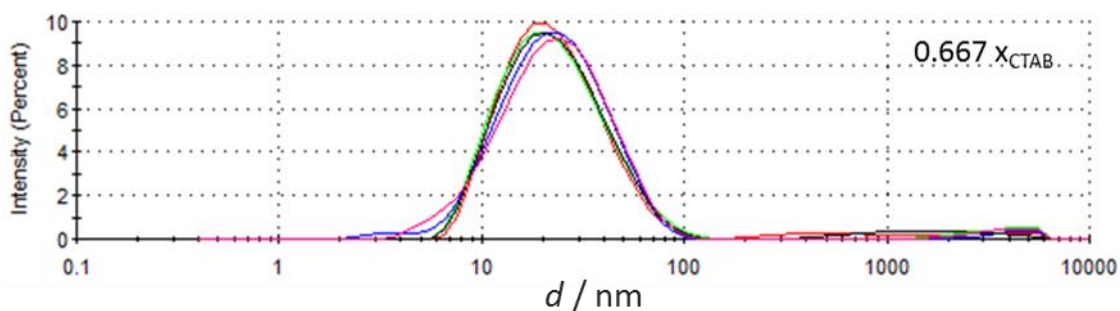


Figure 32 - Size distribution by intensity for 0.667 x_{CTAB} at 20 mmol·kg⁻¹

In sample $x_{CTAB} = 0.667$ (Figure 32) all 5 measurements converge to single peak for aggregates with a characteristic size of about 20 nm.

In Table 3, one can observe that the small aggregates (population 1) increase in size from 2.1 nm at sample 0.900 to 26.0 nm at sample 0.667. The relative abundance of this population increases with decreasing x_{CTAB} , from 66 to 97% between samples

0.900 and 0.667, respectively. Population 2 shows no trend in size distribution with x_{CTAB} variation, although the abundance of the second population increases with decreasing x_{CTAB} , from 34 to 3% between samples 0.900 and 0.667 respectively. The polydispersity index (PDI) for the different samples lies between 0.261 and 0.37 with no systematic variation with x_{CTAB} .

Table 3 - Summary table of of aggregate size distribution and respective frequency for samples 0.667, 0.750, 0.800 and 0.900 x_{CTAB}

x_{CTAB}	Population 1 / nm	Population 1 frequency / %	Population 2 / nm · 10 ²	Population 2 frequency / %	PDI
0.900	2.1 ± 0.1	66.3 ± 0.9	4.4 ± 0.6	33.7 ± 0.9	0.37 ± 0.01
0.800	3.7 ± 0.1	80.0 ± 0.9	5.1 ± 0.3	20.0 ± 0.9	0.269 ± 0.005
0.750	4.5 ± 0.1	85.3 ± 0.6	0.93 ± 0.08	14.8 ± 0.6	0.243 ± 0.003
0.667	26.0 ± 0.3	97 ± 1	34 ± 9	3 ± 1	0.261 ± 0.001

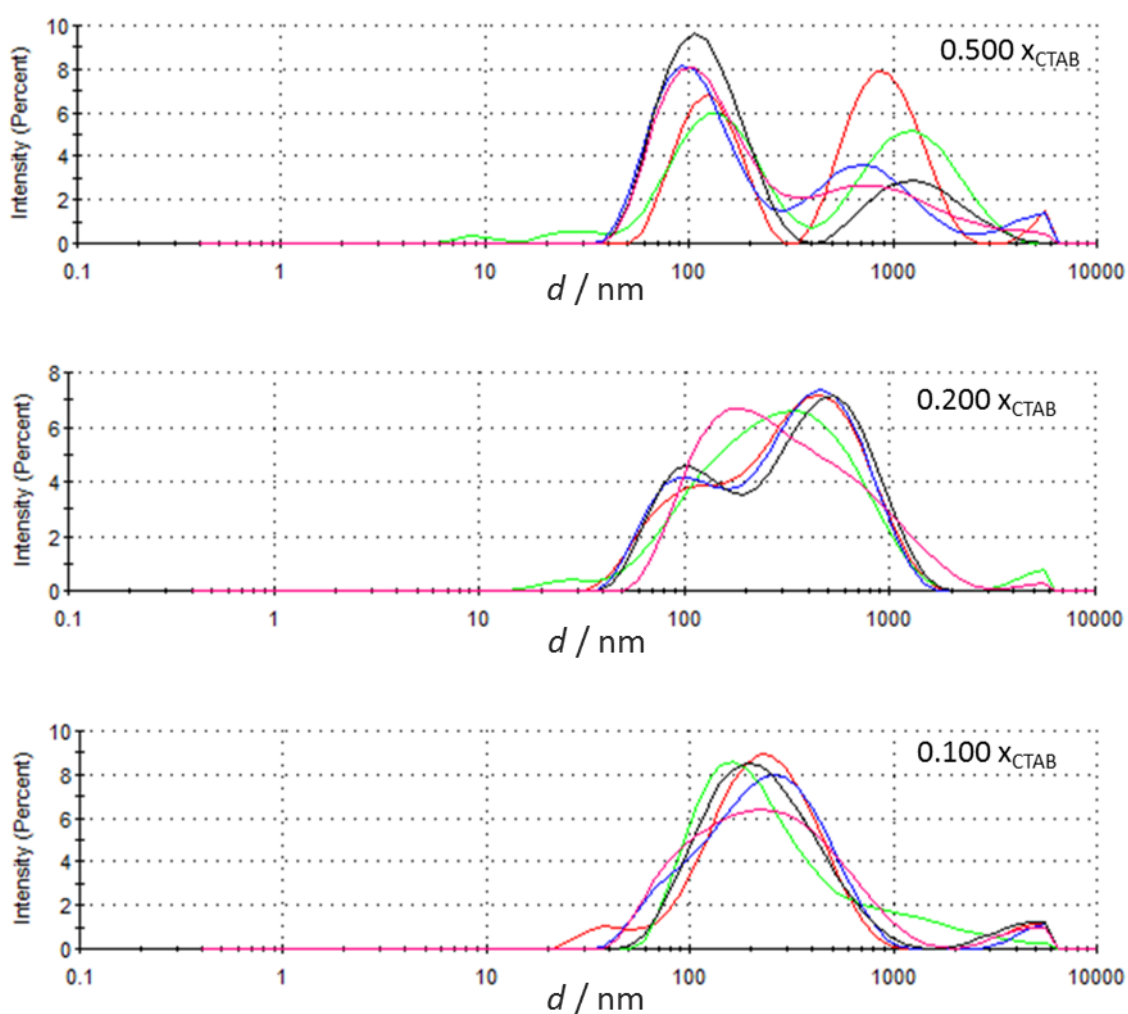


Figure 33 - Size distribution by intensity for 0.500, 0.200 and 0.100 x_{CTAB} at 20 mmol·kg⁻¹

In samples $x_{CTAB} = 0.500, 0.200$ and 0.100 (Figure 33) (where vesicles are observed), it is noticeable a higher polydispersity in the results and some discrepancy is found between measurements. Sample 0.100 presents a *PDI* of 0.42 , it increases for sample 0.200 as 0.47 , and sample 0.500 has the highest value with 0.59 . Aggregates appear to cover a range of sizes from tens of nanometers to several micrometers.

The Zeta potential study is presented considering 5 different measurements of each sample (Figure 34 and Figure 35). This technique indicates strong surface charge variation as shown in Table 4. The zeta potential has the most negative value for sample $0.100 x_{CTAB}$ with -18.9 mV and it decreases in absolute value as the x_{CTAB} increases until sample $0.333 x_{CTAB}$ where the zeta potential is near zero (-0.14 mV). At $0.500 x_{CTAB}$ a large positive value is reached (38 mV), which is rather high for equimolarity. For the cationic-rich region, it was not possible to measure the zeta potential.

Table 4 - Zeta potential as a function of the x_{CTAB}

x_{CTAB}	0.100	0.200	0.250	0.333	0.500	0.667	0.750	0.800	0.900
Zeta potential /mV	-19 ± 2	-9.5 ± 0.9	-6.4 ± 0.2	-0.1 ± 0.7	38 ± 2	n.m.	n.m.	n.m.	n.m.

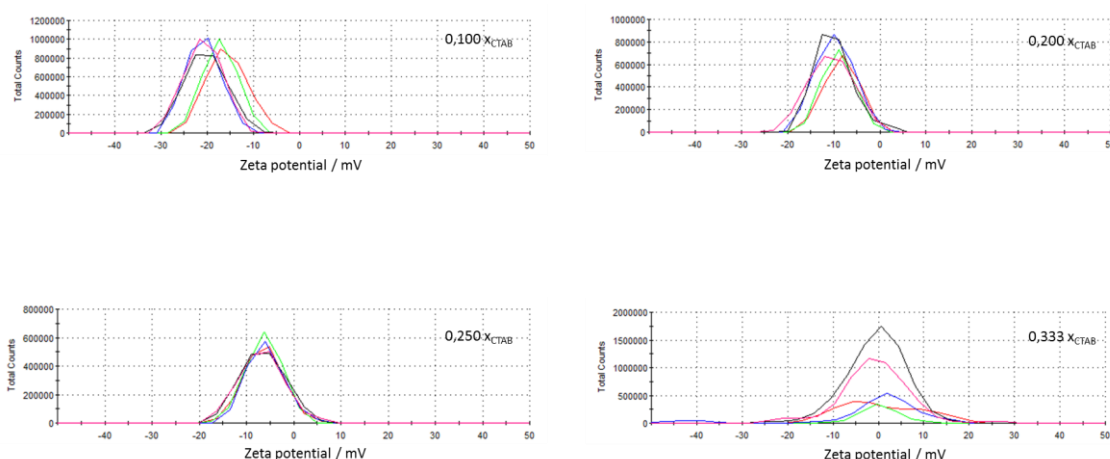


Figure 34 - Zeta potential distribution by intensity for $0.100, 0.200, 0.250, 0.333 x_{CTAB}$ at $20 \text{ mmol} \cdot \text{kg}^{-1}$

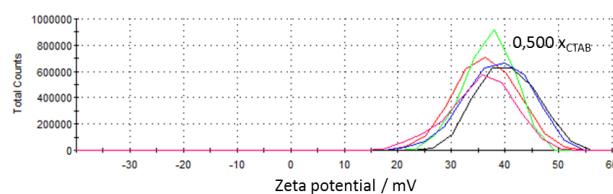


Figure 35 – Zeta potential distribution by intensity for $0.500 x_{CTAB}$ at $20 \text{ mmol}\cdot\text{kg}^{-1}$

3.1.4 Cmc determination by surface tension

Information about the critical micellar concentration (*cmc*) of the different surfactant mixtures was obtained by the evaluation of the cationic mixtures effect on the surface tension of the aqueous solutions (Figure 36). By plotting the surface tension of the solution as a function of the natural logarithm of the concentration, *cmc* can be calculated as described in section 2.4.1. The erratic behavior of surface tension for samples x_{CTAB} 0.200 and 0.100 may indicate the formation of different types of aggregates. Although it is unknown the nature of first aggregates that appear in solution, *cmc* is used for simplification.

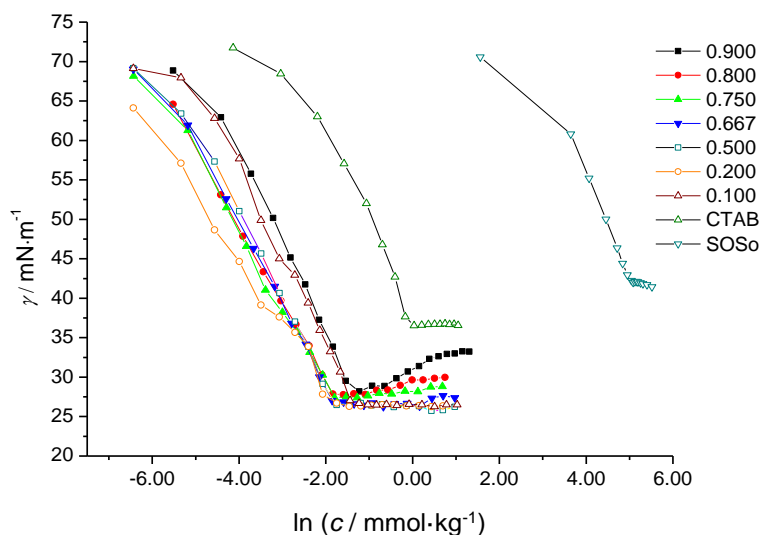


Figure 36 - Summary graph of surface tension as a function of the natural logarithm of concentration for different x_{CTAB}

The *cmc* values were calculated for the different samples and are listed in Table 5, along with the surface tension at *cmc* for the different mixtures.

Table 5 - *cmc* and surface tension on *cmc* for different x_{CTAB}

x_{CTAB}	<i>cmc</i> (mmol·kg ⁻¹)	γ_{cmc} (mN·m ⁻¹)
1.000	0.91 ± 0.04	36.7 ± 0.1
0.900	0.26 ± 0.02	28.2 ± 0.1
0.800	0.17 ± 0.02	27.7 ± 0.1
0.750	0.17 ± 0.02	27.3 ± 0.1
0.667	0.16 ± 0.02	26.8 ± 0.1
0.500	0.16 ± 0.03	26.4 ± 0.1
0.333	-	-
0.250	-	-
0.200	0.14 ± 0.02	26.3 ± 0.1
0.100	0.24 ± 0.04	26.5 ± 0.1
0.000	153 ± 1	42.1 ± 0.1

Clear differences are observed in surface tension behavior for the different samples both before and after the *cmc* (Figure 36). From 0.91 mmol·kg⁻¹ at $x_{CTAB} = 1.000$ to 0.14 mmol·kg⁻¹ at 0.200, the *cmc* value decreases reaching a minimum. Then, it increases again until 153 mmol·kg⁻¹ at 0.000 (neat SOSo). Surface tension on *cmc* follows the same tendency from: 36.7 mN·m⁻¹ at 1.000, it decreases to 26.3 mN·m⁻¹ at 0.200 and then increases again to 42.1 mN·m⁻¹ at 0.000 (Figure 37). Sample 0.333 and 0.250 were not measured due to the presence of phase separation (creaming).

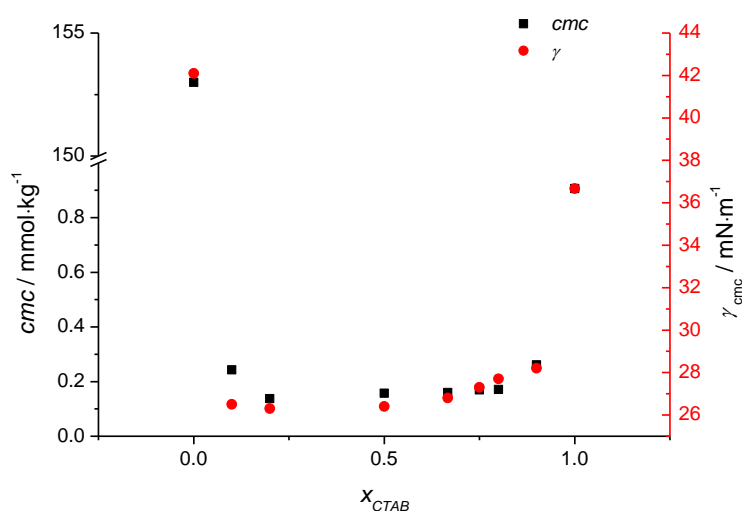


Figure 37 – Summary graph of *cmc* and γ_{cmc} as a function of x_{CTAB}

Except for samples with $x_{CTAB} = 0.900, 0.200$ and 0.100 , before cmc , the surface tension decreases by the same magnitude as the natural logarithm of the concentration increases. Sample 0.900 and 0.100 have higher surface tension than the other samples for the same concentrations although sample 0.100 has a more erratic lowering. Sample 0.200 has also an erratic lowering, but the surface tension is lower than any other sample. After the cmc , the surface tension starts to increase again, with increasing intensity, from 0.670 to 0.900 . For the other samples, the surface tension after cmc is constant.

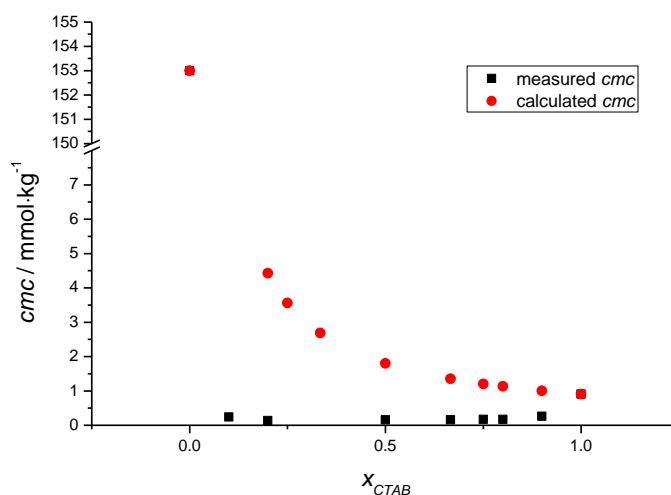


Figure 38 - Measured and calculated cmc for different x_{CTAB}

Figure 38 presents the difference between the cmc measured for the different x_{CTAB} and the theoretical value obtained for an ideal surfactant mixture as referred in section 1.2.3. It is possible to observe that for all the x_{CTAB} range, the theoretical value is higher than the measured one. As an example, for sample 0.900 the ideal value is five times bigger. For sample 0.100 the difference is more than thirty five times. This difference in these values indicates synergistic behavior between the surfactants. In Table 6 the β parameter is calculated to evaluate the degree of synergism for each x_{CTAB} . β values lie between -13.9 for sample 0.900 and -18.1 for sample 0.200 . The synergism is highest for sample in the anionic rich region. An average value $\beta = 16 \pm 1$ was found for the mixture.

Table 6 - Interaction parameter β as a function of x_{CTAB}

x_{CTAB}	0.100	0.200	0.500	0.667	0.750	0.800	0.900
β	-17.7	-18.1	-15.8	-15.5	-15.3	-15.4	-13.9

3.1.5 Viscosity profile by solution rheometry

Rheological studies concerning solution viscosity were carried out for samples with x_{CTAB} ranging from 0.480 to 0.800. Previous results indicate that different types of self-assembled structures are present for different mixing ratios of these catanionic mixtures. Solution viscosity can add some more information about aggregation behavior of the samples.

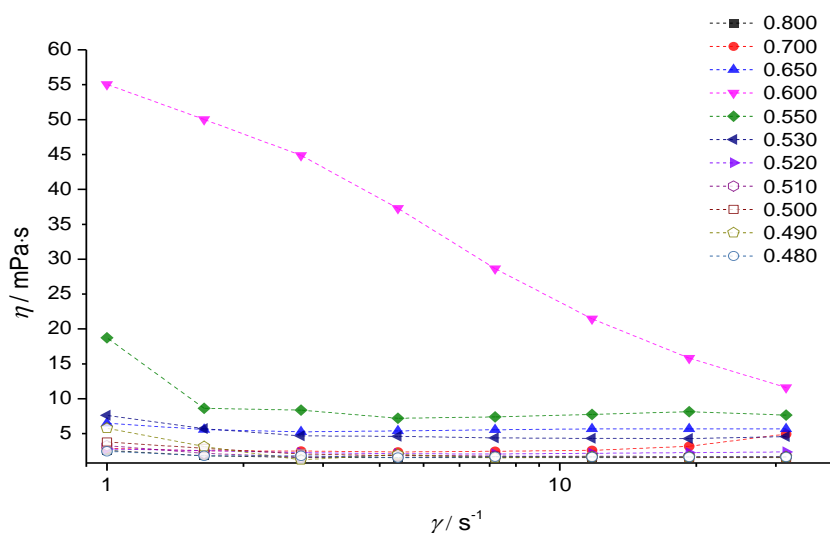


Figure 39 – Viscosity as a function of shear rate for different x_{CTAB}

The viscosity of different CTAB/SOSo mixtures as a function of the shear rate was probed using a double gap measuring system. The shear rate was increased in a log ramp sweep from 1 to 30 s^{-1} acquiring 8 points in each sample to obtain the presented curves (Figure 39).

It is possible to see that viscosity increases from $x_{CTAB} = 0.800$ up to 0.600, where the viscosity at the lower shear rate is around 55 mPa·s. From 0.600 to 0.510, the viscosity decreases and below sample 0.510 the viscosity is approximately constant for the samples. Samples with the lowest viscosity (between 1.4 and 1.8 mPa·s) have slightly higher viscosity than water (1.0 mPa·s). Especially for sample 0.600, it is clear that a shear-thinning behavior occurs, since the viscosity drops as the shear rate is increased. The high viscosity and shear thinning behavior of this sample suggest the presence of elongated micelles that align or break as the shear rate increases ^[57].

Sample 0.550 x_{CTAB} presents phase separation into two distinct liquids, a bluish top phase and a transparent bottom one. While phase separated the sample was analyzed under cross polarized light to investigate the occurrence of birefringent structures, such as lamellar phases, but no evidence of it was found.

3.1.6 Cryo-TEM observations

More detailed information about the aggregation behavior of sample 0.530 x_{CTAB} analysis was obtained by Cryo-TEM (Figure 40). The sample is bluish at naked eye and viscosity tests indicate a viscosity about ten times the viscosity of water. The initial sample was divided in two parts: one part was analyzed directly, the other part was foamed and the drained liquid was analyzed one minute afterwards.

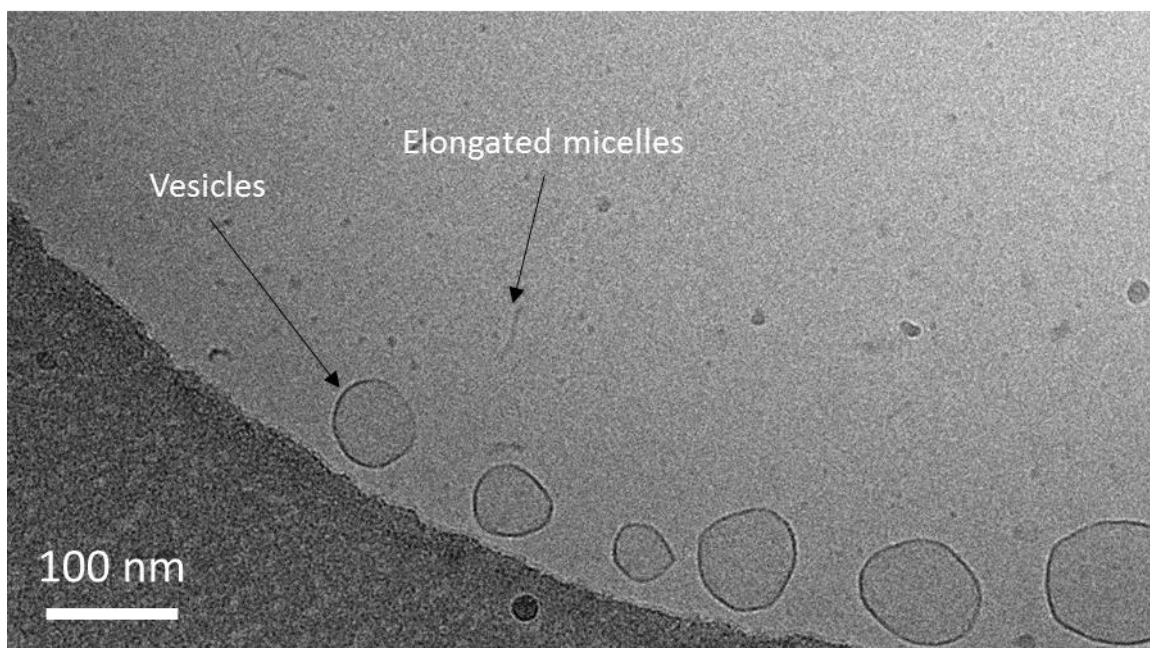
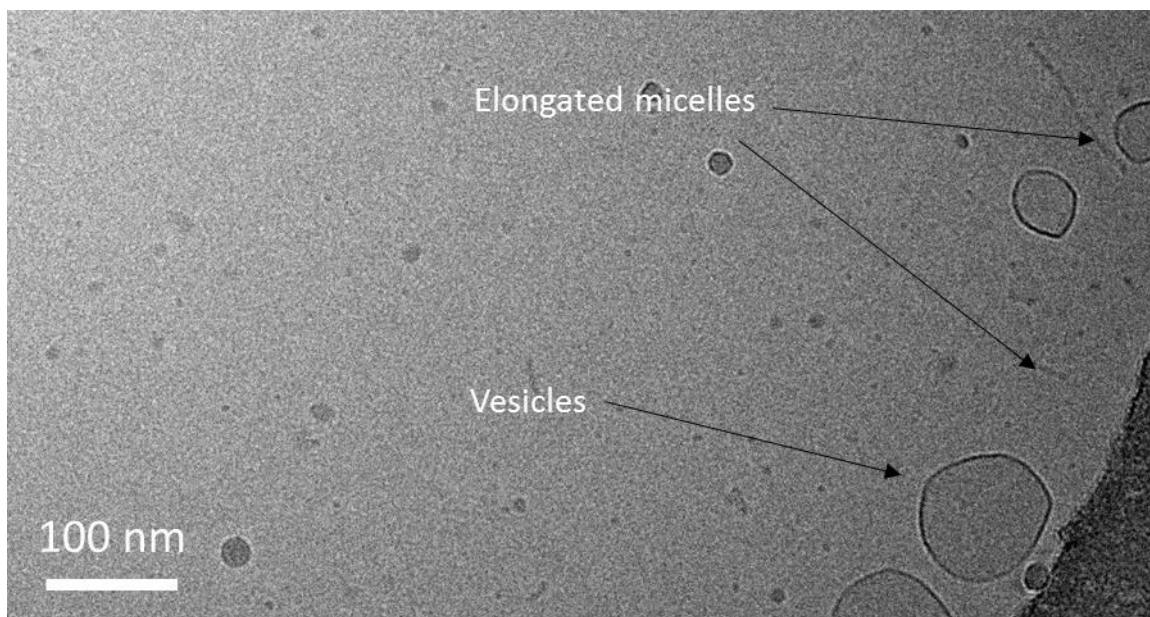


Figure 40 - Cryo-TEM images of sample 0.530 x_{CTAB} at 20 mmol·kg⁻¹ showing vesicles and elongated micelles.

The inspection of the sample provided the confirmation of the existence of vesicles and elongated micelles for this x_{CTAB} . The radius of the vesicles, measured in these samples, lies between 40 and 150 nm, although these values may be biased since big aggregates are usually eliminated due to the size of the film [58]. There was no discernible difference between the undisturbed samples, and the samples after the foaming process.

3.1.7 Small Angle Neutron Scattering (SANS) study

The scattering intensity as a function of the wave vector was probed with 3 or 4 different configurations depending on the sample under study. As previously explained in chapter 2, the wave vector (q) is the difference between the scattered and the incident wave vectors. Settings that probe very low q ($0.002 - 0.02 \text{ \AA}^{-1}$) and low q ($0.005 - 0.05 \text{ \AA}^{-1}$) allow the observation of the scattering object at a big scale. At middle q ($0.03 - 0.13 \text{ \AA}^{-1}$) information about the shape of the particle is dominant and high q ($0.07 - 0.4 \text{ \AA}^{-1}$) gives information about the cross section of the structures. The different scattering spectra for a certain sample are merged resorting to *Pasinet v2.0146* and fitted with *SasView v3.1.2* software's with the purpose of finding the shape and characteristic size of the particle.

SANS results brought significant insight on the studied system. In a sweep over the different extremes of x_{CTAB} , three main different types of aggregation were found. For $x_{CTAB} = 0.900$ to 0.800 , the fitted data was in agreement with the presence of spherical or ellipsoid micelles in solution. As the molar ratio decreases, one can find a transition from spherical micelles to rod like micelles at 0.750 . From 0.700 to 0.590 , in a first approach, the data was fitted for worm-like micelles with a good fitting that returns a persistence length higher than the total length of the aggregate. This means that the aggregates are in fact rigid rods and not worm-like micelles, thus, the curves were fitted for rod-like micelles, since it is simpler to compute improving the accuracy of the results. From samples 0.510 to 0.100 , the scattering profiles are consistent with vesicles in solution. From Figure 41 to Figure 43, we show representative plots of the different types of aggregates for which the data was fitted.

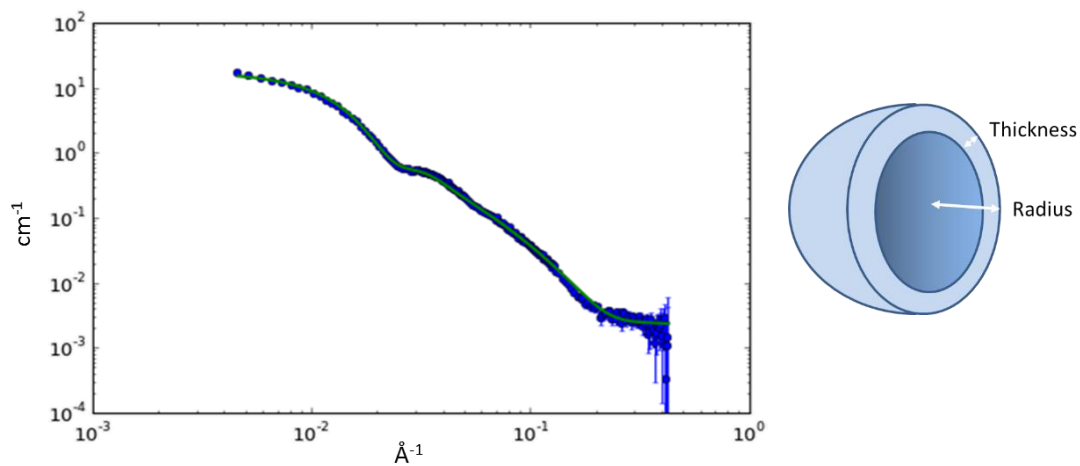


Figure 41 – Model example (sample 0.100) of the scattering intensity as a function of the wave vector for vesicles in solution on the left and schematic representation of a vesicle and respective characteristic sizes on the right.

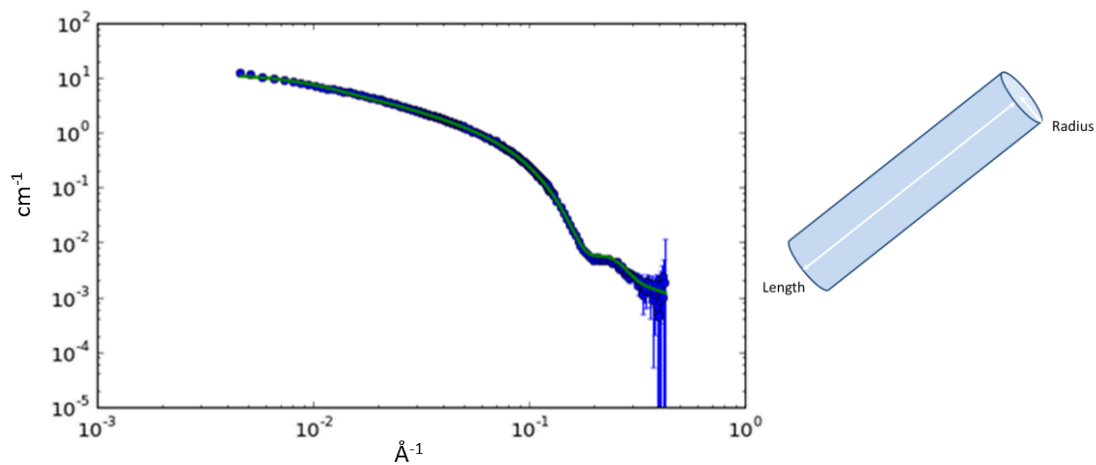


Figure 42 - Model example (sample 0.590) of the scattering intensity as a function of the wave vector for rods in solution on the left and schematic representation of a rod and respective characteristic sizes on the right.

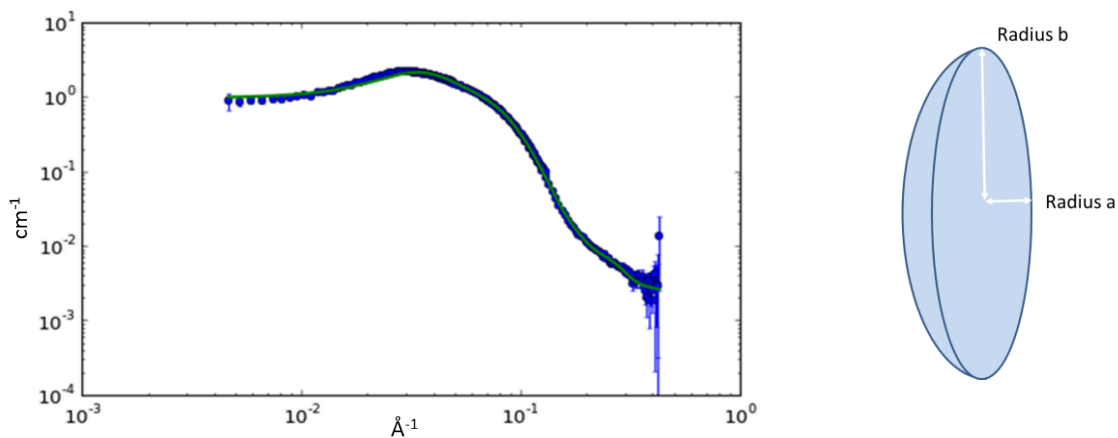


Figure 43 - Model example (sample 0.800) of the scattering intensity as a function of the wave vector for ellipsoids in solution on the left and schematic representation of an ellipsoid and respective characteristic sizes on the right.

The differences between the aggregates arise from their different size and shape. For the different types of aggregates, the characteristic length scales influence the profile of the SANS curve.

Figure 44 presents the acquired data for all the bulk samples studied by neutron scattering. These samples are prepared in D_2O to enhance the contrast between the scattering objects and the solvent, so that they can be observed in SANS. Although we assume that no big differences are present, the use of D_2O instead of H_2O may lead to small changes in the phase behavior of the surfactant mixture. To simplify the analysis, samples were divided. In the top plot we represent all the x_{CTAB} whose fitting processes involved vesicular shape, and in the bottom plot we present all the other samples.

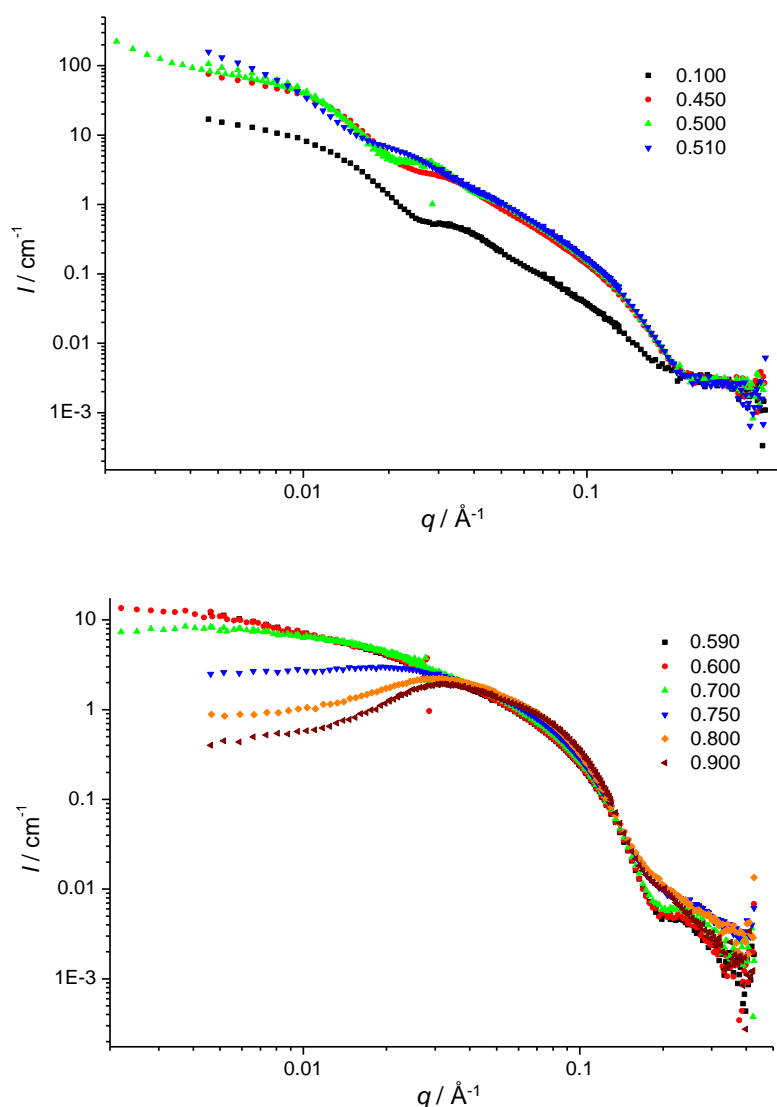


Figure 44 - Intensity as a function of q for the different samples analyzed

The fitting parameters obtained for each sample are summarized from Table 7 to Table 9 and divided by shapes (vesicles, rods and ellipsoids respectively).

Table 7 - Summary table of fitting parameters for samples 0.100, 0.450, 0.500 and 0.510 x_{CTAB} using form factor for vesicle shape.

Molar ratio	0.100	0.450	0.500	0.510
Radius / nm	9.0 ± 0.1	10.4 ± 0.1	11.6 ± 0.1	12.6 ± 0.2
Radius polydispersity	0.383 ± 0.005	0.333 ± 0.002	0.353 ± 0.003	0.60 ± 0.01
Thickness / nm	2.2 ± 0.1	2.6 ± 0.1	2.6 ± 0.1	2.6 ± 0.1
Thickness polydispersity	0.1 ± 0.5	0.077 ± 0.007	-	-
Scaling factor · 10³	1.015 ± 0.007	3.606 ± 0.006	3.92 ± 0.006	4.229 ± 0.006
Background · 10³	2.016	2.348	2.337	1.387
Aggregate sld · 10⁶	0.23	-0.37	-0.075	-0.083
Solvent sld · 10⁶	6.39	6.39	6.39	6.39

Vesicular structures are found both in the equimolar and anionic regions of x_{CTAB} . Although these two regions present self-assembled vesicles, there are some differences between them, evidenced in Table 7. As x_{CTAB} increases, the average radius of the vesicles increases. The bilayer thickness is the same for $x_{CTAB} = 0.510, 0.500$ and 0.450 (2.6 nm) but it is thinner for 0.100 (2.2 nm). Polydispersity of the vesicles is very similar for samples $0.500, 0.450$ and 0.100 (around 0.350) and is almost the double for sample 0.510 . In addition the scaling factor decreases significantly from sample 0.510 to 0.100 .

Table 8 - Summary table of fitting parameters for samples 0.590, 0.600, 0.700 and 0.750 x_{CTAB} using form factor for rod shape.

Molar ratio	0.590	0.600	0.700	0.750
Length / nm	44.2 ± 0.8	40.5 ± 0.9	27.0 ± 0.2	9.24 ± 0.04
Length polydispersity	-	0.4 ± 0.1	0.11 ± 0.04	0.24 ± 0.01
Radius / nm	2.0 ± 0.1	2.0 ± 0.1	2.0 ± 0.1	2.1 ± 0.1
Radius polydispersity	0.145 ± 0.003	0.147 ± 0.003	0.148 ± 0.001	0.128 ± 0.001
Scaling factor · 10³	4.483 ± 0.007	4.54 ± 0.007	4.81 ± 0.006	4.984 ± 0.006
background · 10³	0.884	0.917	1.18	2.50
Aggregate sld · 10⁶	-0.144	-0.152	-0.228	-0.305
Solvent sld · 10⁶	6.39	6.39	6.39	6.39

From sample 0.510 to 0.590 , one observes a transition in the scattering pattern indicating different types of aggregates. In the cationic-rich region between 0.590 and 0.750 , the data is fitted with a form factor of rod like structures. As x_{CTAB} increases, the

length of the rods decreases from 44.2 nm for sample 0.600 to 9.24 nm for sample 0.750. The cross-section radius of the rods is approximately the same (≈ 2 nm) with a slight difference for sample 0.750, which lies between two scattering regimes, although it can be fitted for rod-like structures. Radius polydispersity is almost the same for the different sample (≈ 0.14) whereas length polydispersity depends on the samples varying between 0.11 in sample 0.700 to 0.4 in sample 0.600. The scaling factor increases with increasing X_{CTAB} .

Table 9 - Summary table of fitting parameters for samples 0.100, 0.450, 0.500 and 0.510 X_{CTAB} using form factor for spherical shape.

Molar ratio	0.800	0.900
Radius a / nm	2.0 ± 0.1	2.0 ± 0.1
Radius a polydispersity	-	-
Radius b / nm	3.4 ± 0.1	3.2 ± 0.1
Radius b polydispersity	0.204 ± 0.001	0.04 ± 0.008
Scaling factor $\cdot 10^3$	5.11 ± 0.03	5.16 ± 0.01
Background $\cdot 10^3$	2.016	2.348
Aggregate sld $\cdot 10^6$	-0.300	-0.381
Solvent sld $\cdot 10^6$	6.39	6.39

Samples 0.800 and 0.900 X_{CTAB} present yet another intensity pattern that indicates the presence of ellipsoid or spherical structures.

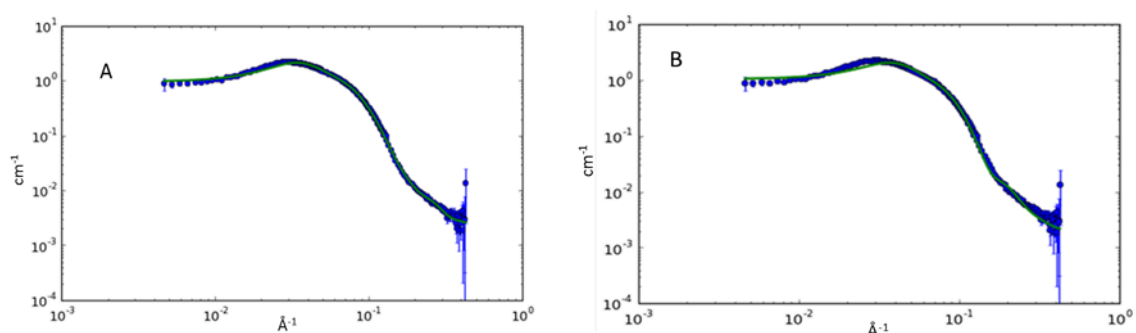


Figure 45 - Comparison of the fitting of 0.800 X_{CTAB} data for A) ellipsoid form factor, and B) sphere form factor

Both form factors were tested for the fitting process and both present good data fitting (Figure 45). The ellipsoid model was chosen instead of the spherical one because the fitting value for the sphere radius was higher than a fully stretched CTAB molecule, hence this value had no physical meaning. $X_{CTAB} = 0.800$ and 0.900 present similar characteristic values. Radius a is the same for samples 0.800 and 0.900 (2.0 nm), but radius b is slightly higher for sample 0.800. Polydispersity of radius b for sample 0.800

(0.204) is higher than the one for sample 0.900 (0.04). The scaling factor decreases slightly from sample 0.900 to 0.800.

The scaling factor is a parameter derived from the fitting process that condenses information on the number of particles and the volume of a single particle. This parameter is related with the volume fraction of the aggregates. As expected, since CTAB is a larger molecule than SOSo, the volume fraction increases with increasing x_{CTAB} (Figure 46).

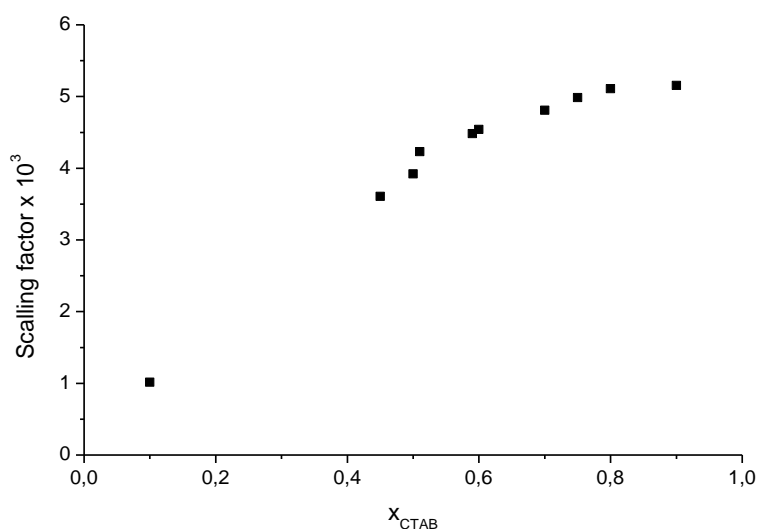


Figure 46 - Scaling factor as a function of the x_{CTAB}

3.1.8 Discussion – Bulk behavior

With the information obtained from the different techniques for the 20 mmol·kg⁻¹ CTAB/SOSo cationic mixture, an overview of the system can be done regarding its phase behavior and self-assembling properties. To simplify the analysis, we start from CTAB micelles x_{CTAB} and we evaluate the effect of adding SOSo in the aggregate structures (decreasing CTAB).

From the macroscopic observation, it was already clear that a variation in x_{CTAB} influences the aggregation behavior of the solutions. The transparent cationic-rich side was found to contain small ellipsoidal micelles that grow into rod-like micelles as x_{CTAB} decreases from $x_{CTAB} = 1.000$ to 0.590. This growth tendency is consistent with an increasing viscosity in the samples indicating that the rod structure of the aggregates

may be responsible for this behavior. For sample 0.530, vesicles form in coexistence with rod-like micelles, as observed in Cryo-TEM. From 0.530 to 0.500, the decrease in viscosity suggests a gradual disappearing of rods leaving a single vesicle solution with unusually high zeta potential (37.6 mV) for equimolarity. With further decrease in x_{CTAB} , although sample 0.450 still presents vesicles, phase separation occurs from sample 0.333 to 0.250 where zeta potential is near zero. At $x_{CTAB0} = 0.200$ and 0.100 vesicles are found again, this time with negative surface charge in line with the higher proportion of SOSo in the system.

The bilayer thickness is higher for vesicles from the equimolar region than for vesicles from the anionic rich region. Given that the surface charge is different, being positive for vesicles in the equimolar region, it is a possibility that the bilayer has different composition: rich in CTAB for 0.500 x_{CTAB} and rich in SOSo for 0.100 x_{CTAB} , suggesting two different types of vesicles for the same catanionic system. Microscopy, DLS and SANS measurements in combination suggest that both vesicular structures are widely polydisperse with diameters ranging from tens of nanometers to few micrometers.

Considering that the total concentration of surfactant is the same, decreasing x_{CTAB} implies the substitution of CTAB for SOSo molecules. Hence, the decrease in aggregate volume fraction should in principle follow a linear tendency. In Figure 46, we observe a non-linear decrease of the scaling factor with decreasing x_{CTAB} , suggesting that as x_{CTAB} decreases, some of the molecules are left outside the aggregates.

Altogether, the dependence of phase behavior with x_{CTAB} , cmc determinations and β parameter show a strong synergism between the two surfactants. The appearance of ellipsoids at first, then rods and finally vesicles as x_{CTAB} decreases from 1.000 to 0.500 indicates that the interaction between CTAB and SOSo increases successively the effective packing parameter or, alternatively, decreases the mean spontaneous curvature of the aggregates in this range. This defined trend is not observed between 0.500 and 0.000 although the presence of vesicular structures and precipitate clearly indicates the strong interaction between aggregates and increase in the effective packing parameter compared with the single surfactants.

For a visual understanding of the aggregation behavior in the bulk solutions Figure 47 displays a schematic representation of self-assembled structures as a function of the x_{CTAB} . Neat surfactants are not represented in the diagram for pure SOSo did not form micelles at this concentration and neat CTAB could not be analyzed.

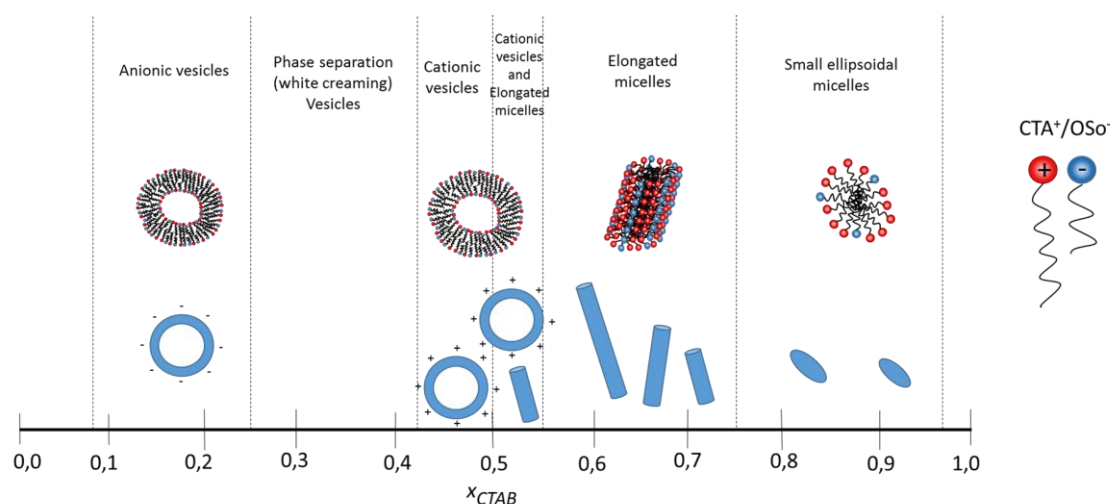


Figure 47 - Schematic representation of the types of aggregates formed as a function of X_{CTAB}

Molecular view

The mixture of CTAB and SOSo presents strong synergistic behavior. Reduction in both *cmc* and surface tension at *cmc* can be explained by the strong electrostatic interaction between the head groups. Contact between these opposite charges gives rise to a screening effect lowering the repulsion between head groups and allowing a denser packing at the surfaces. This interaction allows a decrease in surface tension compared with the single surfactants. Interaction between head groups also allow the freeing of the counter ions leading to an increase in entropy of the system, favoring mixed aggregation and explaining the lowering in *cmc*.

Given that the hydrophobic chain of SOSo is smaller than the CTAB one, as X_{CTAB} decrease one could expect that the effective packing parameter of the aggregates would decrease as well. But, as mentioned above, the electrostatic attraction between head groups lead to a screening effect on the charges decreasing the surface area and thus increasing the packing parameter of the mixture. The sequence of the aggregates formed when decreasing X_{CTAB} , indicates that the effective packing parameter of the mixture is increasing. Possibly the differences in aggregation derive from both the difference in chain length and electrostatic interaction, although, from the results, we can observe that the dominant factor is the last one.

The difference in chain length is also responsible for a mismatched solubility between the two surfactants. The presence of positively charged vesicles in the equimolar region may be understood by the higher solubility of SOSo leaving the

aggregates richer in CTAB. The formation of vesicular structures in two regions, with different compositions, can be explained by the coexistence of surfactants with different chain length. The organization of the surfactants in a bilayer is not limited by one characteristic surfactant chain length. The arrangement between different amounts of surfactants in the inner or outer layers allow the formation of vesicular structures for different compositions.

The non-linear dependence of the volume fraction of aggregates in solution with x_{CTAB} can be explained by the fact that the *cmc* of neat SOSo is more than a hundred times lower than the concentration we are dealing with these experiments. In the presence of CTAB, the electrostatic interaction between the surfactants is strong enough to keep SOSo in the aggregates. As x_{CTAB} decreases, less and less CTAB molecules are available to keep the SOSo in the aggregates. When all the CTAB is occupied, SOSo starts to solubilize.

The Increase in viscosity is related with the presence of rod-like micelles in solution. The physical interactions among the elongated aggregates create transient entanglements that turn the flow of the liquid more difficult.

Comparison with previous results

Due to their remarkable properties, catanionic mixtures and catanionic surfactants have been widely studied regarding bulk and interfacial behavior. Catanionic mixtures present a rich phase behavior comprising a wide range of microstructures at various mixing ratios as can be seen in the present work.

The surface behavior of catanionic mixture CTAB/SOSo was previously studied in our group ^[59]. For this catanionic system, the dependence of surface tension with concentration was investigated with similar results to those obtained in this work. Both studies show that the *cmc* of the surfactant mixtures is lower than the *cmc* for the individual surfactants with very good agreement between the values except for the ratio $x_{CTAB} = 0.500$. For this sample, the *cmc* value in the previous work was close to that in the catanionic surfactant TAso (surfactant counter-ion free derived from the equimolar mixture of the individual surfactants used in this work). This value is two times lower than the one we found in this work. The synergistic behavior was presented by the interaction parameter, β , that present a similar average value (-16) in both studies.

In order to obtain further insight about the aggregation behavior in catanionic mixtures, various systems are compared in table 10 considering differences in chain length, for both anionic and cationic surfactants.

Table 10 – Aggregation behavior for different catanionic mixtures. *M* = micelles, *sM* = spherical micelles, *eM* = ellipsoidal micelles, *R* = rod-like micelles, *V* = vesicles, *L* = lamellar phase, *L.C.* = liquid crystalline phase, *P* = precipitate, *C.L.* = clear liquid, *MPh* = multi-phase region, *I* = isotropic phase, *2Ph* = two phase region. ^{+/−} indicates cationic-rich or anionic-rich respectively. *x_c* indicates molar fraction of cationic surfactant.

Surfactant mixture	Alkyl chain length difference	Aggregate evolution with <i>x_c</i>	Reference
CTAB/SOSo	16-8	$V^- \rightarrow V^- + P \rightarrow V^+ \rightarrow V^+ + R \rightarrow R \rightarrow eM$	This work
CTAB/SOS	16-8	$sM \rightarrow V^- \rightarrow V^- + L \rightarrow V^+ \rightarrow V^+ + R \rightarrow R$	Brasher 1995 Karukstis 2004
CTAB/SDSO	16-12	$I \rightarrow 2Ph \rightarrow L.C. \rightarrow P \rightarrow L.C. \rightarrow 2Ph \rightarrow I \rightarrow 2Ph \rightarrow L.C.$	Nan 2005 You 2009
CTAB/SDS	16-12	$I \rightarrow L.C. \rightarrow P \rightarrow L.C \rightarrow I$	Zhang 2008
DTAB/SDS	12-12	$M \rightarrow MPh \rightarrow V + P \rightarrow C.L. + P \rightarrow M$	Chen 1973 Herrington 1993
OTAB/SDS	8-12	$I \rightarrow L.C. \rightarrow 2Ph \rightarrow I$	Chen 1973

As can be observed in the comparative table, there are differences in the aggregation behavior sequence when different surfactants of opposite charge are mixed in a water-rich environment. The comparison between different studies is not always easy and robust due to the different levels of detail of the studies available, which can give rise to ambiguous or insufficient information for comparisons. Nonetheless, there seem to be obvious differences in phase behavior between some systems that allow for some general conclusions.

The similarities between our system and CTAB/SOS^[60, 61] are obvious. The latter mixture, which only differs in the anionic head group, presents considerable resemblance in aggregation behavior sequence to the one studied here. There are however some differences like the presence of a lamellar phase near the equimolar region, that is not present in CTAB/SOSo system, the presence of rod-like micelles in the cationic-rich region that appear as ellipsoidal micelles in our system, and the presence of anionic spherical micelles that were not observed in our study. Both the study conducted by *Brasher* and coworkers and the one conducted by *Karukstis* and coworkers are in good agreement.

As the chain length asymmetry become smaller, more pronounced differences are found for the aggregation behavior in comparison with CTAB/SOSo. CTAB/SDSo^[62, 63] or CTAB/SDS^[64] present a more symmetrical behavior for the cationic and anionic-rich sides with presence of liquid crystalline phases that are not observed in CTAB/SOSo. In these systems a significant part of the diagram is dominated by precipitate around the equimolar region. It is noteworthy that the spontaneous formation of vesicles was not observed for these systems. The studies conducted by *Nan* and coworkers and *You* and coworkers present very similar results with latter one complementing the aggregation behavior on the cationic rich side with a two-phase and a liquid crystalline phase region.

In the symmetric system DTAB/SDS^[18, 65], the differences become even more pronounced since precipitation occurs mainly in the cationic rich region whereas in the other systems it is mostly observed in the anionic-rich one. In this system, no liquid crystals are formed and a precipitate dominates the phase diagram. The study of *Herrington* and coworkers presents good agreement with the one conducted by *Chen* and coworkers but with a much higher level of detail.

The study of the asymmetric system OTAB/SDS^[65] shows the presence of a liquid crystalline phase that is not present in the CTAB/SOSo system. Although detailed information is scarce for this mixture, the study reveals clear differences in phase behavior when compared with our system.

Variation in the asymmetry of the hydrophobic chain length between the two surfactants is a key parameter for the aggregation behavior of catanionic systems. In a general way, as the symmetry increases also does the precipitation area in the phase diagram. Differences in the asymmetry of the chain length dictates the formation of different types of self-assembled structures and different transitions between aggregates. It appears that the difference between sulfate and sulfonate in the head group cause small differences in the aggregation behavior, although these differences can also result from other factors.

3.2 Foams

To study the ageing process of the different foams produced with the different x_{CTAB} solutions, experiments concerning the foam stability were conducted.

It is possible to have an idea about foamability observing how the samples produce foam by vigorous shaking. Both foaming and foam stability are different between the cationic and anionic-rich sides. In the anionic-rich side, it is not possible to produce foam whereas in the cationic rich side it is very easy except for $x_{CTAB} = 0.670$ where low foamability is found, probably due to the viscosity of the solution. Sample 0.500 foams well despite being at midpoint between the anionic and cationic-rich sides. It can also be observed that the rate at which the liquid drains to the bottom of the container is different for the different samples.

3.2.1 Foam ageing

Drainage velocity is measured for different foams, generated with pure air as the dispersed phase, at 20% ϕ , as a function of x_{CTAB} . The plot in Figure 48 was constructed to evaluate the behavior of foam drainage for the different samples.

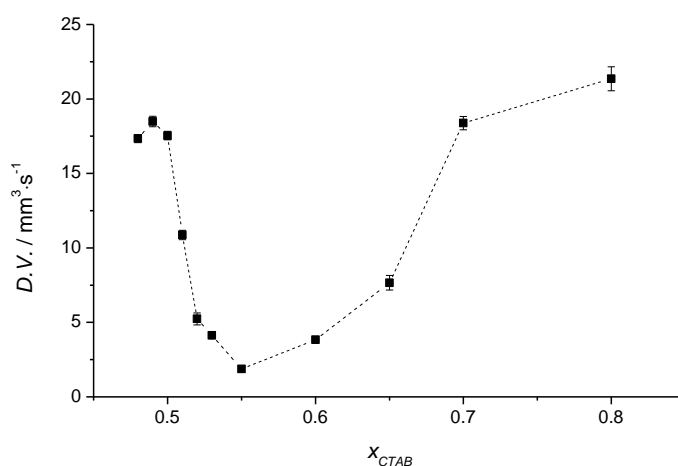


Figure 48 - Drainage velocity of foams, at 20% liquid fraction generated with simple air, as a function of the x_{CTAB} .

$x_{CTAB} = 0.480, 0.490$ and 0.500 have similar drainage velocities comprised between 17.3 and $18.4 \text{ mm}^3 \cdot \text{s}^{-1}$. As the x_{CTAB} increases, the drainage velocity decreases sharply reaching a minimum of $1.88 \text{ mm}^3 \cdot \text{s}^{-1}$ at 0.550 . From 0.550 to 0.800 the drainage

velocity increases reaching the highest value of $21.3 \text{ mm}^3 \cdot \text{s}^{-1}$. The minimum in drainage velocity appears in a region of transition between rod-like micelles and vesicles.

Drainage velocity of foams generated with air containing traces of C_6F_{14} , at 20% ϕ , was measured for different x_{CTAB} (Figure 49).

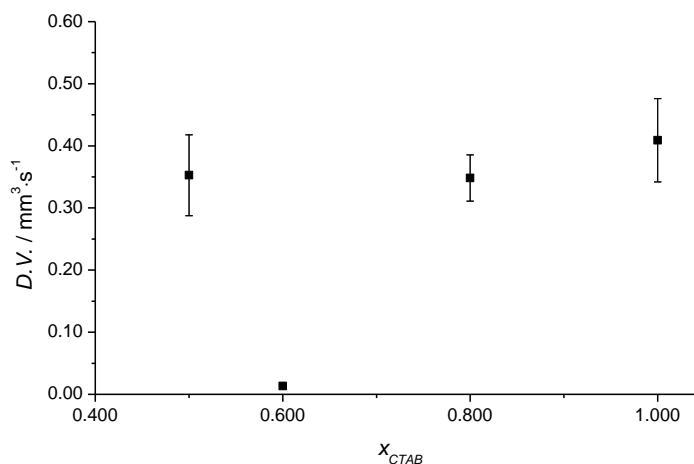


Figure 49 - Drainage velocity of different x_{CTAB} at 20% liquid fraction generated with air containing traces of C_6F_{14}

Drainage velocity is $0.35 \text{ mm}^3 \cdot \text{min}^{-1}$ for sample 0.500, it decreases to a minimum of $0.013 \text{ mm}^3 \cdot \text{min}^{-1}$ for sample 0.600 and then increases until sample 1.000 where the drainage velocity is $0.41 \text{ mm}^3 \cdot \text{min}^{-1}$.

As it was mentioned in section 1.3.5, the bulk viscosity is directly proportional with the characteristic time of foam drainage, which means the drainage velocity is inversely proportional to viscosity. Hence, the product of drainage velocity by viscosity should give rise to a constant value if the other parameters remain constant.

In Figure 50 we present a plot of the product between drainage velocity and viscosity as a function of the x_{CTAB} . The used viscosity value was taken from the viscosity results at a shear rate consistent with the shear provoked by the flow of the solution in a small capillary with typical size of a plateau border ($\approx 20 \mu\text{m}$) at the same velocity as the foam drainage velocity.

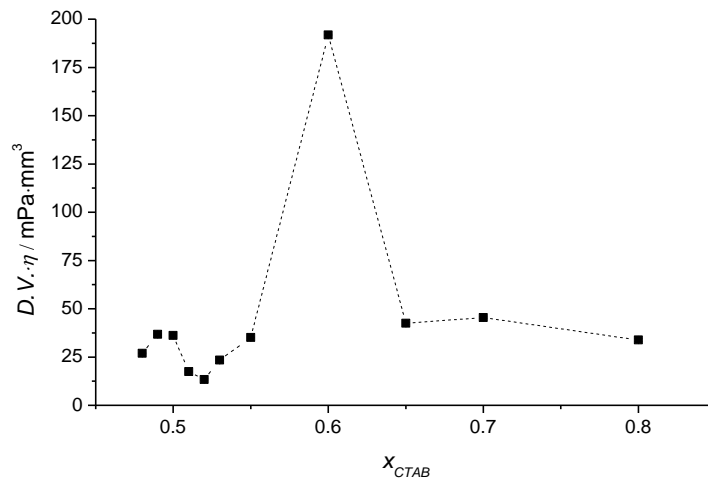


Figure 50 - Product between drainage velocity and viscosity as a function of x_{CTAB} for 20% liquid fraction foams generated with simple air.

The results show an obvious peak for sample 0.600 at 191 $\text{mPa} \cdot \text{m}^3$ more than four times higher than for the other samples. This indicates that considering the viscosity, sample 0.600 is draining faster than expected. For the other samples this product lies between 13 and 45 $\text{mPa} \cdot \text{m}^3$, with slight differences. This product increases from 0.480 to 0.490 that is approximately the same as 0.500. It decreases until 0.530 reaching the minimum and increases again until 0.600 where there is the absolute maximum. Then it decreases to 0.650 and from 0.650 to 0.800 it is almost constant.

The same principle was applied for foams with air containing traces of C_6F_{14} as dispersed phase. The results are presented in Figure 51.

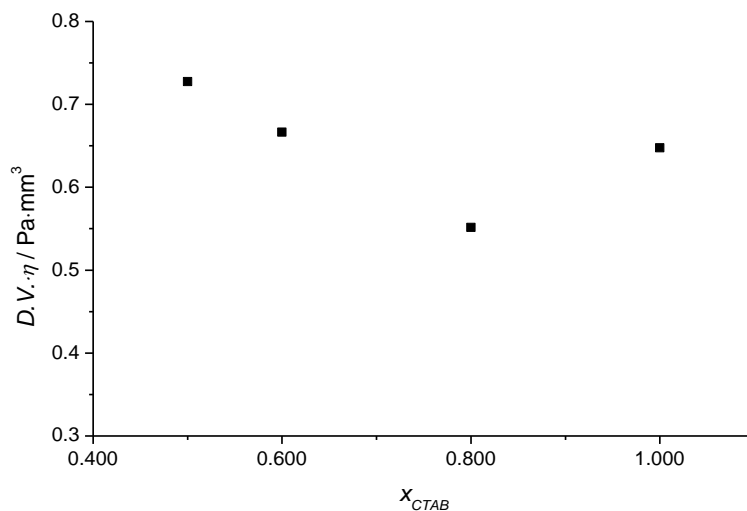


Figure 51 - Product between drainage velocity and viscosity as a function of x_{CTAB} for 20% liquid fraction foams generated with air containing trace amounts of C_6F_{14} .

For this case, the values are higher for sample 0.500 (0.72 mPa·mm³) and decrease until sample 0.800 (0.55 mPa·mm³) to then increase again for 1.000 x_{CTAB} (0.65 mPa·mm³). Nonetheless the values are all of the same order of magnitude.

As an example of the macroscopic behavior of a draining foam, in Figure 52 is represented a foam generated from a solution of $x_{CTAB} = 0.600$, at 20% liquid fraction with simple air as dispersed phase at initial stage and the same sample 20 and 40 minutes after.

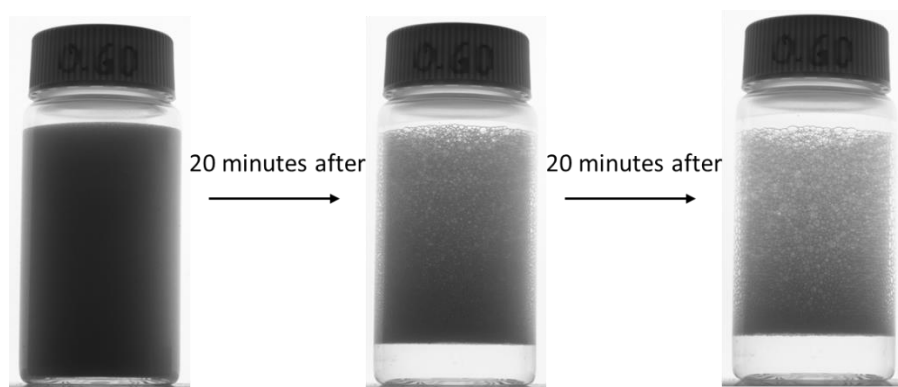


Figure 52 - Photography of foam at 20% liquid fraction (simple air) from sample 0.600 x_{CTAB} in 20 minutes intervals, representing foam ageing.

After the first 20 minutes the foam is obviously more transparent, the size of the bubbles have increased and there is liquid in the bottom of the vial derived from the drainage of the foam. 20 minutes after that, the same evolution is observed.

Another experiment was carried out with the same solution at the same liquid fraction but the dispersed phase is air with traces of C₆F₁₄ (Figure 53).

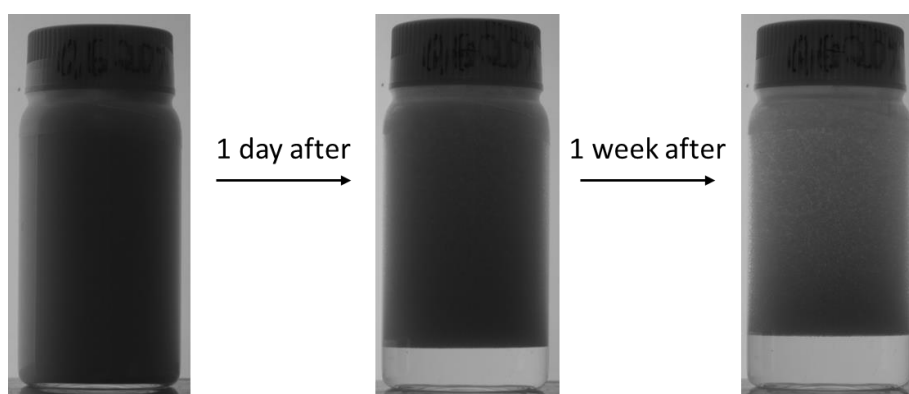


Figure 53 - Photography of foam at 20% liquid fraction (air with trace amounts of C₆F₁₄) from sample 0.600 x_{CTAB} , one hour and 1 week after foam generation, representing foam ageing.

The same evolution processes are observed in the foam such as bubble growth, drainage and increased transparency, but at a much larger time scale. The ageing is

faster for simple air foams. This explains why the drainage velocities are so different between the foams from pure air and those with traces of C_6F_{14} . As the coarsening is almost arrested with the C_6F_{14} the Plateau borders remain small and the drainage is much slower. It is possible that the very fast drainage is only observed in foams made with air as the drainage velocity needs to be sufficiently high to observe it.

To evaluate foam stability one can acquire information about the bubble radius evolution and have an idea about the rate at which coarsening is happening. Foams generated with different x_{CTAB} at 20% liquid fraction with traces of C_6F_{14} in the gas phase were analyzed (Figure 54). The bubble size is the average value of the measurements.

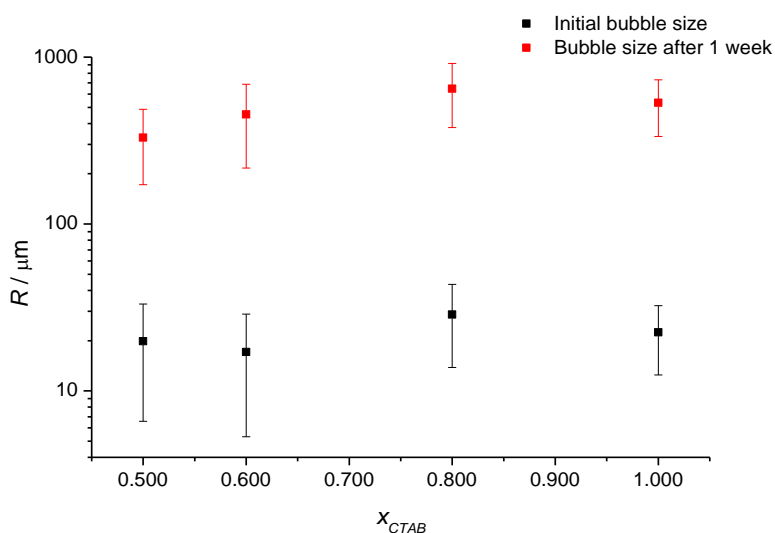


Figure 54 - Bubble radius as a function of the x_{CTAB} at 20 % liquid fraction with air containing trace amounts of C_6F_{14} at the time of formation (black) and one week later (red). The y axis is represented in logarithmic scale for convenience.

Initial bubble size is different for the different foams in study. The average initial bubble size values are comprised between 16 μm and 30 μm decreasing from 20 μm at 0.500 to 17 μm at 0.600. Then it increases again to 29 μm at 0.800 to decrease again to 22 μm for pure CTAB. After one week the bubble radius is lowest for 0.500 with 325 μm it increases until 650 μm for sample 0.800 and decreases again for pure CTAB with 550 μm . The initial bubble size is lowest for sample 0.600 but after 1 week is sample 0.500 with the lowest bubble radius. This indicates that coarsening process is slower for sample 0.500.

3.2.4 SANS in foams

The use of neutron scattering in foams is useful to understand foam structure and probe the aggregation behavior of surfactants inside the foam. In SANS interfaces are very important as a contribution for the scattering. A foam is characterized by its considerable amount of interface which give rise to a strong signal that decays with the q^{-4} . Foams were generated at 0.10, 0.15, 0.20 and 0.25 liquid fractions, for x_{CTAB} of 0.500, 0.600 and 0.800 at $20 \text{ mmol}\cdot\text{kg}^{-1}$. The analyzed samples were prepared in D_2O and C_6F_{14} as dispersed phase.

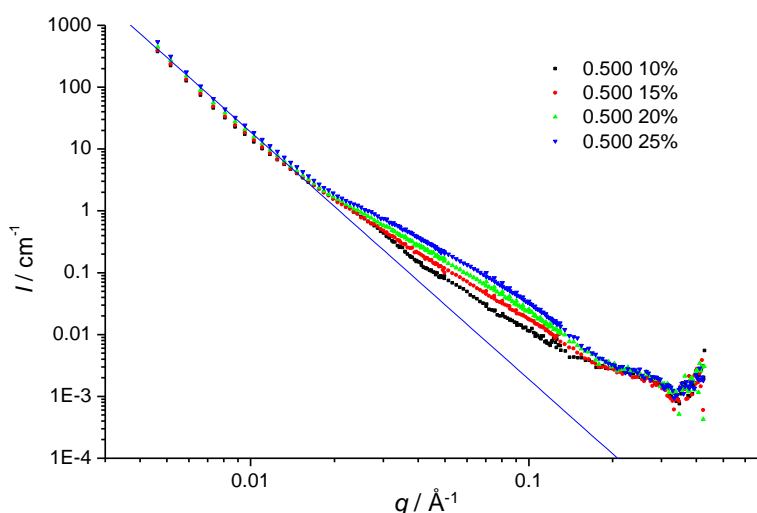


Figure 55 - Scattering intensity as a function of the wave vector for 0.500 x_{CTAB} solutions at $20 \text{ mmol}\cdot\text{kg}^{-1}$ in D_2O , at 10, 15, 20 and 25% liquid fractions with air containing traces of C_6F_{14} as dispersed phase. The blue line represents the q^{-4} decay for low q in sample 0.500 25%.

Figure 55 presents the scattering intensity as a function of q for sample 0.500 at different liquid fractions. The scattering intensity in the low q region present strong signal with a decay that follow a q^{-4} tendency, characteristic of the presence of interfaces. It is observed that at low q , the intensity increases as the liquid fraction increases. Middle q show a systematic increase with the increase in liquid fraction of the foam and high q is roughly the same for all the samples. At 10% ϕ , some oscillations are observed for q around 0.025 that could indicate the presence of a characteristic length.

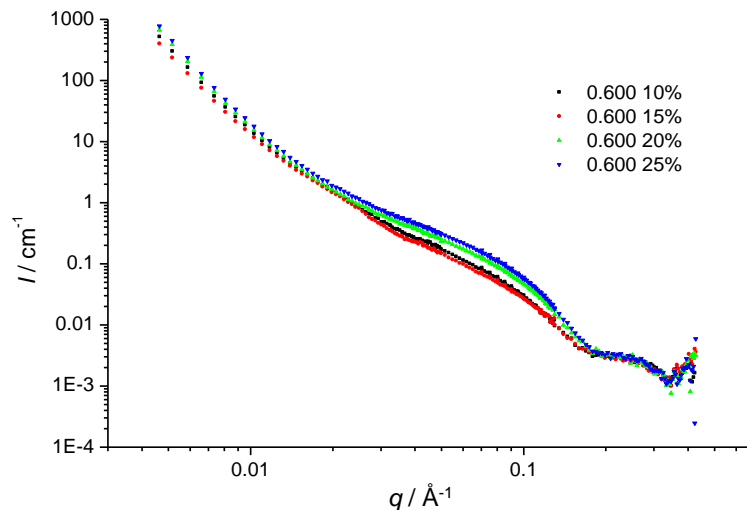


Figure 56 - Scattering intensity as a function of the wave vector for 0.600 x_{CTAB} solutions at $20 \text{ mmol}\cdot\text{kg}^{-1}$ in D_2O , at 10, 15, 20 and 25% liquid fractions with air containing traces of C_6F_{14} as dispersed phase.

Foams with different liquid fractions of 0.600 x_{CTAB} show the typical strong signal with q^4 dependence for foams (Figure 56). At low q the intensity increases with increase liquid fraction from sample 0.600 15% to 0.600 25% and sample 0.600 10% appears to increase in intensity compared with 0.600 15%. Middle q follows the same tendency as low q with small oscillations for q around 0.030. High q values are the same for the different samples.

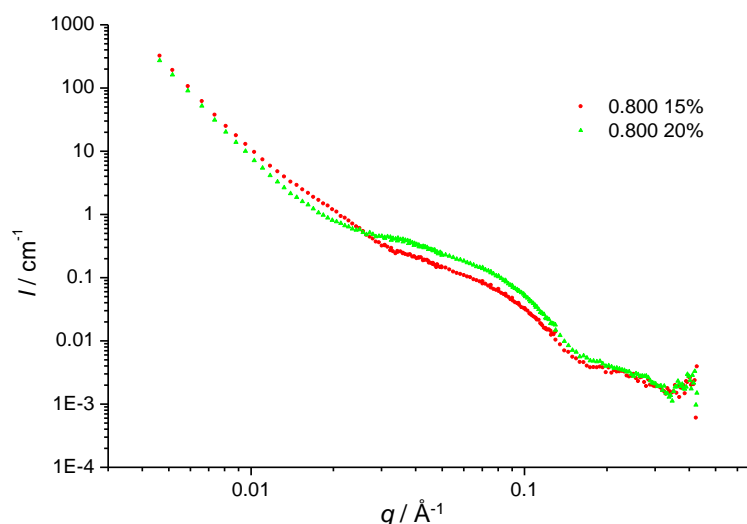


Figure 57 - Scattering intensity as a function of the wave vector for 0.500 x_{CTAB} solutions at $20 \text{ mmol}\cdot\text{kg}^{-1}$ in D_2O , at 15 and 20% liquid fractions with air containing traces of C_6F_{14} as dispersed phase.

The analysis of 0.800 x_{CTAB} foams with 15% and 20% liquid fractions show high intensity at low q with a decay following q^4 . In this sample the intensity at low q is higher for sample 0.800 15%. At q around 0.025 the intensity of the samples is approximately

the same and for middle q , intensity of sample 0.800 20% gets stronger. At high q the scattering intensity is very similar, slightly more intense for 20%.

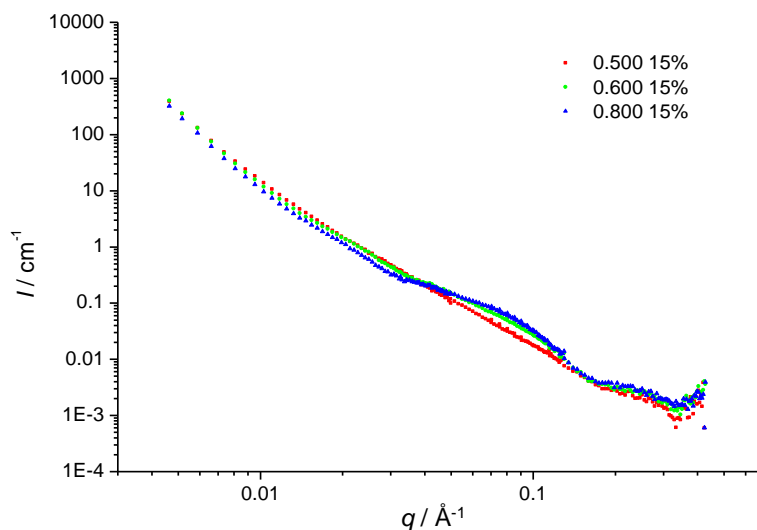


Figure 58 - Scattering intensity as a function of the wave vector for 0.500, 0.600 and 0.800 x_{CTAB} solutions at 20 $\text{mmol}\cdot\text{kg}^{-1}$ in D_2O , at 15% liquid fraction with air containing traces of C_6F_{14} as dispersed phase.

The comparison of the different x_{CTAB} analyzed at the same liquid fraction is presented in Figure 58. The foam scattering intensity for low q is very similar for the different x_{CTAB} , slightly smaller for 0.800. At middle q a notorious difference is observed between samples. At high q sample 0.500 15% has slightly lower intensity than the other samples.

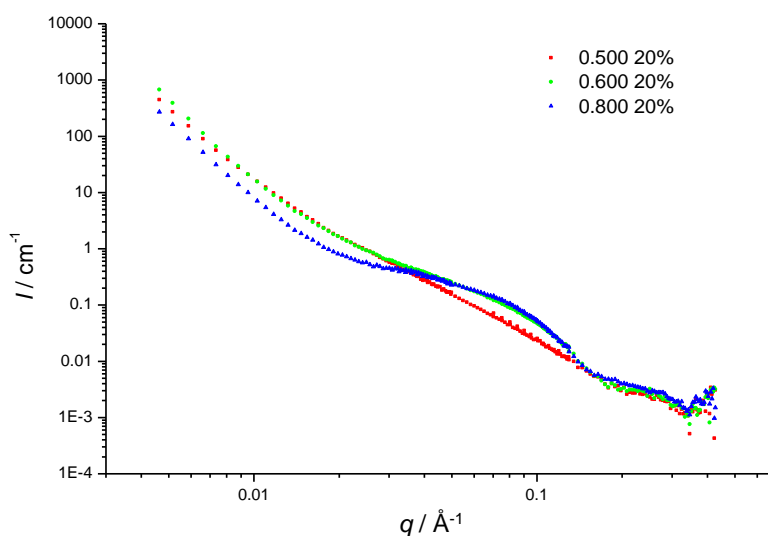


Figure 59 - Scattering intensity as a function of the wave vector for 0.500, 0.600 and 0.800 x_{CTAB} solutions at 20 $\text{mmol}\cdot\text{kg}^{-1}$ in D_2O , at 20% liquid fraction with air containing traces of C_6F_{14} as dispersed phase.

The analysis of Figure 59 permit the observation of a big difference at low q for foam 0.800 20%. At q around 0.03 the relative intensity between the curves changes and

at middle q , sample 0.800 20% and 0.600 20% are higher than 0.500 20% and approximately the same. For high q no difference is found between the different samples.

3.2.5 Discussion – Foam behavior

The results indicate that foam ageing is dependent on x_{CTAB} . The drainage velocity of foams generated with simple air as dispersed phase decreases with x_{CTAB} from $21.3 \text{ mm}^3 \cdot \text{s}^{-1}$ at 1.000 to 0.550 reaching a minimum of $1.88 \text{ mm}^3 \cdot \text{s}^{-1}$ to increase again until $17.3 \text{ mm}^3 \cdot \text{s}^{-1}$ for sample 0.480. The product between the drainage velocity and viscosity of the solution are in line with the expected dependence except for sample 0.600 that is draining faster than expected considering its viscosity.

In foams where air with trace amounts of C_6F_{14} is used, the drainage velocity presents a similar trend as for the foams generated with simple air where the drainage velocity decreases with x_{CTAB} from $0.41 \text{ mm}^3 \cdot \text{min}^{-1}$ for sample 1.000 to $0.013 \text{ mm}^3 \cdot \text{min}^{-1}$ for sample 0.600. Then it increases again until $0.35 \text{ mm}^3 \cdot \text{min}^{-1}$ for sample 0.500. For this foams no considerable deviation was found for the values of the product between drainage velocity and viscosity.

Bubble size of foams for different x_{CTAB} generated with air containing C_6F_{14} is different for the different samples both in the initial stage and after one week. Bubble radius is lowest ($17 \mu\text{m}$) for 0.600 in the initial stage but one week after it is the 0.500 with the lowest bubble radius ($325 \mu\text{m}$) suggesting that the gas exchange is different for the different compositions. The ratio of the final bubble size to the initial bubble size is around 24 for the three samples at 0,600 (26), 0,800 (22) and 1,000 (25). This ratio is much smaller (16) for the sample at 0.500. This indicates that coarsening process is slower for sample 0,500, as the drainage is not slower it suggests that the coarsening is slow because of interfacial properties.

For all the foam scattering plots, there is a strong signal for low q with a decay approximately of q^{-4} . This big contribution in the spectra derives from the interfaces that are present in great quantity in foams. It is expected that in foams with higher liquid fraction, the contribution from the interfaces to be lower since the relative amount of air dispersed in the solution is smaller. In this results we observe for 0.500 with different liquid fractions that both at low q scattering is more intense for samples with higher liquid fraction. Also for 0.600 the intensity of the plots increases with increase liquid fraction

except for sample 0.600 10% where the intensity is higher than for sample 0.600 15%. On sample 0.800 the scattering intensity at low q is higher for sample 0.800 15% than 0.800 20% but at middle q the intensity is stronger for the last one. The different molar ratios in study present different scattering patterns, especially at middle q , consistent with the aggregates present in the bulk samples, indicating that different types of objects are present inside the foams.

The unexpected high scattering intensity for low q in samples mentioned above can be explained by the high amount of scattering objects within the Plateau borders. Since the double syringe method produce samples with characteristic bubble radius, we can assume that amount of scattering objects increase with the amount of solution inside the foam. For sample 0.600 10% this tendency is not observed probably because, due to the high viscosity of the sample that could have led to bad foaming, hence changing the liquid fraction and bubble distribution. Sample 0.800 present the expected behavior where the low q signal is higher for the lowest liquid fraction (interfaces dominate) and the middle q signal is higher for higher liquid fraction where aggregates dominate.

The acquired data indicates that the presence of C_6F_{14} in the dispersed phase has great impact on foam ageing. The drainage velocity for foams with the fluor carbon compound is about a hundred times lower than the foams with simple air. This suggests that slower coalescence is linked with slower drainage velocity. For both foams with different dispersed gases it is clear that the x_{CTAB} has influence in foam stability. It is observed that as the rod-like micelles grow the drainage velocity of the samples decrease but as soon as they disappear drainage velocity tend for the same value both when vesicles or ellipsoid micelles are present in solution. The interaction between rods give rise to high viscosity that slows down the liquid flow through the foam channels. A change in the aggregation tuned by the x_{CTAB} can be used to control the foam ageing process.

Comparison with previous results

Few studies were conducted regarding the foamability and foam stability of foams derived from catanionic mixtures. *Stocco* and coworkers ^[36] performed a study with a catanionic mixture of CTAB and myristic acid ($C_{13}COOH$) evaluating surface properties and foam behavior. In this study, the authors observed that catanionic mixtures present a lowering in surface tension compared to the individual surfactants and that the surface

tension is approximately the same for samples close to equimolarity. They also showed that the surfactants mixture ratio influence foam stability, as observed also in our work. Another study, by *Varade* and coworkers ^[35], with the same system but in a particular ratio of 2 C₁₃COOH : 1 CTAB, considered the generation of a low foamability ultra-stable foam, whose stability is dependent on the very high amount of vesicles in the solutions that constrain the drainage of the samples. Although vesicles are present in our system, there was no evidence of this behavior and the samples presented high foamability.

In a different study, by *Fauser* and coworkers ^[37], a mixture of DTAB and SDS was probed regarding foam film formation and stabilization. In this study, the author also found a dependence of the film stability and formation with the mixture ratio. This system differs significantly from CTAB/SO₂, since the hydrophobic chains are symmetric with twelve carbons each and only the anionic-rich region gives rise to stable foam films. In contrast, in our system, foams are only observed in the cationic-rich region. Nonetheless all these studies point out that the electrostatic interaction between the oppositely charged surfactants is responsible for an increase in foam stability compared with the single surfactants.

4 Conclusions and perspectives

The phase behavior of the catanionic mixture cetyl trimethylammonium bromide (CTAB) / sodium octyl sulfonate (SOSo), as a function of x_{CTAB} has been determined with focus on how different compositions affect the bulk self-assembly and the ageing process of foams generated from the different solutions.

Interfacial studies of the different mixtures were carried out by tensiometry where it was found that both *cmc* and surface tension of the mixtures at *cmc* are lower than for the individual surfactants. Along with an average β parameter of -16 for the mixture, these results indicate a strong synergism between the two oppositely charged surfactants (negative deviation from the ideal behavior).

In the course of this work it was found that x_{CTAB} has significant influence on the different parameters studied mainly in bulk self-assembly, solution viscosity and foam stability.

Resorting to light microscopy, DLS, cryo-TEM and SANS, it was found that bulk aggregation behavior comprises the presence of: ellipsoidal micelles, from $x_{CTAB} = 0.900$ to 0.800; rod-like micelles, that increase in size as the x_{CTAB} decreases from 0.750 to 0.590; and vesicles, with high degree of radius polydispersity, of different bilayer thickness, which can be positively charged in the equimolar region, or negatively charged from 0.200 to 0.100. The types of aggregates formed can be rationalized based on the *CPP* model and molecular interaction between surfactants.

In the cationic-rich side, the variation of the solution viscosity is related with the presence of rod-like micelles with different lengths. Longer rods give rise to solutions with higher viscosity. For samples where spherical micelles or vesicles are present no significant difference between the viscosities is observed.

Rod-like micelles also play an important role in the drainage velocity of foams, and it is observed that the longer these structures are, the lower the drainage velocity is. Bubble size variation showed that there is an influence in coarsening depending on x_{CTAB} . The gas exchange between bubbles is approximately the same for x_{CTAB} between 1.000 and 0.600, but is lower for 0.500. For the anionic-rich side, it is not possible to generate foam. The presence of C_6F_{14} has great influence on coarsening and foam drainage velocity, increasing substantially foam stability. SANS studies inside the foam structure have shown the presence of the same types of aggregates than the ones found in the bulk.

Overall, we have demonstrated that in catanionic mixtures a considerable amount of properties can be tuned by the simple variation of x_{CTAB} . There are, however, several

topics that could be further explored, such as the influence of concentration and temperature in the bulk behavior, and the foam stability with different liquid fractions. Moreover, new studies could be done with this type of mixtures, such as systems with different mismatch between the surfactant tails, which could bring better understanding on the relation between aggregation and foaming properties.

5 Bibliography:

1. Krister Holmberg, B. J., Bengt Kronberg and Bjorn Lindman. *Surfactants and polymers in aqueous solutions*; John Wiley & Sons Ltd., Chichester, 2002.
2. Singh, S. *Liquid Crystals*; World Scientific Publishing Company: Singapore, 2002.
3. Marques, E. F.; Brito, R. O.; Wang, Y.; Silva, B. F. B. Thermotropic phase behavior of triple-chained cationic surfactants with varying headgroup chemistry. *J Colloid Interface Sci.* **2006**, *294* (1), 240-247.
4. Silva, B. F. B.; Marques, E. F.; Olsson, U. Unusual Vesicle–Micelle Transitions in a Salt-Free Cationic Surfactant: Temperature and Concentration Effects. *Langmuir* **2008**, *24* (19), 10746-10754.
5. Menger, F. M.; Keiper, J. S.; Mbadugha, B. N. A.; Caran, K. L.; Romsted, L. S. Interfacial Composition of Gemini Surfactant Micelles Determined by Chemical Trapping. *Langmuir* **2000**, *16* (23), 9095-9098.
6. Goretí Silva, S.; Fernandes, R. F.; Marques, E. F.; do Vale, M. L. C. Serine-Based Bis-quat Gemini Surfactants: Synthesis and Micellization Properties. *Eur. J. Org. Chem.* **2012**, *2012* (2), 345-352.
7. H. Butt, K. G., Michael Kappl. *Physics and Chemistry of Interfaces 2ed.*; Wiley-VCH Verlag GmbH & Co: Weinheim, 2006.
8. Schramm, L. L. *Surfactants: Fundamentals and applications in the petroleum industry*, Cambridge university press: Cambridge, 2000.
9. Presto, W. C.; Preston, W. Some Correlating Principles of Detergent Action. *J. Phys. Colloid Chem.* **1948**, *52* (1), 84-97.
10. Marques, E. F.; Regev, O.; Khan, A.; Lindman, B. Self-organization of double-chained and pseudodouble-chained surfactants: counterion and geometry effects. *Adv. Colloid Interface Sci.* **2003**, *100–102*, 83-104.
11. Wilkinson, C. b. A. D. M. a. A. IUPAC. Compendium of Chemical Terminology, 2nd ed. (the "Gold Book"). <http://goldbook.iupac.org/K03415.html>.
12. Santos, C. I. C. Propriedades interfaciais e de auto-agregação de tensoactivos derivados da treonina e suas misturas catiónicas. Master, Faculdade de Ciências da Universidade do Porto, **2013**.
13. Chabba, S.; Kumar, S.; Aswal, V. K.; Kang, T. S.; Mahajan, R. K. Interfacial and aggregation behavior of aqueous mixtures of imidazolium based surface active ionic liquids and anionic surfactant sodium dodecylbenzenesulfonate. *Colloids Surf. A: Physicochemical and Engineering Aspects* **2015**, *472*, 9-20.

14. Emilio, A.; Elena, J. Surfactant Aggregates: Experimental and Theoretical Characterization of Mixed Systems. In *Encyclopedia of Surface and Colloid Science, Third Edition*; CRC Press, 2015, pp 7116-7132.
15. Marques, E. F.; Regev, O.; Khan, A.; da Graça Miguel, M.; Lindman, B. Vesicle Formation and General Phase Behavior in the Catanionic Mixture SDS–DDAB–Water. The Anionic-Rich Side. *J. Phys. Chem. B* **1998**, *102* (35), 6746-6758.
16. Tah, B.; Pal, P.; Mahato, M.; Talapatra, G. B. Aggregation Behavior of SDS/CTAB Catanionic Surfactant Mixture in Aqueous Solution and at the Air/Water Interface. *J. Phys. Chem. B* **2011**, *115* (26), 8493-8499.
17. Marques, E.; Khan, A.; da Graça Miguel, M.; Lindman, B. Self-assembly in mixtures of a cationic and an anionic surfactant: the sodium dodecyl sulfate-didodecyltrimethylammonium bromide-water system. *J. Phys. Chem.* **1993**, *97* (18), 4729-4736.
18. Herrington, K. L.; Kaler, E. W.; Miller, D. D.; Zasadzinski, J. A.; Chiruvolu, S. Phase behavior of aqueous mixtures of dodecyltrimethylammonium bromide (DTAB) and sodium dodecyl sulfate (SDS). *J. Phys. Chem.* **1993**, *97* (51), 13792-13802.
19. Kaler, E. W.; Herrington, K. L.; Murthy, A. K.; Zasadzinski, J. A. N. Phase-behavior and structures of mixtures of anionic and cationic surfactants. *J. Phys. Chem.* **1992**, *96* (16), 6698-6707.
20. Silva, S. G.; do Vale, M. L. C.; Marques, E. F. Size, Charge, and Stability of Fully Serine-Based Catanionic Vesicles: Towards Versatile Biocompatible Nanocarriers. *Chem. Eur. J.* **2015**, *21* (10), 4092-4101.
21. Bramer, T.; Dew, N.; Edsman, K. Pharmaceutical applications for catanionic mixtures. *J. Pharm. Pharmacol.* **2007**, *59* (10), 1319-1334.
22. <http://www.miningeducation.com/2012/01/flotation-in-mining.html>;
<http://www.dailymail.co.uk/sciencetech/article-2877550/How-magnets-improve-BEER-Magnetic-field-reduces-foam-make-brews-cheaper-bitter-too.html>;
<http://www.vanguard-ifp.com/firefighting-foam.html>;
https://en.wikipedia.org/wiki/Sea_foam. (accessed 15-09).
23. I. Cantat; S. Cohen-Addad; F. Elias; F. Graner; R. Höhler; O. Pitois; F. Rouyer; Saint-Jalmes, A. *Foams Structure and Dynamics*; Oxford University Press: Oxford, 2013.
24. Malysa, K. Wet foams: Formation, properties and mechanism of stability. *Adv. Colloid Interface Sci.* **1992**, *40*, 37-83.
25. Drenckhan, W., Hutzler, S. Structure and energy of liquid foams. *Adv. Colloid Interface Sci.* **2015**, *224*, 1-16.
26. Weaire D, H. S. *The physics of foams*; Clarendon Press: Oxford, 1999.

27. Besson, S.; Debrégeas, G. Statics and dynamics of adhesion between two soap bubbles. *Eur. Phys. J. E* **2007**, *24* (2), 109-117.
28. Brakke, K. Instability of the wet cube cone soap film. *Colloids Surf. A: Physicochemical and Engineering Aspects* **2005**, *263* (1–3), 4-10.
29. Weaire, D.; Hutzler, S.; Verbist, G.; Peters, E. A Review of Foam Drainage. In *Advances in Chemical Physics*; John Wiley & Sons, Inc., 2007, pp 315-374.
30. Rio, E.; Drenckhan, W.; Salonen, A.; Langevin, D. Unusually stable liquid foams. *Adv. Colloid Interface Sci.* **2014**, *205*, 74-86.
31. Fameau, A.-L.; Saint-Jalmes, A.; Cousin, F.; Houinsou Houssou, B.; Novales, B.; Navailles, L.; Nallet, F.; Gaillard, C.; Boué, F.; Douliez, J.-P. Smart Foams: Switching Reversibly between Ultrastable and Unstable Foams. *Angew. Chem. Int. Ed.* **2011**, *50* (36), 8264-8269.
32. Novales, B.; Navailles, L.; Axelos, M.; Nallet, F.; Douliez, J.-P. Self-Assembly of Fatty Acids and Hydroxyl Derivative Salts. *Langmuir* **2008**, *24* (1), 62-68.
33. Anniina Salonen, C. G., Armando Maestro, Wiebke Drenckhan, Emmanuelle Rio. Arresting bubble coarsening: A model for stopping grain growth with surface elasticity. <hal-01149400v2> **2016**.
34. Fameau, A.-L.; Salonen, A. Effect of particles and aggregated structures on the foam stability and aging. *C. R. Phys.* **2014**, *15* (8–9), 748-760.
35. Varade, D.; Carriere, D.; Arriaga, L. R.; Fameau, A. L.; Rio, E.; Langevin, D.; Drenckhan, W. On the origin of the stability of foams made from catanionic surfactant mixtures. *Soft Matter* **2011**, *7* (14), 6557-6570.
36. Stocco, A.; Carriere, D.; Cottat, M.; Langevin, D. Interfacial Behavior of Catanionic Surfactants. *Langmuir* **2010**, *26* (13), 10663-10669.
37. Fauser, H.; Uhlig, M.; Miller, R.; von Klitzing, R. Surface Adsorption of Oppositely Charged SDS:C(12)TAB Mixtures and the Relation to Foam Film Formation and Stability. *J. Phys. Chem. B* **2015**, *119* (40), 12877-12886.
38. Wollmann, J.-C. G. R. The History of Sclerosing Foams. *Dermatol. Surg.* **2004**, *30* (5), 694-703.
39. Holmberg, K.; Shah, D.; Schwuger, M. *Handbook of applied surface and colloid chemistry*; John Wiley & Sons, Inc.: Wiltshire, 2002; Vol. 2.
40. Hiemenz, P.; Rajagopalan, R. *Principles of Colloid and Surface Chemistry*; 3rd ed.; Marcel Dekker, Inc.: New York, 1997.
41. Leng, Y. *Materials Characterization - Introduction to Microscopic and Spectroscopic Methods*; JohnWiley & Sons (Asia) Pte Ltd: Singapore, 2008.
42. Abramowitz, M. *Microscope basics and beyond*; Olympus America Inc. : New York, 2003.

43. Murphy, D.; Davidson, M. *Fundamentals of Light Microscopy and Electronic Imaging*; 2nd ed.; John Wiley & Sons, Inc.: New Jersey, 2013.
44. Holoubek; Jaroslav. Some applications of light scattering in materials science. *J. Quant. Spectrosc. Rad. Transfer* **2007**, *106* (1–3), 104-121.
45. Huglins, M. B. *Light scattering from polymer solution*; Plenum Press: New York, 1972.
46. Murphy, R. M. Static and dynamic light scattering of biological macromolecules: what can we learn? *Curr. Opin. Biot.* **1997**, *8* (1), 25-30.
47. Kirby, B. J. *Micro- and Nanoscale Fluid Mechanics - transport in microfluidic devices*; Cambridge University Press: Cambridge, 2010.
48. Paillot, R. M. SMOLUCHOWSKI. — Contribution à la théorie de l'endosmose électrique et de quelques phénomènes corrélatifs (Bulletin de l'Académie des Sciences de Cracovie; mars 1903). *J. Phys. Theor. Appl.* **1904**, *3* (1), 912.
49. Martin, A. Y.; Isayev, A. I. *Rheology: Concepts, Methods, & Applications*; ChemTec Publishing: Toronto, 2006.
50. Walters, K.; Jones, W. M. *Instrumentation Reference Book*; 4th ed.; Elsevier: Oxford, 2010.
51. Viswanath, D.; Ghosh, T.; Prasad, D.; Dutt, N.; Rani, K. *Viscosity of Liquids*. Springer: Dordrecht, 2007.
52. Rheosys. Basic Introduction to Viscometers & Viscometry. (accessed 16/09).
53. Dubochet, J.; Adrian, M.; Chang, J.-J.; Homo, J.-C.; Lepault, J.; McDowell, A. W.; Schultz, P. Cryo-electron microscopy of vitrified specimens. *Q. Rev. Biophys.* **2009**, *21* (2), 129-228.
54. Almgren, M. Alexander Lecture 2003: Cubosomes, Vesicles, and Perforated Bilayers in Aqueous Systems of Lipids, Polymers, and Surfactants. *Aust. J. Chem.* **2003**, *56* (10), 959-970.
55. *Neutron, X-rays and Light. Scattering Methods Applied to Soft Condensed Matter*; 1st ed.; Elsevier: North Holland, 2002.
56. Richardson; Robert. Scattering and Reflection Techniques. In *Colloid Science*; Blackwell Publishing Ltd., 2009, pp 228-254.
57. Kern, F.; Zana, R.; Candau, S. J. RHEOLOGICAL PROPERTIES OF SEMIDILUTE AND CONCENTRATED AQUEOUS-SOLUTIONS OF CETYLTRIMETHYLAMMONIUM CHLORIDE IN THE PRESENCE OF SODIUM-SALICYLATE AND SODIUM-CHLORIDE. *Langmuir* **1991**, *7* (7), 1344-1351.
58. Talmon, Y. Transmission electron microscopy of complex fluids: The state of the art. *Ber. Bunsen-Ges. Phys. Chem. Chem. Phys.* **1996**, *100* (3), 364-372.

59. Fernandes, R. M. F.; Marques, E. F.; Silva, B. F. B.; Wang, Y. Micellization behavior of a cationic surfactant with high solubility mismatch: Composition, temperature, and salt effects. *J. Mol. Liq.* **2010**, *157* (2–3), 113-118.
60. Brasher, L. L.; Herrington, K. L.; Kaler, E. W. Electrostatic effects on the phase-behavior of aqueous cetyltrimethylammonium bromide and sodium octyl sulfate mixtures with added sodium-bromide. *Langmuir* **1995**, *11* (11), 4267-4277.
61. Karukstis, K. K.; McCormack, S. A.; McQueen, T. M.; Goto, K. F. Fluorescence delineation of the surfactant microstructures in the CTAB-SOS-H₂O cationic system. *Langmuir* **2004**, *20* (1), 64-72.
62. Nan, Y.; Liu, H.; Hu, Y. Aqueous two-phase systems of cetyltrimethylammonium bromide and sodium dodecyl sulfonate mixtures without and with potassium chloride added. *Colloids Surf., A: Physicochemical and Engineering Aspects* **2005**, *269* (1–3), 101-111.
63. You, Y. L.; Hao, L. S.; Nan, Y. Q. Phase behavior and viscous properties of cetyltrimethylammonium bromide and sodium dodecyl sulfonate aqueous mixtures. *Colloids Surf., A: Physicochemical and Engineering Aspects* **2009**, *335* (1-3), 154-167.
64. Zhang, S.; Teng, H. N. Rheology and microstructure studies of SDS/CTAB/H₂O system. *Colloid J.* **2008**, *70* (1), 105-111.
65. Chen, D. H.; Hall, D. G. Phase diagrams of the systems (I) Sodium dodecyl sulphate — octyl trimethyl ammonium bromide-water, (II) Sodium dodecyl sulphate — dodecyl trimethyl ammonium bromide-water. *Kolloid-Zeitschrift und Zeitschrift für Polymere* **1973**, *251* (1), 41-44.